PEOPLE'S DEMOCRATIC REPUBLIC OF ALGERIA
MINISTRY OF HIGHER EDUCATION AND SCIENTIFIC RESEARCH

University of Mohamed Boudiaf - M'sila
Faculty of Technology
Department of Electronics

THESIS

A dissertation submitted for the degree of
DOCTORAT

Field**:** Electronics

Option**:** Electronics and Telecommunications

By: MELOUKI Noureddine

THEME

Contribution to the analysis and design of a microstrip antenna based on EBG structures for modern wireless communication systems

« Contribution à l'analyse et à la conception d'une antenne microstrip à base de structures EBG pour les systèmes de communication sans fil modernes. »

Presented and publicly defended on the 29/07/2021

JURY MEMBERS:

MEZACHE Amar	**Professor**	**Univ. of M'sila**	**Chairman**
HOCINI Abdesselam	**Professor**	**Univ. of M'sila**	**Supervisor**
DENIDNI Tayeb Ahmed	**Professor**	**Univ. of Quebec**	**Co-supervisor**
KHEDROUCHE Djamel	**Professor**	**Univ. of M'sila**	**Examiner**
LADJAL Mohamed	**MCA**	**Univ. of M'sila**	**Examiner**
ZEBIRI Chemseddine	**MCA**	**Univ. of Setif**	**Examiner**

2020/2021

Acknowledgments

First and foremost, all gratitude is due to "ALLAH" for giving me the strength, courage, and commitment that enabled me to start and finish this research work.

I am extremely grateful to my supervisors, Prof. Abdesselam HOCINI and Prof. Tayeb Ahmed DENIDNI for their invaluable advice, continuous support, and patience during my PhD study. Their immense knowledge and plentiful experience have encouraged me in all the time of my academic research and daily life.

I would also like to thank and express my sincere gratitude and appreciation to Prof. Djamel KHEDROUCHE for all his support, time, motivation, and advice throughout the accomplishment of this modest research work, and for having agreed to examine my work by taking part in the thesis jury. Also would like to thank all the members of the Signal and Systems Analysis Laboratory (LASS) under the direction of Prof. Abdesselam HOCINI, where my research began during these past four years, and extend my gratitude also to all the members of the Radio Frequency Laboratory (LRF) in INRS-EMT, Montréal Canada, under the guidance of Prof. Tayeb Ahmed DENIDNI. It is their kind help and support that have made my study and life in Canada a wonderful time.

I would like to express my sincere appreciation to Prof. Amar MEZACHE, professor at the University of M'sila, for his interest in my work by doing the honor of chairing the jury of my defense.

I would like to extend my sincere thanks to all members of the jury:

I would like to thank Dr. Chemseddine ZEBIRI, MCA at the University of Setif, for his interest in this work and for having agreed to examine my work by taking part in the thesis jury.

I would like to thank Dr. Mohamed LADJAL, MCA at the University of M'sila, for his interest in this work and for having agreed to examine my work by taking part in the thesis jury.

My appreciation also goes out to my family and friends for their encouragement and support all through my studies.

Above all I would like to thank my wife Houda for her love and constant support, for all the late nights and early mornings, and for keeping me sane over the past five years. Thank you for being my muse, editor, proofreader, and sounding board. But most of all, thank you for being my best friend. I owe you everything, and without my wife, Houda, none of this would ever have been possible, she was always there, and always supported me unconditionally. To have a woman of such infinite talent and dynamism invest all her precious time and life to support the dreams of the man she's married to, is a powerful thing, and I have striven every day to live up to that. Our old five-year plan is complete, and the next adventure has begun. I am blessed to be able to share it with such a magnificent woman.

Contribution to the Analysis and Design of a Microstrip antenna based on EBG structures for modern wireless communication systems

by

Noureddine MELOUKI

Saturday 31st July, 2021 14:51

Submitted to the Department of Electronic, Faculty of Technology, University of Mohamed Boudiaf - M'sila
on July 2021, in partial fulfillment of the requirements for the
Doctoral Program in Electronics and Telecommunications

Abstract

This thesis focuses on the analysis and design of microstrip antennas working in a wide range of frequency bands (WiMAX, UWB, Ku-band, mm-Wave), and based on electromagnetic band gap (EBG) structures. A mushroom-like EBG structure-based substrate is designed, analyzed and optimized using a technique based on the combination of an evolutionary heuristic optimization algorithm (genetic algorithm) with the Computer Simulation Technology (CST) Microwave Studio, for WiMAX applications. Next, a topology optimized ultra wideband antenna alongside a compact FSS layer, covering the UWB spectrum of frequencies, are designed and analyzed. The simulation results and measurements obtained are compared with various works in the open literature. Finally, Fabry-Pérot resonator antennas based on the proposed PRS structures, generated and optimized using an automatic synthesis system, based on a VBA link between MATLAB and CST Microwave studio, were designed, analyzed and fabricated. The obtained results are compared with other research in the open literature, where it is clearly indicated that the proposed designs could be potential candidates for high gain and wideband systems in Ku-band and mm-wave applications, such as the 5G.

Keywords: 5G, Microstrip antenna, EBG/PBG, AMC, FSS, PRS, Genetic algorithm, CST, FPRA.

Publications

Journal Papers

1. **N. Melouki**, A. Hocini, and T. A. Denidni, “Performance enhancement of a compact patch antenna using an optimized EBG structure,”Chinese Journal of Physics, vol. 69, pp. 219-229, 2021.

2. A. Hocini, **N. Melouki**, and T. A. Denidni, "Modeling and simulation of an antenna with optimized AMC reflecting layer for gain and front-to-back ratio enhancement for 5G applications," Journal of Physics: Conference Series, vol. 1492, no. 1, p. 012006. IOP Publishing, 2020.

3. **N. Melouki**, A. Hocini, and T. A. Denidni, “High gain and Wideband Fabry-Perot Resonator Antenna based on a compact single PRS layer,” IEEE Access, (accepted with revision), 2021.

4. **N. Melouki**, A. Hocini, and T. A. Denidni, “Performance Enhancement of An UWB Antenna Using A Compact Topology Optimized Single FSS-Layer as A Reflector,” International Journal of RF and Microwave Computer-Aided Engineering, (accepted with revision), 2021.

International Communications

1. **N. Melouki**, A. Hocini, and T. A. Denidni, “Enhancing the Performances of a Compact Microstrip Antenna Using Electromagnetic Band Gap Structure for Future 5G of Communication Systems,” in The Third International Conference on Technological Advances in Electrical Engineering (ICTAEE’18), December 2018.

2. A. Hocini, **N. Melouki**, and T. A. Denidni, “Modelling and simulation of an optimized AMC reflecting layer for gain and Front-To-Back ratio enhancement for 5G.” in 21st International Summer School on Vacuum, Electron and Ion Technologies (VEIT 2019), September 2019.

Other works(Journal Papers)

1. H. Ben salah, A. Hocini, D. Khedrouche, and **N. Melouki**, "A high-sensitive sensor and band-stop filter based on intersected double ring resonators in metal–insulator–metal structure," Optical and Quantum Electronics, vol. 52, no. 7, p. 86–97, 2020.

2. H. Ben salah, A. Hocini, **N. Melouki**, and D. Khedrouche, "Design and analysis of near infrared high sensitive metal-insulator-metal plasmonic bio-sensor," IOP Conference Series: Materials Science and Engineering, vol. 1046, no. 1, p. 012003. IOP Publishing, 2021.

3. H. Ben salah, A. Hocini, B. Hocine, and **N. Melouki**, "High Sensitivity Plasmonic Sensor Based on Metal–Insulator–Metal Waveguide Coupled with a Notched Hexagonal Ring Resonator and a Stub," ECS Journal of Solid State Science and Technology, IOP Publishing, July 2021.

Contents

List of Figures

List of Tables

List of Abbreviations

5G fifth Generation Mobile Network.

AMC Artificial Magnetic Conductor.

AUT Antenna Under Test.

BPSO Binary Particle Swarm Optimization.

BS Base Station.

CST Computer Simulation Technology.

D2D Device-to-Device.

DNG Double-Negative.

DPS Double-Positive.

EBG Electromagnetic Band Gap.

ENG Epsilon Negative.

ENZ epsilon-near-zero.

FBW Fractional Bandwidth.

FCC Federal Communications Commission.

FDTD Finite Difference Time Domain.

FEM Finite Element Method.

FPRA Fabry-Perot Resonator Antenna.

FSS Frequency Selective Surface.

GA Genetic Algorithm.

HFSS High-Frequency Structure Simulator.

HIS High Impedance Surface.

LHM Left-Handed Medium.

MATLAB MATrix LABoratory.

MIMO Multiple-Input and Multiple-Output.

MNG Mu Negative.

MNZ Mu-near-zero.

MoM Method of Moments.

MPA Microstrip Patch Antenna.

MTL Multi Transmission Line.

MTMs Metamaterials.

NRI Negative Refraction Index.

P2P Point-to-Point.

PBG Photonic Band Gap.

PEC Perfect Electric Conductor.

PG Partial Ground.

PMC Perfect Magnetic Condition.

PRS Partially Reflective Surface.

RCA Resonant Cavity Antenna.

RFID [Radio-frequency identification.

RHM Right-Handed Medium.

RMSE Root-Mean-Square Error.

S-EBG Step-Like Electromagnetic Band Gap.

SAR Specific Absorption Rate.

SLL Side-Lobe Level.

SMA SubMiniature version A.

SNG Single Negative.

SRR Split-Ring Resonator.

TE Transverse Electric.

TM Transverse Magnetic.

UC-PBG Uniplanar Compact Photonic Band Gap.

UWB Ultra-Wideband.

VBA Visual Basic for Applications.

VNA Vector Network Analyzer.

VSWR Voltage Standing Wave Ratio.

WiMAX Worldwide Interoperability for Microwave Access.

WLAN Wireless Local Area Network.

Chapter 1

Introduction

1.1 Motivations

Microstrip patch antennas are becoming the most popular antenna for a variety of applications due to their low weight, low production cost, and ability to operate across a wide frequency range. On the other hand, microstrip antennas, have a significant disadvantage in terms of bandwidth, efficiency, and size.

The key objective in microstrip patch antenna designs is to broaden the narrow bandwidth, which is inherent in microstrip antennas, and to miniaturise the patch antenna size. Increasing the thickness of the substrate will improve the narrow bandwidth; however, this will result in a larger surface waves, which will reduce the antenna's radiation efficiency and degrade the antenna pattern.

To overcome these disadvantages, microstrip patch antennas are incorporated with various materials used to improve the antenna's potential parameters, with electromagnetic band gap (EBG) structures proving to be the most suitable.

Electromagnetic Band gap (EBG) structures have piqued the interest of numerous researchers in electromagnetism, particularly in the field of telecommunications, for more than two decades. Their miniaturised integrations and specific electromagnetic properties are of great interest in terms of electromagnetic surface wave suppression. Because of their distinct bandgap characteristics, EBG structures can be classified as a special type of metamaterials.

This thesis aims mainly to develop EBG-based microstrip antennas that fulfil the

requirements of significant radiation gain and efficiency, while maintaining a miniaturisation compatible with component integration technology in the architecture of future wireless communication systems.

1.2 Thesis Contributions and Organization

The contributions and outlines of this thesis are ordered as follows:

In Chapter 2, an overview of metamaterials structures, namely the Electromagnetic and Photonic Band Gap structures (EBG PBG), Artificial Magnetic Conductors (AMC), and Frequency Selective surfaces (FSS), is briefly presented.

PBG based patch antenna is analyzed and discussed, followed by an AMC backed coaxial-fed antenna for gain and front-to-back ratio improvements, both working in the Mm-wave region.

Chapter 3 will present a designed EBG based microstrip patch antenna using CST Microwave Studio linked to the genetic algorithm embedded in MATLAB as an optimization technique to create a unique EBG structure that enhance the electrical characteristics of the antenna. First, the microstrip antenna is designed based on a step-like substrate using two layers, to enhance both the impedance bandwidth and peak gain, with an adequate performances, then employing it as a base substrate for the proposed design approach. After that, an optimization of the mushroom-like EBG is presented and analyzed using CST Microwave studio and optimized according to a fitness function for bandwidth, gain and side lobe levels enhancement.

The potential of this published work [1] is presented by comparing it to the literature.

Chapter 4 will present a designed and analyzed compact Ultra-Wideband (UWB) monopole antenna, synthesized using a computer aided system based on a VBA based link between CST and MATLAB, creating unique pixelated patterns, according to a merit function to enhance the electrical properties of the patch antenna namely it's impedance bandwidth, while keeping it's footprint as small as possible for a more efficient UWB antenna, followed by the design of an Ultra-Wideband FSS based layer employed as a reflector for the previously designed UWB antenna.

Different FSS unit cells designed were simulated and analyzed. A parametric study is in order to improve the electrical characteristics of the UWB antenna. The final optimized designs for both the UWB source antenna and the FSS based reflecting layer are fabricated and validated with measurements.

Finally, the proposed design is compared with other research papers, proving the feasibility of the final design as a potential candidate for UWB applications.

Chapter 5 will present the analysis and design of an aperture-coupled wideband antenna as a source, to form a Fabry-Perot Resonator, using a PRS based superstrate synthesized and generated throughout a unique pixelating system, creating different patterns, to achieve certain goals according to a fitness function in the genetic algorithm module of MATLAB, in corporation with the commercial simulator CST.

In this chapter, first, a wide band aperture-coupled antenna is proposed, as a source feeding antenna, which consists of a parasitic patch, coupled to a feeding line through a slotted ground plane, is analyzed and investigated for its interesting characteristic, namely the wide band of operation, in both the Ku- and Mm-wave bands, followed by the PRS unit cell designs for both frequency spectrums, providing a positive phase gradient properties, which leads to a wider impedance and 3-d gain bandwidths. Then by applying the designed PRSs as superstrates to the aperture-coupled wideband antennas, in both communication scenarios (Ku-band and Mm-wave) in which its enhancements are achieved and compared to other related works in the open literature, proving how performing these proposed designs can be as potential candidates for present and future wireless communication systems.

Chapter 6 will conclude the presented contributions and will provide some suggestions for future works.

Chapter 2

Metamaterials: Electromagnetic Band Gap structures (EBG) in Antenna Engineering

2.1 Introduction

Metamaterials (MTMs) were proposed first by Veselago [2], based on the idea that the constitutive values ϵ (electric permittivity) and μ (magnetic permeability) of an effectively homogeneous material could both be negative. As a result, several physical phenomena, such as the reversal of Snell's law, the reversal of Doppler shift, and the reversal of the Cerenkov effect, could change their natural behaviour. The refractive index n is related to the constitutive material parameters and as follows:

$$n = \pm\sqrt{\varepsilon_r \mu_r} \tag{2.1}$$

where ϵ_r and μ_r are the relative permittivity and permeability related to the free space permittivity $\epsilon_0 = \epsilon \ / \ \epsilon_r \approx 8.85$ x 10^{-12} F/m and permeability $\mu_0 = \mu \ / \ \mu_r = 4\pi$ x 10^{-7} H/m.

Then, four possible regions appear depending on the sign combinations of (ϵ, μ); since ϵ_0 and μ_0 are positive fundamental constants, negative values in $\epsilon = \epsilon_0$. ϵ_r and $\mu = \mu_0 \ \mu_r$ are due to the sign of the relative parameters ϵ_r and μ_r, respectively.

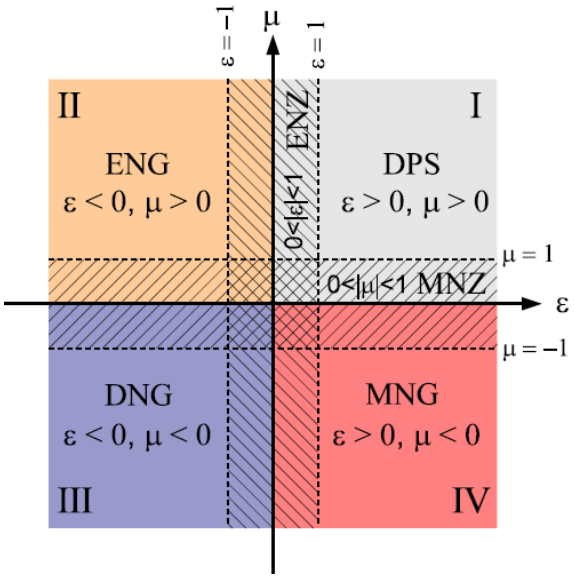

Figure 2-1: The ϵ-μ diagram [3].

An ϵ-μ diagram is illustrated in Figure 2-1 representing the materials that can be formed by the four sign combinations of (ϵ, μ).

Waves can only propagate in materials from regions I and III, where ϵ and μ are both positive (double-positive, DPS, or right-handed medium, RHM) or both negative (double-negative, DNG, or left-handed medium, LHM). Non propagating evanescent waves are found in regions II and IV, where $\epsilon < 0$ (epsilon negative, ENG) or $\mu < 0$ (μ negative, MNG). Finally, some other regions of interest might also be considered, such as the epsilon-near-zero (ENZ) where $0 < |\epsilon| < 1$, and the mu-near-zero (MNZ) where $0 < |\mu| < 1$.

DNGs are distinguished by the simultaneous values of $\epsilon < 0$ and $\mu < 0$. This fact has an impact on Maxwell's formulas' field equations. In phasor notation, a general definition of the Poynting vector $\vec{S}$ is eq. (2.2), where a time dependence $e^{+j\omega t}$ and a space dependence e^{-jkr} are assumed, and described as follow:

$$\vec{S} = \frac{1}{2}\vec{E}x\vec{H}_* \tag{2.2}$$

where the electric field $\vec{E}$ and the magnetic field $\vec{H}$ are defined by:

$$\vec{\beta} x \vec{E} = \omega \mu \vec{H} \tag{2.3}$$

$$\vec{\beta} x \vec{H} = -\omega \varepsilon \vec{E} \tag{2.4}$$

As a result, for an isotropic and homogeneous medium with $\epsilon > 0$ and $\mu > 0$, the electric field $\vec{E}$, magnetic field $\vec{H}$, and propagation vector $\vec{\beta}$ form a right-handed triplet, which is the basis for the definition of right-handed medium (RHM). However, by taking into account a medium with $\epsilon < 0$ and $\mu < 0$, the previous equations can be rewritten as follows:

$$\vec{\beta} x \vec{E} = -\omega |\mu| \vec{H} \tag{2.5}$$

$$\vec{\beta} x \vec{H} = \omega |\varepsilon| \vec{E} \tag{2.6}$$

demonstrating that the $\vec{E}$-$\vec{H}$-$\vec{\beta}$ vectors forms a left-handed triplet, and since the Poynting vector $\vec{S}$ is opposite in direction to the propagation vector $\vec{\beta}$, the energy and wavefronts travel in opposite directions in this medium (backward waves), which is known as a left-handed medium (LHM). This is reflected in the RHM and LHM $\vec{E}$-$\vec{H}$-$\vec{\beta}$ triplets illustrated in Figure 2-2.

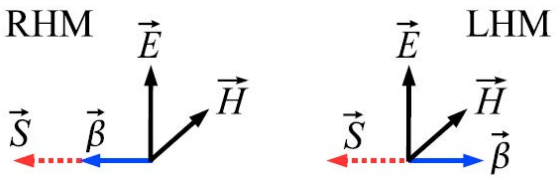

Figure 2-2: The right-handed and left-handed $\vec{E}$-$\vec{H}$-$\vec{\beta}$ triplets diagram [3].

2.2 Metamaterials Applications

Although DNG materials appear to be the most promising for implementation due to their unique backward-wave propagation feature and other related properties, the use of SNG metamaterials, either ENG or MNG, may offer some additional worthwhile applications.

The following are several remarkable applications focused on metamaterials:

- The negative index of refraction (NRI) ($\epsilon < 0$, $\mu < 0$) of a double negative medium is its distinguishing feature. When a plane wave travelling from a right-handed medium impinges on a left-handed medium, this fact causes a negative angle of refraction, which breaks Snell's law [4].

- Perfect flat lens. It is a direct result of using the NRI. Lenses are used to focus or shape radiation beams, but due to the wavelength limit, they have several limitations. Normal lenses are typically convex, requiring a large aperture to achieve good resolution; additionally, the image's details are contained in the near field, which decays exponentially (evanescent waves), contributing nothing to the final image. Negative index lenses can be concave or even flat, and they can focus the image as well as amplify evanescent waves that contribute positively to the final image while overcoming the wavelength limitation [5].

- Electromagnetic cloaking technology, which allows three-dimensional metallic objects to be rendered invisible. By introducing a required spatial variation in its constitutive parameters, cloaking allows control of the paths of electromagnetic waves within a metamaterial. This could be useful in stealth applications [6, 7].

- High impedance surfaces (HISs) [8], can be used to realise novel types of surfaces or reflectors which could behave like perfect magnetic conductors (PMCs), like in the case of Artificial Magnetic Conductors AMC [9], or Frequency selective surfaces FSSs. Perhaps the terminology of Electromagnetic Band Gap (EBG) structure is more widely and well known, than HIS, and this could be useful in the designing process of low-profile, compact, and high performance antenna systems, consisting of one or more antennas (array), and this study is focused on the use of such metamaterials to design, analyze, and fabricate antenna prototypes for modern wireless communication systems.

2.3 Electromagnetic Band Gap (EBG) Structures

2.3.1 EBG Definition

The electromagnetic band gap (EBG) structures are the most related to antenna applications among metamaterial applications, as stated in the previous section. They are mounted around or near the antennas, and may also be used in the antenna's feeding network, or even as part of the antenna itself.

So, what are electromagnetic band gap (EBG) structures? This section addresses this question from two aspects: definition of EBG structures and its application to antenna engineering.

Periodic structures abound in nature, and they've long piqued the interest of both artists and scientists. Exciting phenomena and amazing features appear when they interact with electromagnetic waves, like frequency stop bands, pass bands, and band gaps, among other things. When reviewing the literature, it is clear that different terminologies have been used depending on the application domain like Filter designs, gratings, frequency selective surfaces (FSS) [10], photonic crystals [11], and photonic band gaps (PBG) [12], and they are classified as "Electromagnetic Band Gap (EBG)" [13] under the broad terminology.

In general, electromagnetic band gap structures are defined as artificial periodic (or non-periodic) objects that prevent or assist electromagnetic wave propagation in a specific frequency band, for all incident angles and polarization states.

Typically, EBG structures are realised through the periodic arrangement of dielectric materials and metallic conductors. In general, they are classified into three groups based on their geometric configuration (see Figure Figure 2-3):

- three-dimensional volumetric structures.
- two-dimensional planar surfaces.
- one-dimensional transmission lines.

This thesis focuses on 2-D EBG surfaces, which have low profile, light weight, and low fabrication cost and are widely used in antenna engineering.

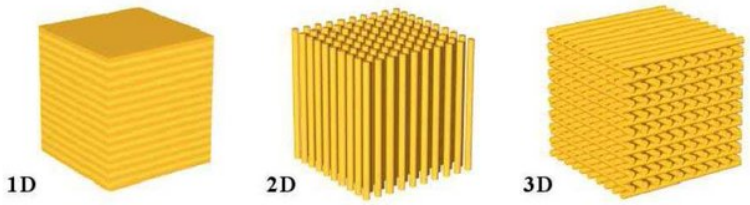

Figure 2-3: 1D, 2D and 3D EBG structures [14].

With respect to incident electromagnetic waves, planar electromagnetic band gap (EBG) surfaces exhibit distinct electromagnetic properties:

- The EBG structures show a frequency band gap through which the surface wave cannot propagate for any incident angles and polarisation states when the incident wave is a surface wave ($k_x^2 + k_y^2 \leq k_0^2$, k_z is purely imaginary).
- The reflection phase of the EBG structures varies with frequency when the incident wave is a plane wave ($k_x^2 + k_y^2 \leq k_0^2$, k_z has a real value). The reflection phase is zero degrees at a certain frequency, resembling a perfect magnetic conductor that does not exist in nature.

In the above equations, k_x and k_y are the wavenumbers in the horizontal directions, k_z is the wavenumber in the vertical direction, and k_0 is the free space wavenumber.

EBG also has some other exciting features, such as a high impedance and AMC, in addition to its band gap feature. A mushroom-like EBG surface, for example, has high surface impedance for both TE and TM polarizations. When a plane wave illuminates the EBG surface, an in-phase reflection coefficient similar to that of an artificial magnetic conductor is obtained. Furthermore, in the frequency-wavenumber plane, soft and hard operations of an EBG surface have been identified. These intriguing characteristics have resulted in a wide range of antenna engineering applications, ranging from wire antennas to microstrip antennas, linearly polarized antennas to circularly polarized antennas, and from the conventional to the novel concepts and reconfigurable antennas.

In brief, electromagnetic band gap structures are an important type of metamaterials. Their characterizations and antenna applications are the central focus of this thesis.

2.3.2 Analysis of EBG Structures

Various methods have been implemented to analyse the unique features of EBG structures. These techniques can be classified into three groups:

- Lumped element model.
- Periodic transmission line method.
- Full wave numerical methods.

A well-known lumped LC model was first proposed in [15], in which a parallel LC circuit model was used to describe the two-dimensional mushroom planar EBG (see Figure 2-4 (a)). The capacitance is originated from the electric coupling of adjacent metal patches, while the inductance comes from current following within the structure (see Figure 2-4 (b)). When the periodicity is small compared to the wavelength at the operation frequency, this lumped circuit model is valid. The LC circuit model is widely used for a wide range of 2D planar EBGs [8, 16], despite the fact that it is intrinsically derived for a specific EBG structure (the so-called mushroom EBG). This parallel LC circuit's impedance, which refers to the EBG

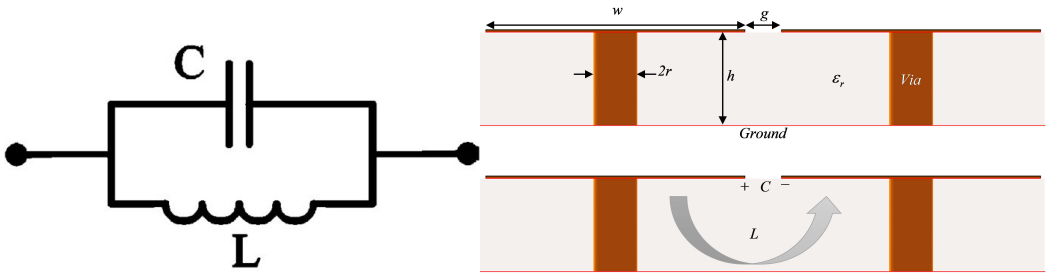

(a) (b)

Figure 2-4: (a) Equivalent circuit model with lumped elements LC for (b) Mushroom-like EBG [1].

structure's surface impedance, is provided by:

$$Z_s = \frac{jL\omega}{1 - LC\omega^2} \tag{2.7}$$

The resonance frequency at which the EBG structure acts as a high impedance surface can be calculated as follows:

$$f_0 = \frac{1}{2\pi\sqrt{LC}} \tag{2.8}$$

The EBG structures exhibit unique properties around this resonance frequency, such as in-phase reflection and frequency band gap properties.

Although this model is simple to comprehend, the results are inaccurate due to the simplified approximation of L and C.

Another widely used technique for analysing EBG structures is the periodic transmission line method [17]. Figure 2-5 shows an EBG transmission line model, with Z_P denoting the impedance of each periodic element and X_C denoting the coupling capacitor. This method takes into account the Floquet periodic boundary condition. The dispersion curve can be easily obtained after analysing the cascaded transmission line, providing more information than the lumped element method. The dispersion curve can easily identify surface wave modes, leaky wave modes, left- and right-hand regions, and band gaps. However, obtaining accurate equivalent Z_P and X_C values for the EBG structures is a challenge with this method. Some empirical formulas for simple geometries have been proposed, using multi transmission line (MTL) models, but the results are limited for general geometries.

Various numerical methods have been used in full wave simulations of EBG structures due to the rapid development of computational electromagnetics. Various research groups have used both frequency domain methods such as the MoM and FEM and time domain methods such as FDTD to characterise EBG structures. Figure 2-6, for example, depicts an FDTD model for the mushroom-like EBG analysis [18]. The versatility and accuracy in analysing different EBG geometries is one advantage of full wave numerical methods. Another significant advantage is the ability to calculate various EBG parameters such as surface impedance, reflection

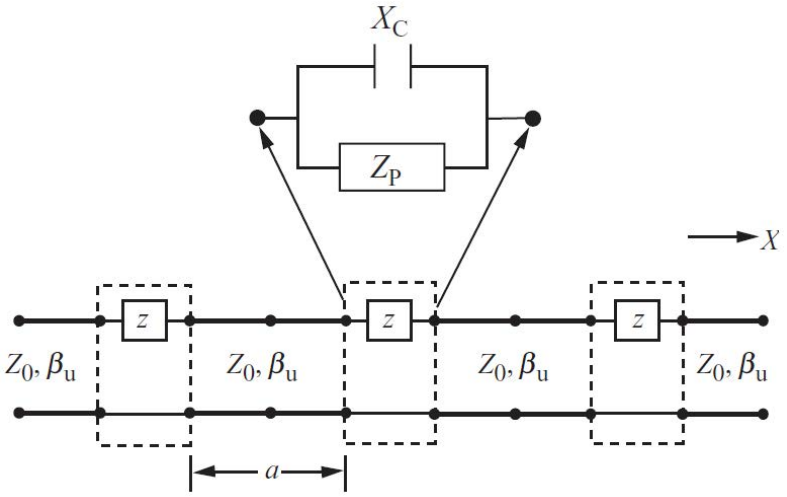

Figure 2-5: Periodic transmission line method for EBG analysis [17].

phase, dispersion curve, and band gaps.

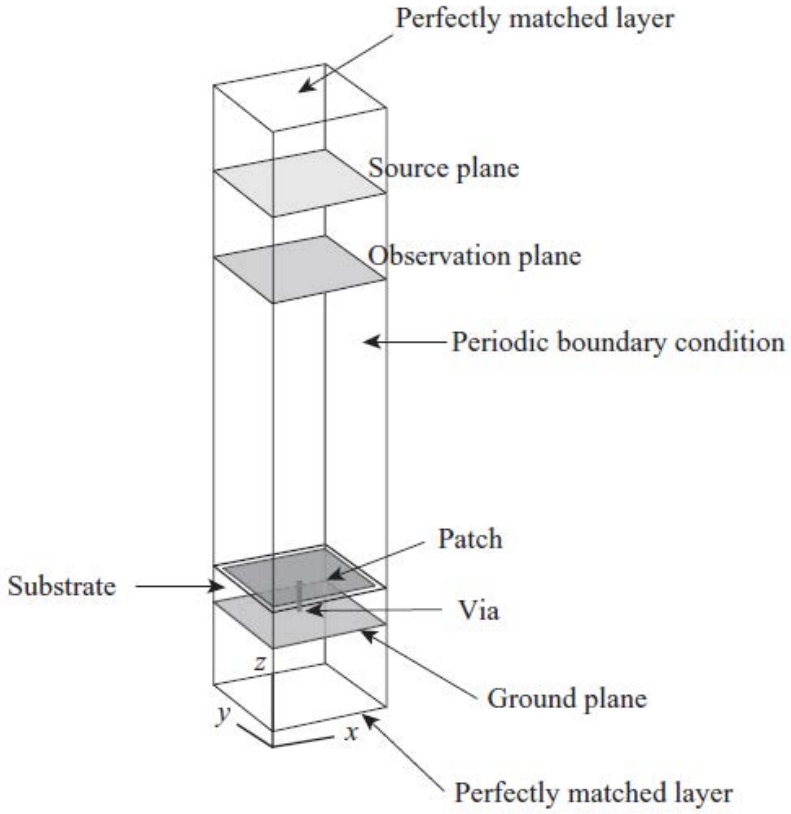

Figure 2-6: FDTD simulation setup for EBG analysis [16].

2.3.3 EBG/PBG Enhanced Microstrip Patch Antenna

In this section, a microstrip antenna based on an EBG structure, that meets the requirements of high gain and radiation efficiency, while keeping a degree of miniaturization compatible with component integration technology, in the architecture of wireless communication systems, was proposed and designed, to operate at 30 GHz with a characteristic impedance of 50 Ω. And simulated using CST microwave studio, the antenna's specifications were calculated according to [19].

The simulations of the return loss, the Voltage Standing Wave Ratio (VSWR) ratio, gain, and radiation patterns of the designed antenna over the frequency band of interest are presented. The simulation results reveal that this antenna achieved the desired requirements recommended in the 5G Communication systems.

Antenna Design

At the beginning of this design procedure, the substrate material was carefully selected based on the factors that affect the performance of the antenna, among them the substrate thickness, dielectric permittivity, and loss tangent. In the conventional and proposed design, Rogers RT/Duroid 5880 substrate (ϵ_r=2.2, tan δ= 0.0009) of 0.787mm thickness is selected for the antennas. RT Duroid 5880 substrate has low loss tangent and low dielectric constant. It also has characteristics of low water absorption, low electric loss and low moisture absorption. Roger substrate is the best for mm-Wave.

The Conventional Antenna

First, a rectangular patch of copper and dimensions of 4.47 x 3.51 mm^2 as a width and length, fed by a 50 Ohm microstrip line of 0.6mm wide (W_f) and 3.65mm long (L_f) with an inset of 1.11 mm (F_i) and a gap of 0.65mm (g) to achieve a good impedance matching between the feed line and the patch; is built on top of the substrate layer with a length, width and height of 11.3 mm, 11.8 mm and 0.787 mm respectively and of course a dielectric constant of ϵ_r=2.2. A conducting ground is employed on the other side of the substrate with the same dimensions as this

later. The patch alongside the feedline and the ground are copper-based material with a thickness of 0.035 mm (M_t). These parameters were calculated [19] in a way the designed antenna would resonates at a frequency of 30 GHz. A slot of 2 x 0.5 mm^2 was etched of the patch antenna to broaden the impedance bandwidth. The geometrical configuration of the conventional antenna is shown and summarized in Table 2.1 and Figure 2-7 respectively.

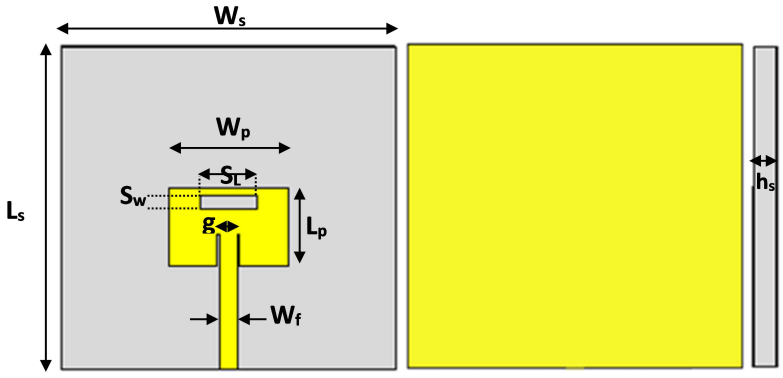

Figure 2-7: The geometry of the conventional antenna.

The Proposed EBG-Based Antenna

An EBG-Based structure is applied on the previous substrate leaving all parameters unchanged. The proposed structure is defined by a square latticed cylindrical air-gaped elements drilled into the substrate with a radius r and lattice (period) constant p (see Figure 2-8). This structure exhibits a distinct band gap for surface wave propagation around the operating frequencies. The existing of bandgap depends

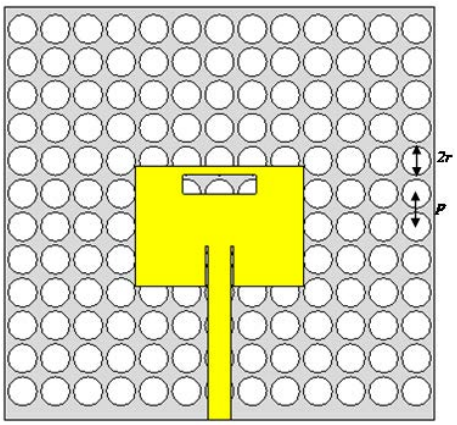

Figure 2-8: The geometry of the proposed EBG-Based Antenna.

Table 2.1: Conventional antenna specifications

Parameter	Value (mm)	Parameter	Value (mm)
Substrate width (Ws)	11.8	Patch length (Lp)	2.75
Substrate length (Ls)	11.3	Feed Length (Lf)	3.65
Substrate height (hs)	0.787	Feed Width (Wf)	0.6
Patch width (Wp)	4.2	Copper Thickness(mt)	0.035
Slot width (Sw)	0.5	Slot length(Sl)	2
Inset width (g)	0.8	Inset length(Fi)	1.11

on the periodicity of the lattice and the refractive index ratio of the material and the impurities that are added in the homogeneous substrate. Usually, the refractive index ratio must be greater than 2:1 (material to impurity) [20].

The lattice constant p and the filling ratio r/p are chosen to maximize the photonic band gap [21], and designed so that the operating frequency of 30 GHz falls within the stop band. The period p is 0.9 mm, and the filling ratio r/p is 0.44.

In order to analyze the band-gap of the proposed structure, direct transmission method is utilized [22]. Figure 2-9 shows the simulation model of this method.

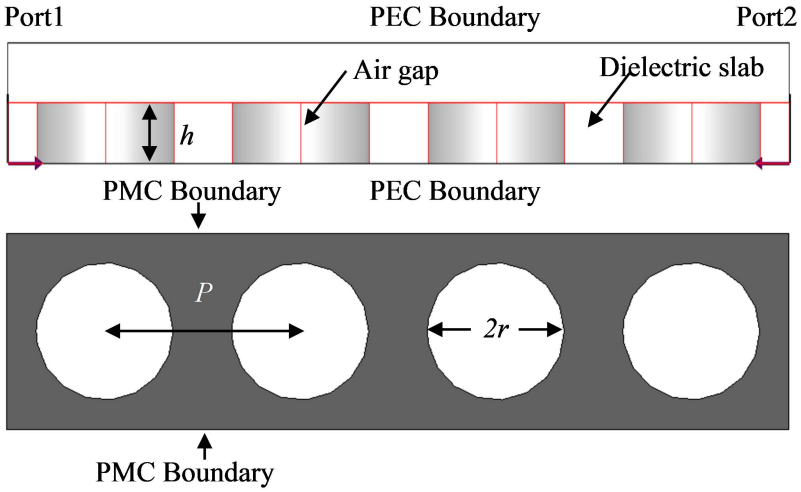

Figure 2-9: Simulation model of the direct transmission method.

As the number of air drilled holes increases, the rejection level also increases (see Figure 2-10), it is found that using 13 x 12 air gaped holes is enough to exhibit a band-gap between the frequencies of 29-33 GHz, in which the surface waves cannot propagate. Figure 2-11 illustrates the effect of the radius r (or the filling ratio r/p) on the bandgap property.

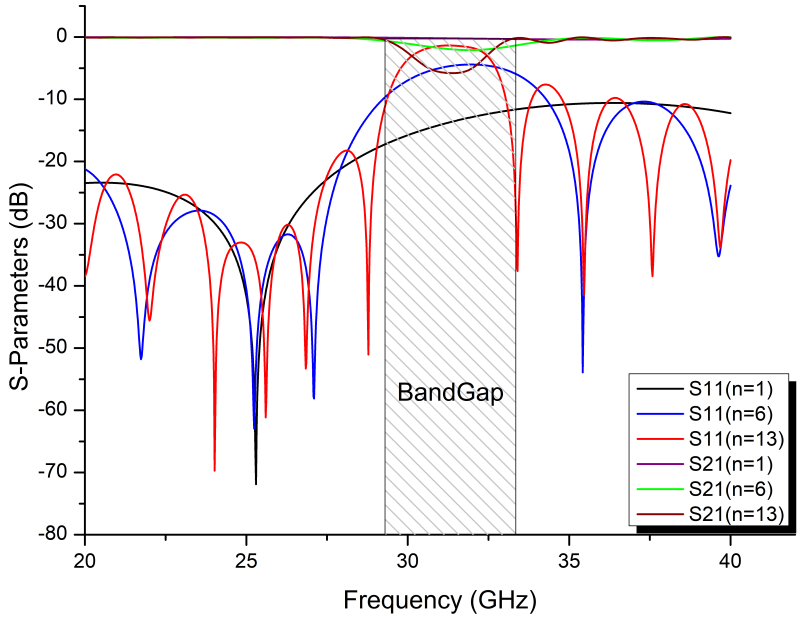

Figure 2-10: 1D electromagnetic bandgap

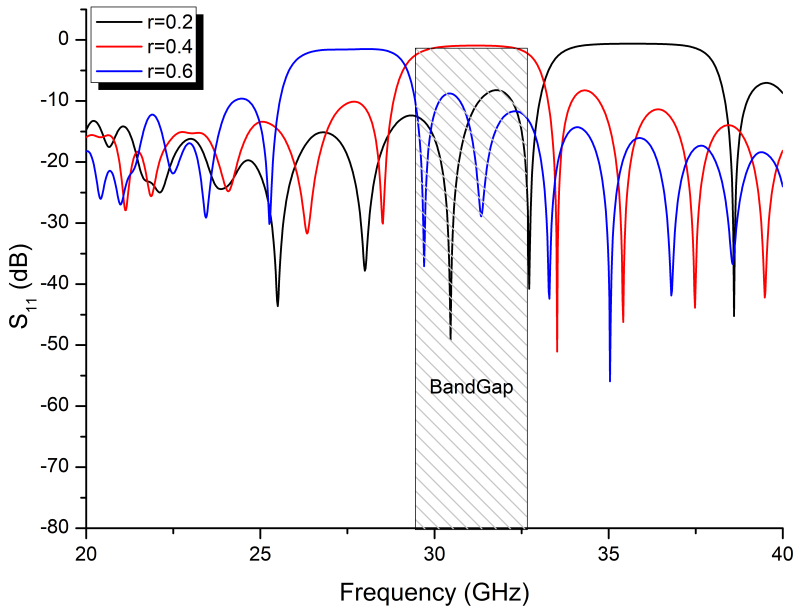

Figure 2-11: Effect of the radius r on the bandgap property.

Numerical Results and Discussion

The antenna's behavior was examined in an FDTD analyzing environment, hence CST Microwave studio (transient solver) with a frequency range from 0 to 40 GHz. The major simulation results of both antennas are given in this section.

Figure 2-12 compares the simulated S_{11} results of the conventional antenna and the EBG-Based one. The resonating frequency for the conventional antenna was

30 GHz, where as in the case of the EBG-Based antenna was 31 GHz, so a frequency shift that is, due to the fact that the presented EBG structure modifies the electromagnetic properties of the dielectric medium [23, 24].

It is noticed also that the proposed structure has shown a significant improvement in terms of the return loss and the -10 dB fractional bandwidth (FBW) with a -53.55 dB and 3 GHz for a return loss and bandwidth respectively, where in the case of the conventional microstrip antenna, both the return loss and bandwidth were -14.17 dB and 1.7 GHz, so a 73.5% and 40% improvement in terms of the return loss and bandwidth.

The simulated VSWR as a function of frequency for both antennas was less than 2 at the working frequencies, and they are 1.48 for the base antenna and 1.004 for the proposed antenna and is shown in Figure 2-13.

The VSWR is basically a measure of the impedance mismatch between the feeding line system and the antenna. The higher the VSWR, the greater is the mismatch. The minimum possible value of VSWR is unity and this lead to a perfect match just like in the case at hand.

For a further understanding of the antenna's performance, the radiation patterns of these antennas are presented in Figure 2-14, in both the E plane and H plane at the operating frequencies.

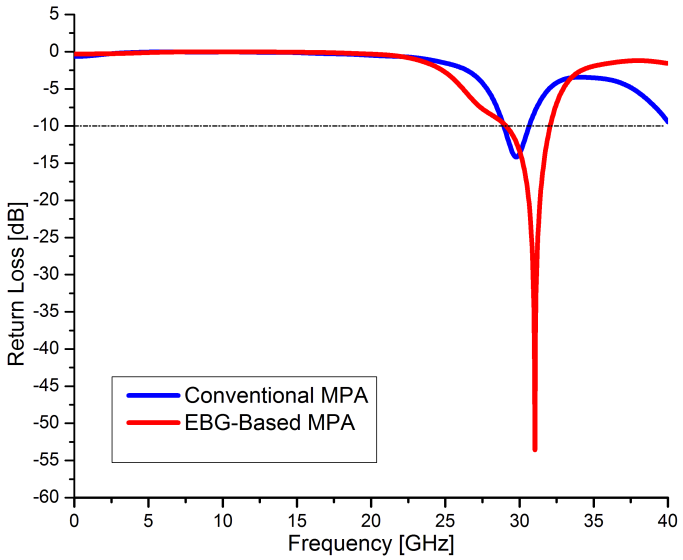

Figure 2-12: Simulated return loss versus frequency.

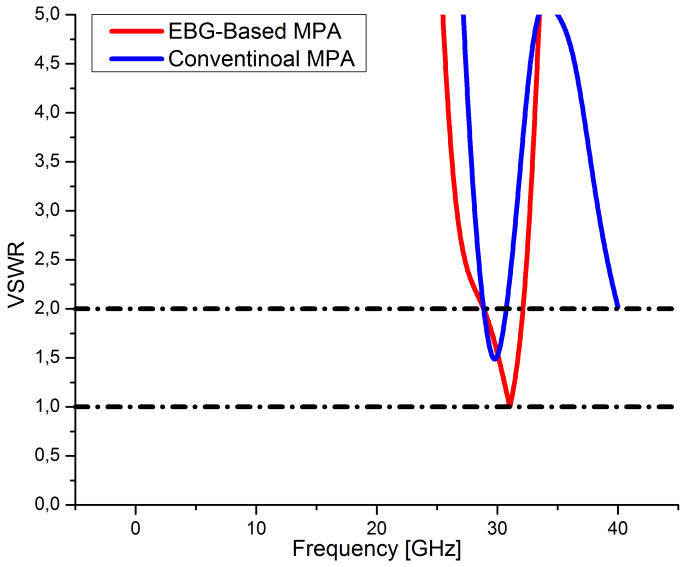

Figure 2-13: Simulated VSWR versus frequency.

The conventional antenna has an 8.1 dBi and -15.4 dB values for a front and back radiation respectively, where as in the case of the EBG-Based antenna, the front and back radiation were 10 dBi and -22.9 dB. So the best radiation performance is achieved by the EBG-Based antenna, because of the successful suppression of the surface waves, it's front radiation is highest, which is about 2 dBi higher than the conventional case. Since the surface wave diffraction at the edges of the ground plane is suppressed, the EBG antenna has a very low back lobe, which is more than 7.5 dB lower.

These radiation patterns are of a directional nature at the operating frequencies of interest and this is in a good agreement with applications of point-to-point (P2P) wireless communication systems, a technology where the utilization of BS (Base Station) or core network is not needed. Proximate devices can directly communicate with each other by establishing direct links, and due to the small distance between the D2D (Device-to-Device) users, power saving schemes are possible within the network, where it is not possible in the case of conventional cellular communication systems [25]. A directional antenna meets the required criteria to be a good candidate in the future wireless communication systems 5G, because it is essential to mitigate the effect of multipath fading with a minimum interference. The radiation efficiency of the proposed antenna is 83%, an 11% higher than the conventional

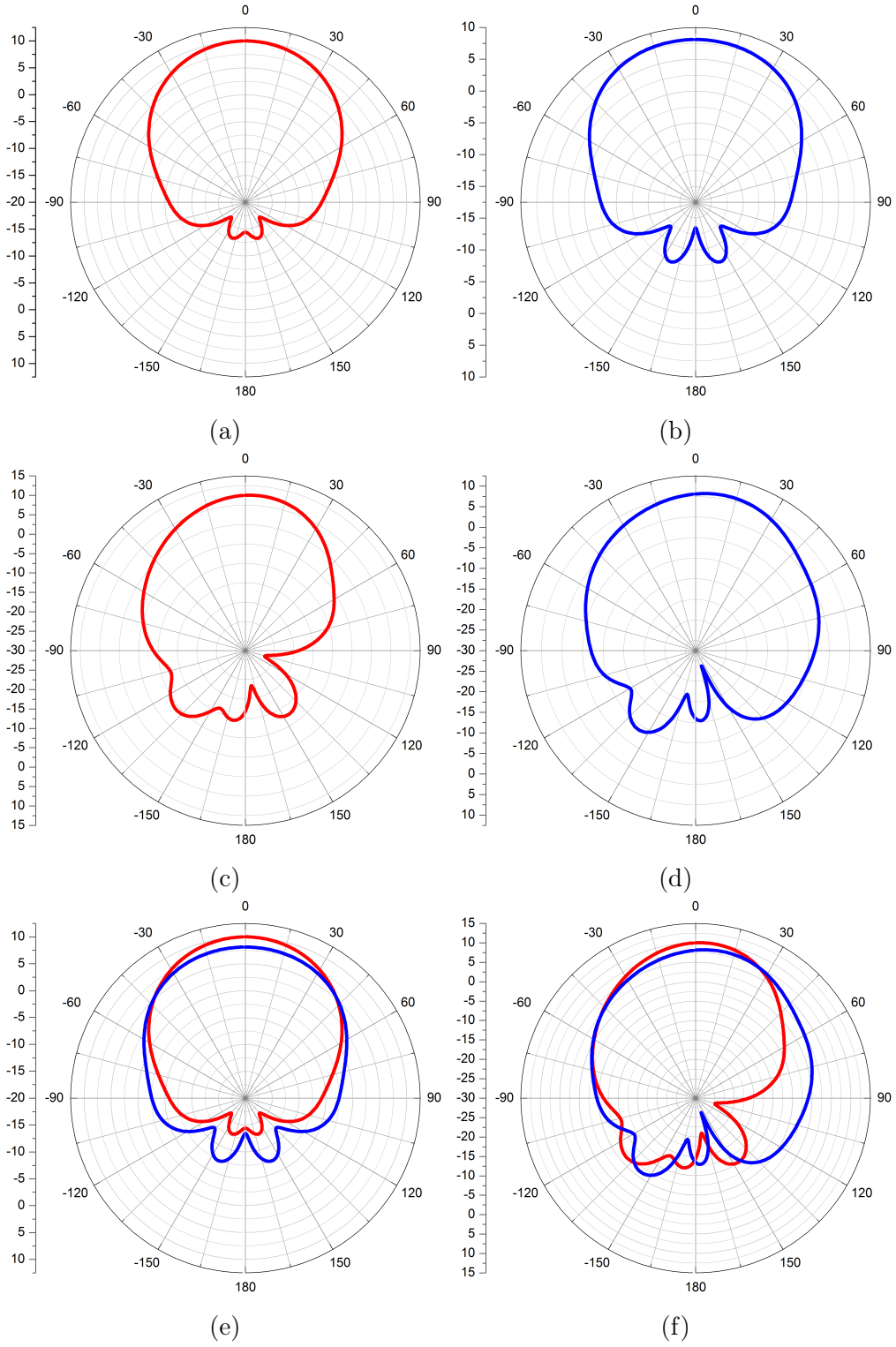

Figure 2-14: Simulated radiation patterns, (a & b) E-planes, (c & d)H-planes, (e & f) E-plane & H-plane (EBG-Based, red line, and Conventional antenna, blue line).

antenna with a radiation efficiency of 72%. The achieved efficiency is good in order to operate in the 5G applications.

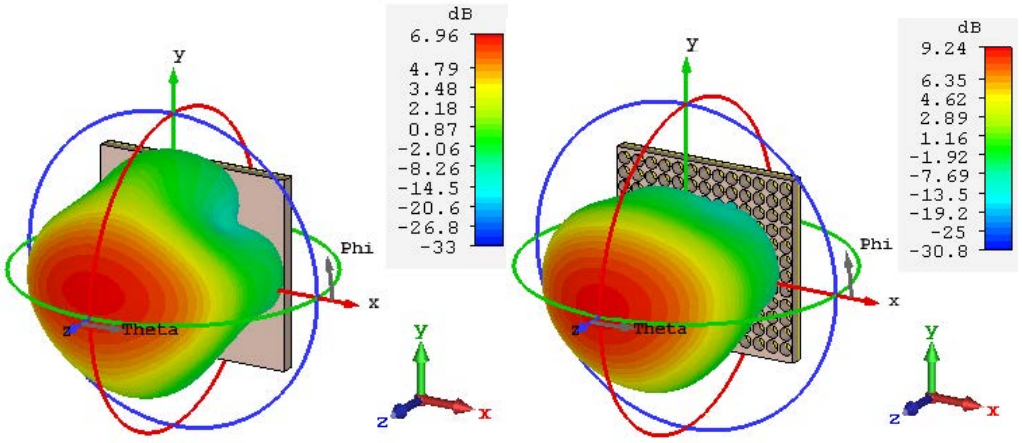

(a) (b)

Figure 2-15: Simulated 3D gain of (a) the conventional antenna versus (b) the proposed EBG antenna.

Table 2.2: Performance comparison between the conventional and the EBG-Based Antenna.

Ant.	Conv-MPA	EBG-MPA
S_{11} (dB)	-14.17	-53.55
$VSWR$ (dB)	1.48	1.004
Bandwidth (GHz)	1.7	3
Front Radia.(dBi)	8.1	10
Back Radia. (dB)	-15.4	-22.9
Peak gain (dB)	6.96	9.24

Figure 2-15 depicts the maximum peak gain achieved for (a) conventional antenna with a value of 6.96 dB at 30 GHZ and (b) EBG-Based antenna with a 9.24 dB peak gain at 31 GHz. So a 2.28 dB enhancement was successfully achieved.

A full comparison between the simulation results from the two antenna designs is summarized in Table 2.2.

Table 2.3 presents a comparison between the proposed antenna and other related works in terms of resonant frequencies, return loss and bandwidth as well as peak gain. It is noticeable from the comparison that the proposed antenna has the lowest return loss and the highest peak gain of -53.55 and 9.24 dB respectively, as well as a broader bandwidth alongside [26] when compared with other antennas.

Table 2.3: Performance comparison between the proposed antenna and other related works.

Ant.	[27]	[26]	[28]	[29]	This work
Freq. (GHz)	28.6	28.89	28.1	28.29	31
S_{11} (dB)	-24	-31	-31	-18.13	-53.55
BW (%)	2	3.1	1.6	1.69	3
Gain (dB)	5	7.73	7.59	7.72	9.24

Summary

In this example, an EBG-Based microstrip patch antenna is designed and simulated using the commercial simulator CST Microwave studio based on the FDTD analyzing method and was compared to the conventional base type of the antenna.

The EBG-Based MPA was proposed for 5G wireless communication systems operating at 30 GHz band spectrum. The antenna is a very low profile with a compact sized structure. Hence the compatibility with integration technology for devices with space constraints.

The obtained results show good performances in terms of return loss (S_{11}), bandwidth, gain, radiation patterns and efficiency, in comparing to the conventional MPA with an improvement of 73.5%, 40%, 24.6%, 19% and 11% respectively, because of the successful suppression of the surface waves by implementing Electromagnetic Band Gap (EBG) Structure.

A side from the previously stated performances, directional antennas such as the proposed one has the potential of being a good candidate for future 5G wireless communication systems.

2.3.4 AMC Enhanced Microstrip Patch Antenna

In this section, a probe fed microstrip patch antenna is proposed to operate at 30 GHz, and backed with an AMC structure, acts as a reflector to improve its front-to-back ratio and gain. The genetic algorithm is exploited by using the established interface between MATLAB and CST Microwave Studio through VBA language, to optimize and achieve the desired AMC unit cell parameters. The results yield an important improvement in terms of front-to-back ratio (low side lobes levels) and gain, compared to the conventional design, which makes it a good candidate for 5G.

AMC unit cell and antenna design

AMC unit cell

It's already known that the perfect electric conductor (PEC) has a 180° reflection phase for a normal incident wave, where as in the case of a perfect magnetic conductor (PMC), it has a 0° reflection phase, AMCs mimic the same property at the resonance frequency [30]. AMCs also exhibit the high surface impedance property (HIS) that can be used to suppress surface waves. As a result, the antenna's gain and side lobe levels are increased and reduced respectively [8], when an AMC structure is used as a reflector such as in our current case.

The AMC unit cell structure is a simple square patch on a Rogers (RT/5880) substrate with a relative permittivity (ϵ_r) of 2.2, a loss tangent (tanδ) of 0.0009 and a thickness of 0.787 mm. The dimensions of the unit cell is calculated using the equivalent LC model from [8], and are depicted in Figure 2-16 (a) alongside the equivalent model (Figure 2-16 (c)), where w_{amc} and g_{amc} are the patch width and the gap width, respectively. All above parameters where chosen carefully so the AMC's zero-reflection property is designed to operate around the frequency of 30 GHz. Figure 2-16 (d), shows the CST Microwave Studio simulation model applied from [31].

Figure 2-17 shows the simulated reflection phase response of the initial AMC unit cell. Its design parameters were: w_{amc} = 1.3428 mm, g_{amc} = 0.2 mm, and h_{amc} = 0.787 mm. These parameters yielded a resonant frequency of 28.77 GHz for the 0°

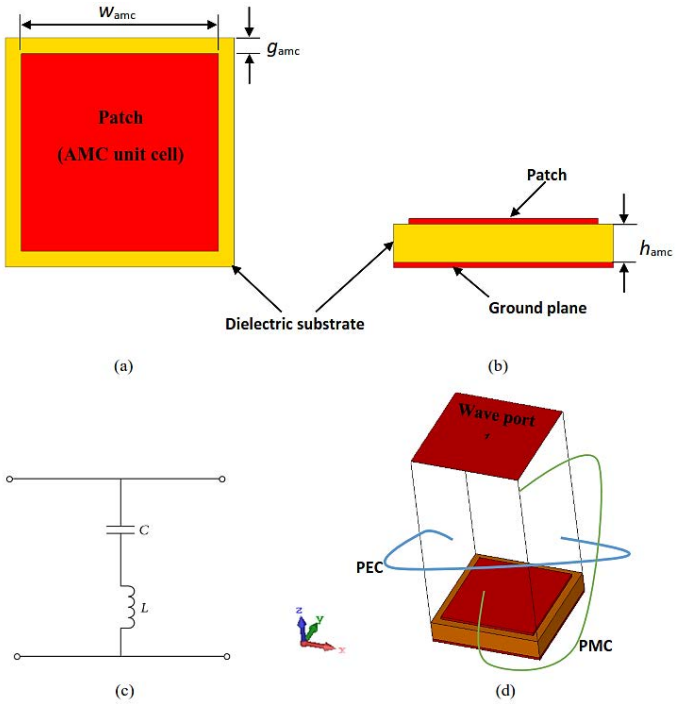

Figure 2-16: AMC unit cell. (a) Front view. (b) Side view. (c) Equivalent circuit. (d) Numerical Simulation model.

reflection phase, the ±90° reflection phase bandwidth was 13.44 GHz (22.77–36.21 GHz). So a frequency shift that needs to be adjusted according to the desired band of interest.

Genetic algorithm (GA) is used here, in combination with the full-wave simulation tool (CST), to optimize the parameters of the unit cell to fulfill the desired requirements. As we all know, genetic algorithm optimizers, are robust, stochastic search methods, modeled on the principles and concepts of the natural selection and evolution [32]. The flowchart of the proposed optimization process is depicted in Figure 2-18. The AMC's patch size w_{amc} and the gap g_{amc} were selected as state variables. The relative permittivity ϵ_r, and the height h_{amc} of the AMC's substrate are considered to be constant and equal to 2.2 and 0.787 mm, respectively.

The required zero-phased frequency of interest is f_{amc} =30 GHz, and the objective is formulated as a two-criterion function with respect to both the zero-phase frequency's position and the maximum bandwidth, the fitness function is minimized

and defined as:

$$F = \left(\frac{f_{amc\_\max} + f_{amc\_\min}}{2} - f_{amc} \right)^2 - \left(\frac{f_{amc\_\max} - f_{amc\_\min}}{f_{amc}} \right) \tag{2.9}$$

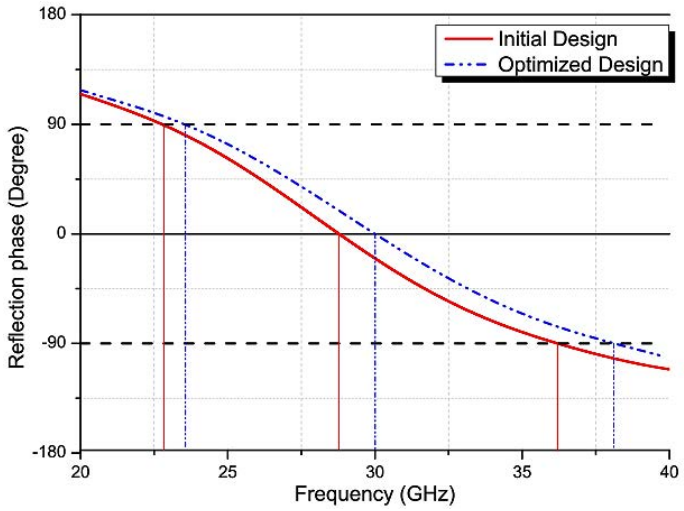

Figure 2-17: Simulated refection phase of the initial AMC unit cell and the optimized one.

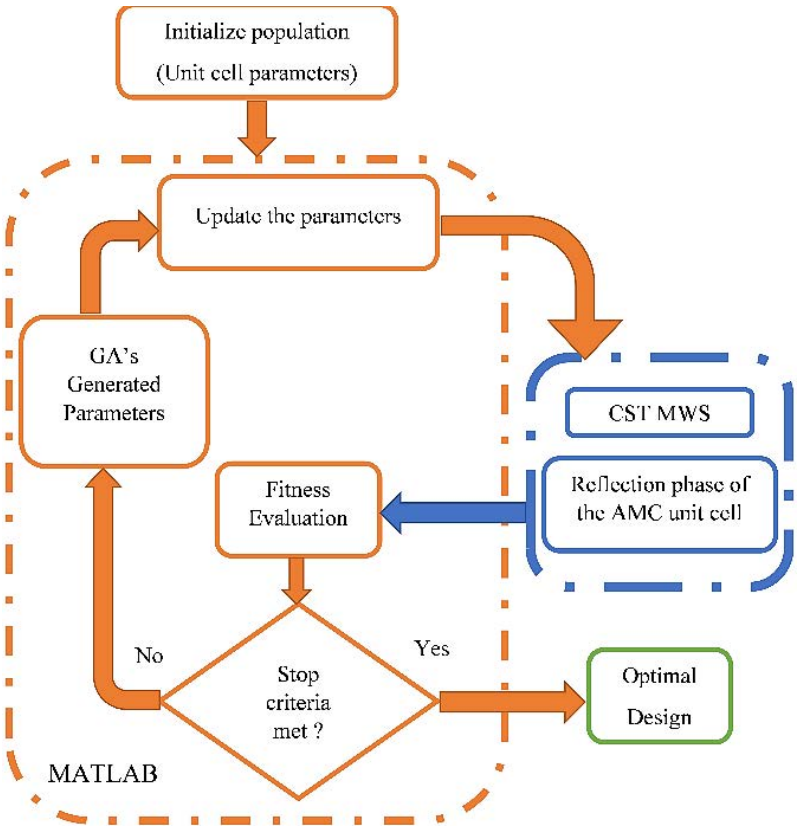

Figure 2-18: The flowchart for genetic algorithm parameters optimization.

Where and are the upper and lower limit of the ±90° reflection phase bandwidth. The minimum and the maximum value of the patch size w_{amc} are set to 1 mm and 2 mm, respectively, the gap g_{amc} is defined within the range of [0.1-0.5] mm. The initial population consists of 50 random individuals, going through the process of selection (Roulette), the probability of the crossover is 100 % and the probability of the mutation is set to 1 %, and the number of generations is set to be 50. After reaching the maximum number of iterations, the final optimized parameters for our designing scenario are given as follow: w_{amc} = 1.2477 mm, g_{amc} = 0.2 mm, h_{amc} = 0.787 mm, and the reflection phase diagram for the best optimized individual is depicted in Figure 2-17.

The proposed design

The previously optimized AMC unit cell, is applied as a reflector to enhance the performances of a probe fed microstrip patch antenna, with a rectangular radiator of 3.53 x 2.55 mm as a width and length, printed on top of a Rogers RO/3003 dielectric slab, with a relative permittivity (ϵ_r) of 3, a loss tangent (tanδ) of 0.001 and dimensions of 7.06 x 5.11 x 0.254 mm for a width, length and thickness respectively. The characteristic impedance of the coaxial feed line was 50 Ohm, and the line passed through a drilled hole on the AMC reflector to feed the patch. These parameters were calculated [19] in a way, so the designed antenna would resonates at a frequency of 30 GHz. The proposed antenna is suspended at a height h_z above the AMC surface, which is an array of 12 x12 unit cells (17.37 x 17.37 mm). Figure 2-19 shows the geometry of the proposed antenna.

The distance, h_z, needs to be chosen carefully to enhance the antenna's performances, by reflecting the back radiation. Therefore, a parametric study with different spacing h_z is needed to illustrate the performances enhancement.

Simulation results and discussion

The simulated return loss s_{11} for both the conventional antenna and the AMC backed one, is depicted in Figure 2-20. By varying the distance h_z (0-10 mm), different return loss values were obtained, and the best one was -52.72 dB at a

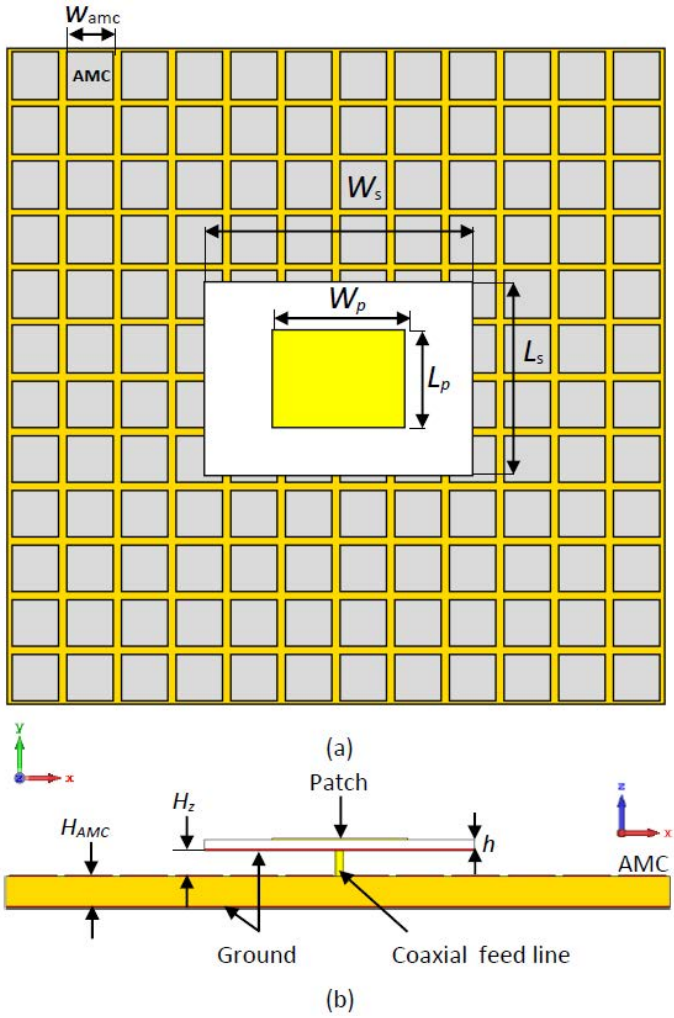

Figure 2-19: Geometry of the optimized proposed antenna on the AMC surface: (a) top view, (b) side view.

distance of h_z =4.6 mm, with a resonance frequency of 30.37 GHz in comparison to the conventional antenna, where the return loss was -30.6 dB at a resonating frequency of 30 GHz, so a frequency shift that is, due to modified electromagnetic properties introduced by the AMC surface. Both antenna's impedance bandwidth is around 3.53 % (1.06 GHz). A significant improvement in terms of return loss is achieved and is about 72.29 %.

Figure 2-21 illustrates both gain and side lobe level (SLL) of the proposed antenna, in function of the spacing between the antenna and the AMC surface. The maximum peak gain of 9.28 dB is achieved at a distance of 0.5 mm with a side lobe level of -18.9 dB, while the peak gain of conventional antenna was 7.34 dB and the side lobe level was -15 dB. So an increase of 26.43 % (1.94 dB) in peak gain and 26

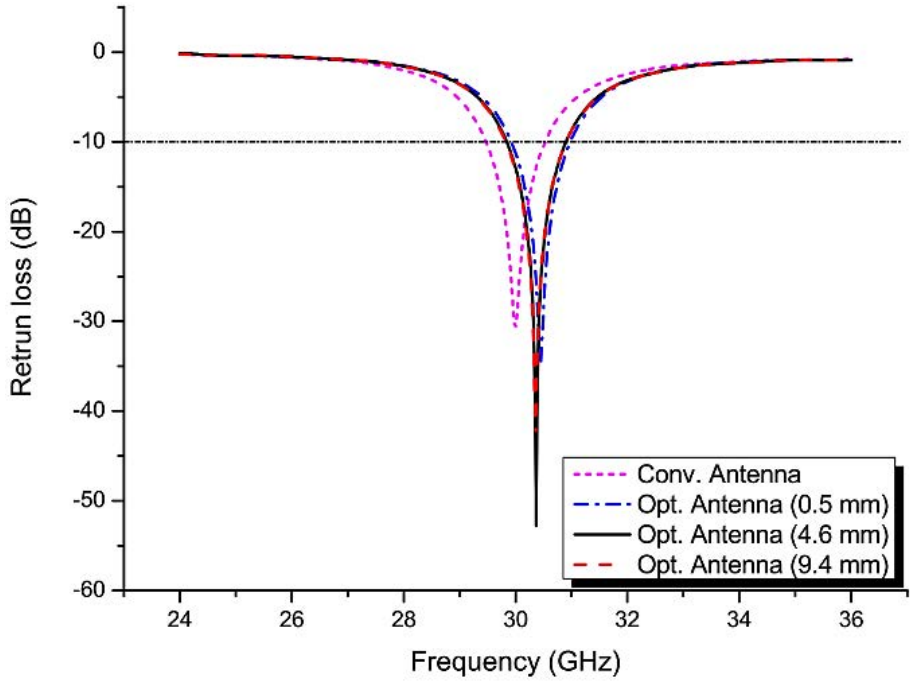

Figure 2-20: Simulated return loss versus frequency.

% (-3.9 dB) enhancement in terms of side lobe level.

The lowest SLL value was -24.6 dB at a distance of 9.4 mm with a gain of 8.55 dB. Resulting in an improvement of 63.8 % (-9.57 dB) in SLL and an increase of 16.49 % in terms of peak gain. So a trade-off between choosing higher peak gain or lower SLL is a must. From above findings, the maximum front-to-back performance is achieved at a spacing h_z of 9.4 mm (see Figure 2-21), due to the effectiveness in back radiation suppression (surface waves), when incorporating the antenna with an AMC based reflector. The antenna's gain could be further enhanced by increasing the number of cells of the AMC surface.

Summary

In this example, a probe fed microstrip patch antenna, suspended over an AMC based reflector, was investigated and simulated. A parametric study was conducted, by varying the spacing between the AMC reflector and the suspended microstrip antenna. Most importantly, the proposed design, effectively, improved the antenna's gain up to 9.28 dB, and also improved the side lobe level as low as -24.57 dB, due to the successful suppression of the surface waves. Moreover, the overall size

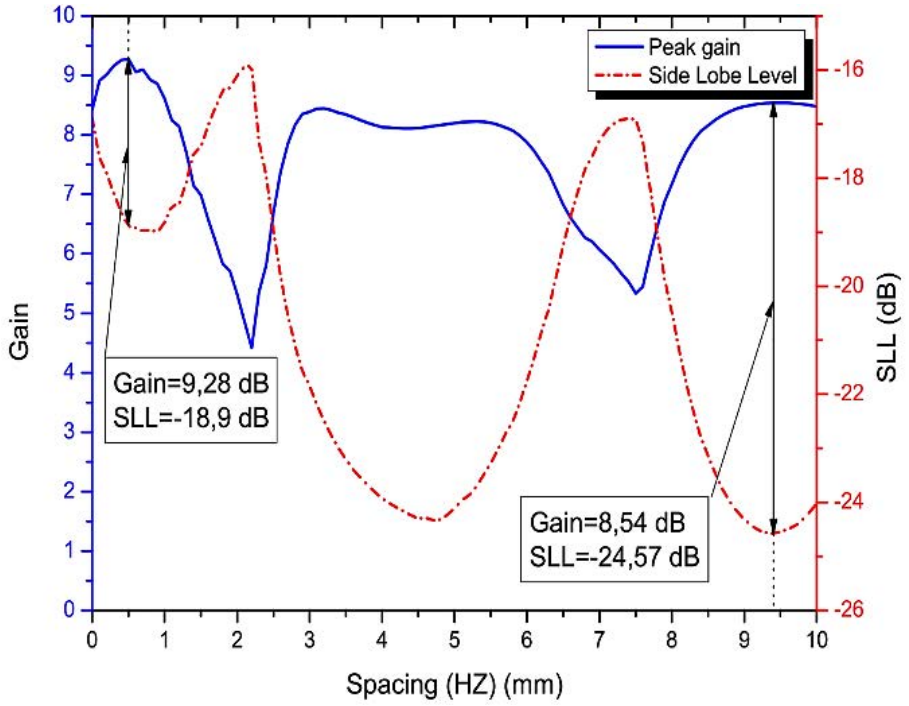

Figure 2-21: Simulated gain and SLL of the proposed antenna at different spacings of h_z.

of structure is compact (17.4 x 17.4 mm), with relatively high gain, makes the proposed design an extremely attractive candidate for the next generation of mobile communication systems 5G.

2.4 Frequency Selective Surfaces FSSs

2.4.1 Definition

A Frequency Selective Surface (FSS) is a periodic, planar arrangement of mostly metallic elements on a dielectric layer. It is constructed in tandem with electromagnetic waves in order to "tailor" an electromagnetic link, in the free-space environment. The FSS regulates the flow of electromagnetic energy by acting as a barrier for waves propagating along that link. The FSS's transfer function manipulates the wave's spectral content. As a result, some of the wave's frequency constituents are blocked, while others pass through the FSS fence. In another sense, an FSS is similar to a filter in circuit theory. In electromagnetic engineering, FSS structures are also known as spatial filters due to their filtering effects.

2.4.2 FSSs and well-known metamaterial structures

Some well-known structures, such as high impedance surfaces (HIS), can be thought of as evolved versions of FSSs, in which FSSs are combined with metallic ground planes and metallic pins (vias). As a result, they can provide two important characteristics at the same time: artificial magnetic conductor (AMC) and electromagnetic band gap (EBG).

Because currents cannot travel across the gaps between the patches, an FSS of metallic patches, such as the one shown in Figure 2-22 (a), can effectively suppress surface waves. It is partially reflective in the frequency range where it prohibits surface waves. This latter can propagate only at very high frequencies, when the effective capacitors between neighbouring plates behave as shorts. As a result, this FSS transmits low-frequency signals while reflecting high-frequency signals.

The inductive FSS, which is shown in Figure 2-22 (b) is the complementary counterpart of the capacitive one, which consists of an array of square slots. The inductive structure has complementary transmission spectra because it is the complementary of the capacitive structure. As a result, it transmits high-frequencies while reflecting low-frequency waves [33].

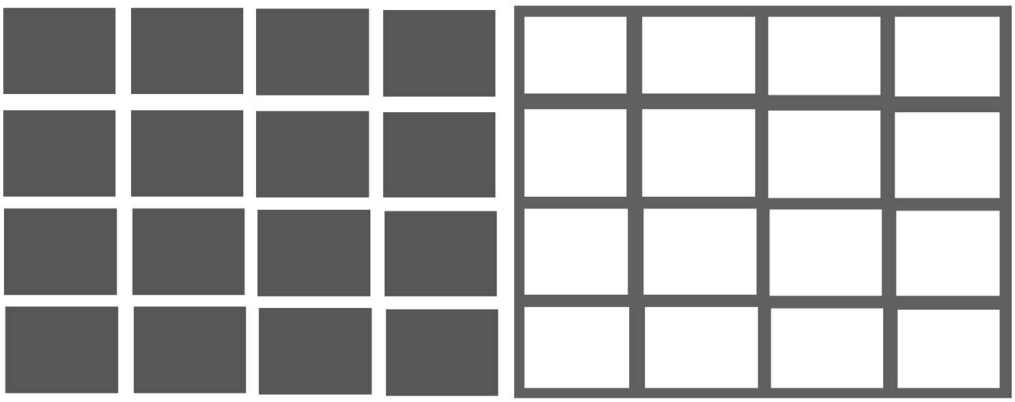

(a) (b)

Figure 2-22: FSS elements types: (a) patch (capacitive) and (b) aperture (inductive).

Waves that are short in comparison to the diameter of the holes will easily pass through the mesh on the inductive surface, while longer waves will see the sheet as continuous metal. As a result, long wavelengths are transmitted while short wavelengths are reflected by the metal sheet. The capacitive sheet is not completely

reflective at low frequencies, where it can prevent the propagation of surface waves. This latter can easily propagate along the continuous metal wires while the inductive sheet is reflective at low frequencies.

When a ground plane is added to a capacitive FSS, the structure becomes completely reflective, with the favourable reflection phase properties of high-impedance surfaces, but surface wave propagation is still possible. The important properties of high-impedance surfaces, such as in-phase, 100 percent reflection, and suppression of surface current propagation, are only obtained when both the ground plane and the vias are included [34].

2.4.3 FSSs in antenna engineering

FSSs have been used, to widen the operating band of backing reflectors and to enhance the performance of broadband reconfigurable antennas, as superstrates and as reflectors. In This thesis, the use of FSSs as reflectors to UWB antenna, is one of the main objectives.

FSSs as UWB reflectors

For broadband and ultra-broadband applications, FSSs can be used effectively in a planar reflector design. The basic concept is to create a single or multilayer FSS structure, with each layer providing reflectivity for a different frequency band. Each reflective plane is positioned at a suitable distance from the antenna, resulting in reflections from various layers and thus increasing the composite reflector's usable range.

The wave radiated toward the FSS is reflected when an antenna is placed at a distance H_z (mm) above it. This reflected radiation would be added to the direct outgoing wave radiated in the opposite direction of the FSS reflector from the antenna. When the two wave components are added in phase, constructive interference is expected to occur, resulting in the maximum gain of the antenna in the presence of the FSS reflector.

Please refer to chapter 4 for more information on the operation mechanism of the FSS/antenna combination.

Several UWB antennas based on such reflectors were reported in the literature, to verify its functionality. In [35] the antenna was placed above the reflector at a distance of about $\lambda/4$ at the center frequency of 6 GHz , and a maximum gain of 9.5 dBi was achieved at 4.2 GHz, with only 1.5 dB gain variation over the frequency range of 3 to 10 GHz.

In [34] a rectangular slot antenna is suspended over an Ultra wideband optimized FSS reflector at a height of 10 mm, and this latter has a very small effect on the radiator's impedance bandwidth, compared to the gain, which is significantly improved due to the reflector's presence.

The average peak gain of the feed antenna alone was 5.7 dBi, while the average peak gain with the FSS reflector was around 10.9 dBi.

In brief, The detailed examples of various FSS antenna applications in the literature, demonstrate the structures dependability and flexibility, as well as their ability to enrich antenna research and lead to further innovations. Meanwhile, FSSs are extremely sensitive due to their dependability and flexibility. As a result, their design should be meticulous in order to achieve the desired results.

2.5 Summary

In this chapter, a brief and general overview on Metamaterials and Electromagnetic Band Gap structures (EBG) in particular, is discussed, alongside the analysis of such periodic structures and the exploitation of full-wave solvers in a few introductory texts and tutorials describing the correct set up of the analysis have been provided. Moreover, these texts are often incomplete and unclear. Therefore, a detailed description of the critical settings of unit cell modeling for the correct characterization of EBGs, FSSs, AMCs and PRS structures, are discussed in the next chapters and sections, and the findings are compared to related works in the literature.

Chapter 3

Analysis and Design of a Compact patch antenna using an optimized EBG structure

3.1 Introduction

The microstrip antenna plays a vital role in the fastest growing wireless communications sector. Today, to establish a communication link between wireless devices, we need an antenna, which is conformal, compact, cheap, and easy to fabricate.

Microstrip patch antennas are light in weight, and have lower fabrication cost, but they do suffer from the inherently narrow impedance bandwidth, low gain and efficiency due to dielectric and conductor losses, and are relatively large in size.

Two of the most important aspects in microstrip antenna design, are to widen the narrow bandwidth, and size miniaturize of the patch antenna.

The narrow bandwidth can be expanded by increasing the substrate thickness. However, by doing so, stronger surface waves are excited in the dielectric slab. As a result, the radiation efficiency and patterns of the antenna are further degraded. In [36] parasitic patches incorporated with shorting vias were introduced on the microstrip patch antenna to form multi-resonant circuit so that the bandwidth is improved, because increasing the resonance modes around the main one, would consequently increases the impedance bandwidth, then by simply adding shorting

vias, the surface current distribution on the patch antenna is changed, reducing the input impedance of the antenna toward 50 Ohm at some frequencies, resulting in the increase of the impedance bandwidth. Another way of broadening the bandwidth is to introduce slots into the patch without additional size [37]. In [38] slot loading techniques, symmetrical rectangular microstrip feed-line, and notch-loaded ground plane, are used to enhance the impedance bandwidth. Another important aspect in microstrip antenna designs is to miniaturize the patch size. In [39] a novel kite-shaped slot utilized in the radiating patch is proposed for antenna miniaturization in both active patch area and volume (i.e., 26 and 50%). The conventional half-wavelength size is relatively large in modern portable communication devices. Increasing the dielectric constant of the substrate is a simple and effective way in reducing the antenna size [40].

Microstrip antennas on high dielectric constant substrate are of growing interest due to their compact size and conformability with integrated architecture circuits. However, there are several drawbacks with the use of high dielectric constant substrate, namely, narrow bandwidth, low radiation efficiency, and poor radiation patterns, which result from strong surface waves excited in the substrate. Hybrid substrates to enhance the gain of the antenna by implementing a ferrite ring without compromising the bandwidth [41].

To overcome the drawbacks of using the thick and high dielectric constant substrate, microstrip patch antennas are incorporated with different materials used to enhance potential parameters of the antenna. Among them, Electromagnetic Band Gap EBG structures are the most appropriate [42].

The EBG structure is defined as artificial periodic (or sometimes non-periodic) objects that prevent or assist the propagation of electromagnetic waves in a specified band of frequency for all incidence angles and all polarization states. It prevents the propagation of the surface wave excited by the patch antenna [43]. Circular mushroom-like substrate was used in [44] to improve the antenna's gain. In [45] the Sierpinski fractal-shaped EBG is used to address the low gain problem, where as for [46], gain and front-to-back ratio were enhanced using a novel elliptical EBG structure. For a highly effective medium ratio and size miniaturization, a cohesive

symmetric hook-C shape inspired metamaterial for S-band application was used [47]. In [48] a Split-Ring ResonatorSRR based metamaterial structure is used to improve the electromagnetic Specific Absorption Rate SAR in many wireless communication systems like WiMAX. Another way of improving the antenna's performance, is by using Frequency Selective Surface structures FSS, like in the case of [49] and [50], where FSS layers were proposed as superstrates to form a Resonant Cavity Antennas RCA, and the results yielded an impressive improvement in terms of directivity and peak gain while keeping a degree of compactness.

The electromagnetic band gap EBG structure is applied in patch antenna design to overcome the undesirable features of the high dielectric constant and thick substrates while maintaining the desirable features of utilizing small antenna size.

In this chapter, a microstrip antenna based on the mushroom-like EBG structure is proposed and designed to operate at 5.8 GHz. The main characteristics of the proposed design is its ability to increase the gain, directivity, return loss and the total efficiency of the antenna without affecting the geometric parameters, which makes it applicable for wide range of RF devices, operating at the chosen resonance frequencies. The simulated results using CST microwave studio compared to the conventional design and other related works have demonstrated attractive performance in terms of impedance matching and bandwidth, compact features (light weight, small sized, low cost), and high gain and efficiency.

3.2 Analysis and design

In this section, a probe fed (0.5 mm in radius) microstrip patch antenna on a thin, thick and step-like substrate designs, are discussed alongside the proposed EBG-based structure, and investigated using the Finite-difference time-domain (FDTD) method in Computer Simulation Technology CST microwave studio. Rogers RT/-Duroid 6010 (ϵ_r=10.2, tan δ=0.0023) commercial laminate is chosen in this study as the substrate, with a size of 1λ x 1λ (where λ is the free space wavelength at the resonance frequency), the feed location was optimized for all designs to give a good impedance matching.

3.2.1 Conventional antenna designs

To study the effect of the substrate's thickness on the performances of the microstrip patch antenna (MPA), two configurations of different heights are simulated on the previously stated substrate with h_1 = 1.27 mm and h_2= 2.54 mm, and by tuning the patch size and the feed location, both antennas match well to 50 Ohm, around the desired resonance frequency of 5.8 GHz. The patch width and length for the antenna with thin substrate(h_1 = 1.27 mm) were 7 and 5 mm respectively, whereas in the case of the design with thicker substrate (h_2= 2.54 mm), its patch width and length were 6.7 and 4 mm respectively (see Figure 3-1(a)).

Another patch antenna design is investigated, as shown in Figure 1b. The idea behind it is to use a thick substrate under the patch with a thickness of 2.54 mm, which helps to keep the compact size and bandwidth and use a thin substrate (1.27 mm) around the patch, which could reduce the surface waves. This geometry is like a stair step [51]. Note that the patch size is 6.7 and 4 mm for a width and length respectively.

3.2.2 The proposed EBG design

An EBG-Based structure is applied on the previous step-like structure surrounding the substrate under the patch, leaving all parameters unchanged. It consists of a

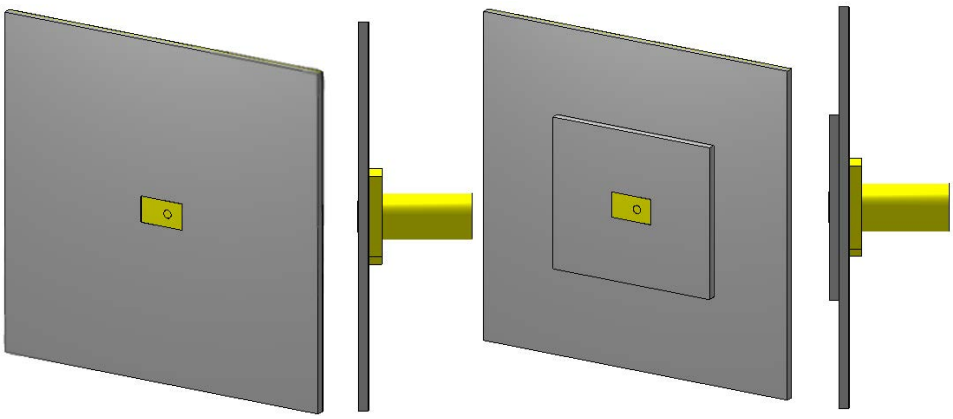

(a) (b)

Figure 3-1: Patch antenna on (a) a simple and (b) step-like substrate, geometry and cross section.

lattice of metal patches, connected to a solid metal sheet by vertical conducting vias penetrating a dielectric medium. It is the mushroom-like EBG structure (Figure 3-2), it was first proposed in [8].

This structure exhibits a distinct band gap or stop band for surface wave propagation, and can be explained and modeled by a simple LC filter network. The inductor L results from the current flowing around the patch through the vias and ground metal sheet, at the same time the fringing effect between two adjacent patches can be considered as a capacitor C.

The values of the inductor L and the capacitor C are determined by the following formula [15]:

$$L = \mu_0 h \tag{3.1}$$

$$C = \frac{w\varepsilon_0(1+\varepsilon_r)}{\pi}\cosh\frac{(w+g)}{g} \tag{3.2}$$

μ_0 and ϵ_0 is the permeability and permittivity of the free space respectively. The parameters h, w, and g are the height of the substrate, the EBG's patch width, and the gap between two neighboring EBG patch units, alongside the via's radius r, and they are depicted in Figure 3-2 (a).

Moreover, the frequency band gap is [15]:

$$\omega = \frac{1}{\sqrt{LC}} \tag{3.3}$$

$$BW = \frac{\Delta\omega}{\omega} = \frac{1}{\eta}\sqrt{\frac{L}{C}} \tag{3.4}$$

Where η is the free space impedance, which is 120π.

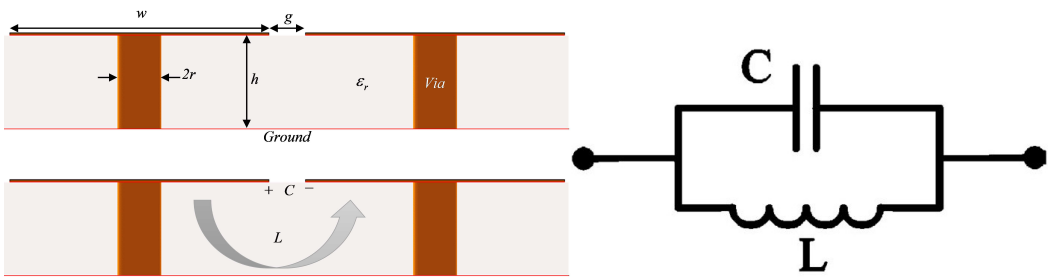

(a) (b)

Figure 3-2: (a) Mushroom-like EBG (b) Equivalent LC circuit.

It should be noted that the presence of the via is responsible for the band-gap existence, and the via's radius r affects the band-gap by moving it to higher frequency region when$r$ is increased, and the band-gap is also enlarged, because the effective area between the top and bottom conducting sheets is reduced, and the total equivalent capacitance is decreased, and so the resonant frequency becomes higher, and the band-gap is expanded because it's proportional to $\sqrt{LC}$ [52].

Due to complex behavior of EBGs, stochastic methods can be successfully implemented. A combination of a full-wave numerical tool (CST) with a global optimization algorithm (GA) was successfully used here to optimize the parameters of the unit cell to fulfill the needed requirements. The computational process is controlled from MATLAB, through an interface with CST for the full-wave dispersion analysis, using Visual BASIC for Application (VBA).

The Bloch-Floquet theorem (see Figure 3-3) is used for the dispersion analysis, which describes the wave propagation in infinite media consisting of periodic repeti-

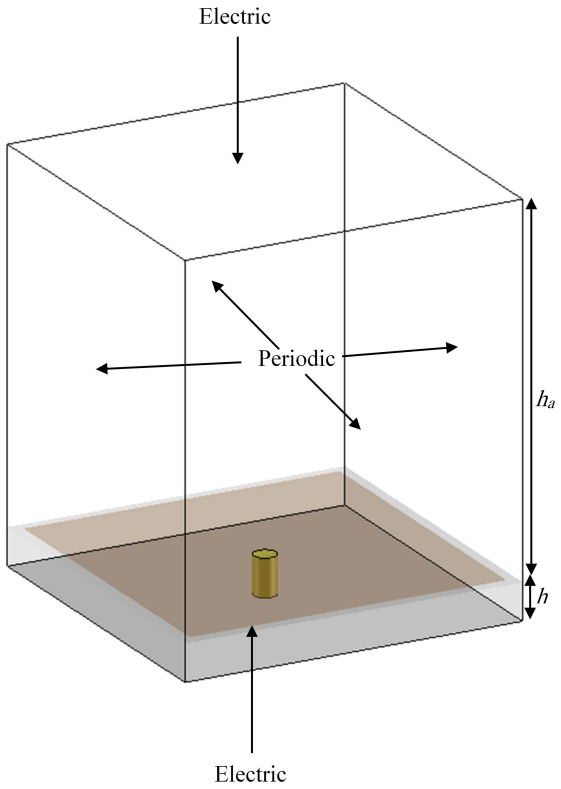

Figure 3-3: Numerical model of a mushroom-like EBG unit cell for dispersion diagram calculation (ha=10h).

tion of the unit cell. The theorem states that the properties of wave propagation in a periodic media can be fully described considering only one unit cell and applying periodic boundary conditions at its edges [53]. But since the eigenmode solver in CST Microwave Studio does not support open boundaries, the top and the bottom of the model should be defined as perfect electric (see Figure 3-3). A relatively small height of the air box h_a could be sufficient considering the fact that the surface waves are concentrated mainly inside the substrate and at the substrate/air interface.

Genetic algorithm optimizers are robust, stochastic search methods, modeled on the principles and concepts of the natural selection and evolution [32]. The flowchart of the proposed genetic algorithm is depicted in Figure 3-4. The EBG's patch size w and the gap g were selected as state variables. The relative permittivity ϵ_r ,and the height h of the dielectric substrate alongside the via's radius r are considered to be constant and equal to 10.2, 1.27 mm and 0.5 mm, respectively. The required

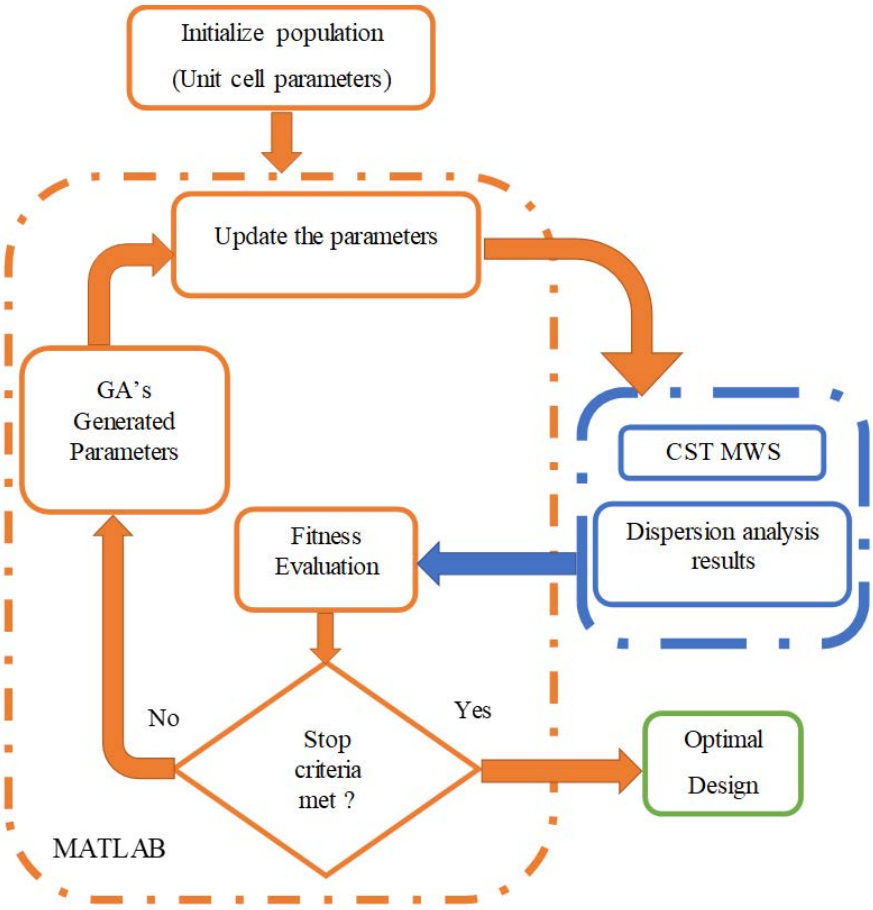

Figure 3-4: The flowchart for genetic algorithm parameters optimization.

center frequency of the bandgap is f_c=5.8 GHz, and the objective is formulated as a two-criterion function with respect to both the bandgap position and the maximum bandwidth, the fitness function is minimized and defined as:

$$Fit = \left(\frac{f_{B\_\max} + f_{B\_\min}}{2} - f_c \right)^2 - \left(\frac{f_{B\_\max} - f_{B\_\min}}{f_c} \right) \tag{3.5}$$

Where $f_{B\_\max}$ and $f_{B\_\min}$ are the upper and lower limit of the bandgap. The minimum and the maximum value of the patch size w are set to 3 mm and 6 mm, respectively, the gap g is defined within the range of [0.2-0.8] mm. The initial population consists of 30 random individuals, going through the process of selection (Roulette), the probability of the crossover is 100 % and the probability of the mutation is set to 1 %, and the number of generations is set to be 20.

After reaching the maximum number of iterations, the final optimized parameters for our designing scenario are given as follow:

w = 4.81 mm, g = 0.5 mm, h =h_1 = 1.27 mm, r = 0.5 mm, and the dispersion diagram for the best optimized individual is depicted in Figure 3-5. The first mode is a TM and starts at zero frequency, and the second one is a TE mode and appears at frequency higher than 6.52 GHz. It is clear that no eigen-mode exists in the frequency range from 5.3 GHz to 6.52 GHz (see Figure 3-5), A band-gap region it is, where no surface wave is allowed to propagate. This stop-band extends from the top of the TM band to the point where the TE band and the light line are crossed. This band-gap is due to the existence of the vias, where the wave attempts to move downward into the dielectric substrate when the frequency increases, and the more it interacts with the vias, the more it is slowed down till surface wave propagation is suppressed [8].

For correct EBG design, it is essential to distinguish between reflection- and dispersion response of a structure. As described in many papers, the frequency of zero reflection phase (usually calculated for normal wave incidence) does not necessarily lie inside the surface wave band gap [54, 55]. To validate our design's band-gap response, direct transmission method is utilized [52]. Figure 3-6 shows the simulation model of this method, it is found that using four unit cells is enough

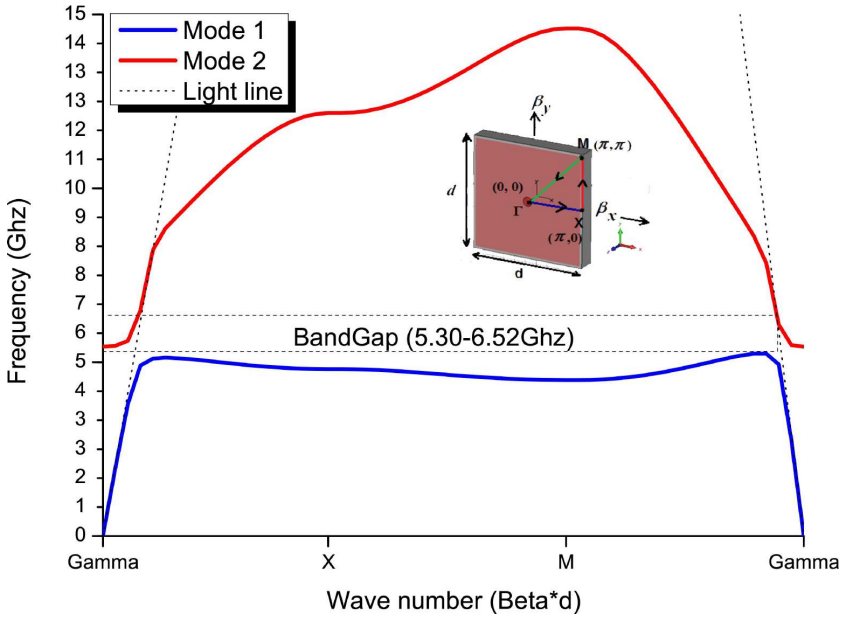

Figure 3-5: Dispersion diagram of the optimized EBG unit cell. The vertical axis shows the frequency and the horizontal axis represents the values of the transverse wavenumbers (βx, βy). Three specific points are: Γ, X and M.

to exhibit a band-gap (Figure 3-7) between the frequencies of 5-6.57 GHz with the criteria of -20 dB, in which the electromagnetic wave cannot propagate.

However, a 4.81 mm unit cell for a structure of four rows increases the substrate dimensions (58 mm x 58 mm) and this is an inconvenience in designing a compact MPA.

A size reducing technique is necessary to resolve such a problem. In [56] a simple way to reduce the size of a mushroom-type EBG surface is proposed, by changing

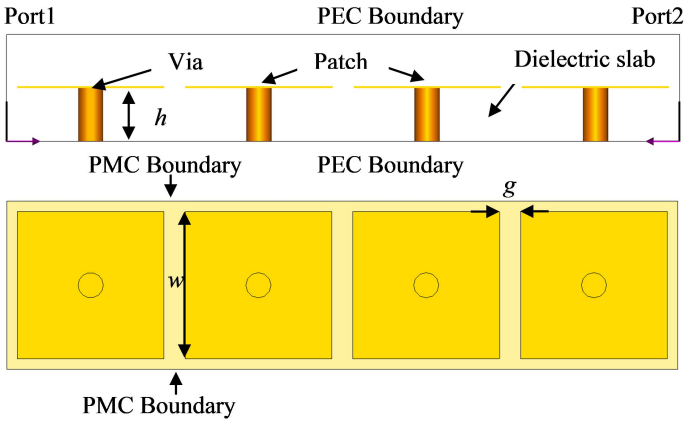

Figure 3-6: Simulation model of the direct transmission method.

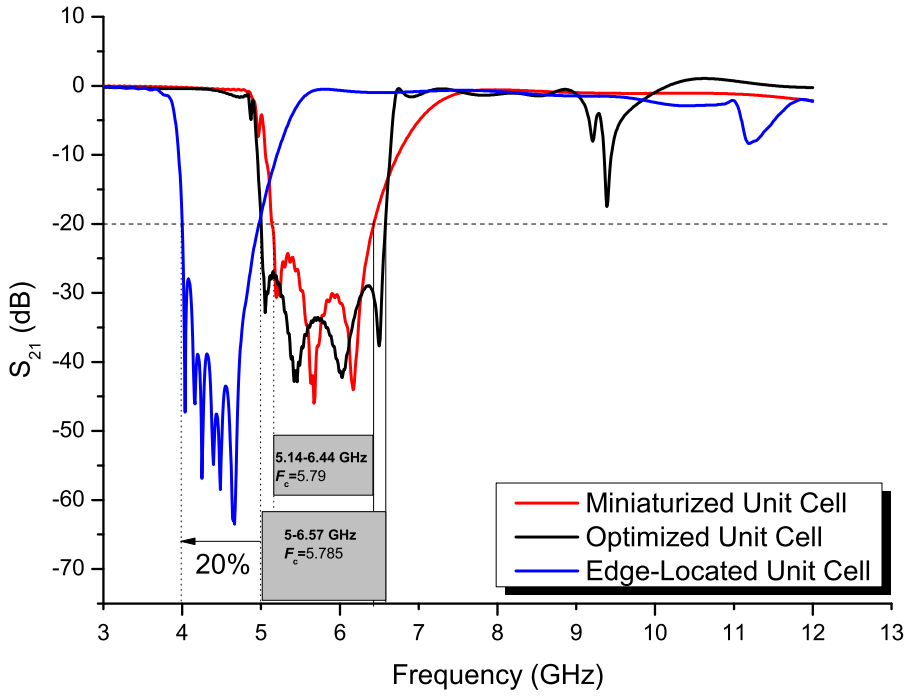

Figure 3-7: S_{21} transmission coefficient of the EBG structure.

the via's position from the center to the side. This allows a 20 % reduction in the start frequency of the band-gap that has been verified via direct transmission line method (see Figure 3-7). Hence reduction in the unit cell size by a factor of 27 % after optimizing the via's radius from 0.5 mm to 0.3 mm is achieved, and the new parameters for the optimized EBG unit cell are:

w = 3.5 mm, g = 0.5 mm, h =h_1 = 1.27 mm,r = 0.3 mm.

These parameters were enough to cover a bandgap from 5.14 to 6.44 GHz (Figure 3-7) to ensure the surface wave suppression around the resonance frequency of 5.8 GHz. It is clearly observed that, our design's stop-band is characterized successfully, using both analyzing techniques. The overall size of the EBG structure is the same as the step-like antenna, which is 1λ x 1λ (where λ is the free space wavelength at the resonance frequency), and by using the final miniaturized EBG unit cell, the proposed EBG structure is composed of a 13 x 13 unit cell array, and by removing the 49 unit cells covering the upper substrate, leaving the final EBG structure with only 120 unit cells, instead of 169.

Different configurations were performed and analyzed by changing the position of the edge-located vias, and the best configuration is depicted in Figure 3-8.

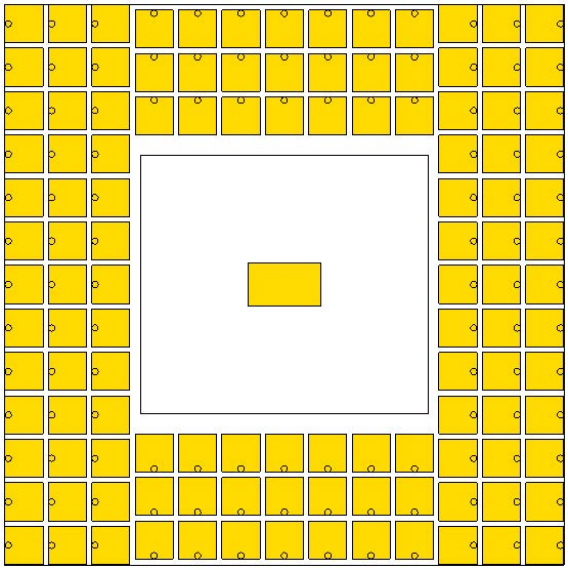

Figure 3-8: Best configuration of the edged-located vias.

The mushroom EBG can suppress surface waves if and only if the following rules are kept:

- The antenna (exciting surface waves of both polarization) works under the first substrate TE surface wave cutoff frequency (i.e. the substrate guides TM0 mode only).
- A mushroom-type EBG is used.

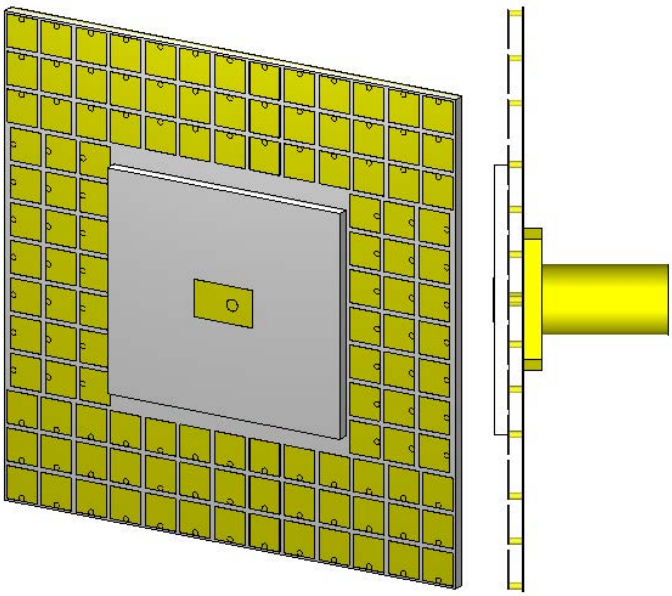

Figure 3-9: The proposed Step-Like EBG (S-EBG) structure.

For our proposed design, both conditions are met, since the cutoff frequency for the first TE1 surface mode is $f_c = 19.5$ GHz and was calculated using the following formula [57]:

$$f_c = \frac{c}{4h\sqrt{\varepsilon_r - 1}} \tag{3.6}$$

Which is larger than the operating frequency, so the conditions are met and verified.

Figure 3-9 depicts the final optimized EBG design and the simulation results are discussed in the next section.

3.3 Numerical results and discussion

In the previous section, four antenna designs were simulated and investigated and the simulation results are given in this section. Figure 3-10 compares the simulated S_{11} results of the proposed S-EBG and the other three antennas. The thin substrate design has a return loss of -22 dB and impedance bandwidth of 66 MHz (1.14 %), where as in the case of the thick substrate antenna, the return loss was -21 dB with 186 MHz (3.22 %) for a bandwidth. Both the Step-Like design and the proposed EBG structure have shown an improvement in return loss with a -34 and -42 dB respectively, and despite the fact that the thickness of the substrate under the patch is the main factor in determining the bandwidth of the antenna and the

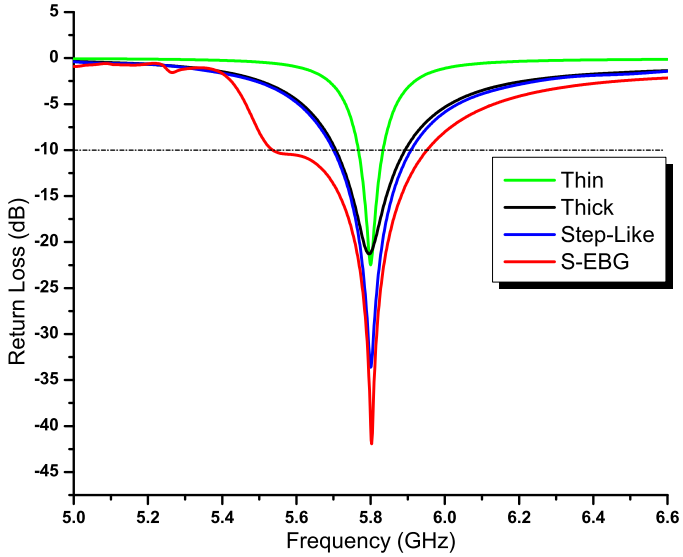

Figure 3-10: Simulated return loss versus frequency.

S-EBG structure being located away from the patch, this later shows an important improvement in bandwidth, around 417 MHz (7.20 %) in contrary to the step-like substrate being also located away from the patch antenna, but having less effect on the antenna's bandwidth (+0.42 % in comparing to the thick substrate).

For a further understanding of the antenna's performance, the radiation properties of the antennas were investigated and simulated around the operating frequency of 5.8 GHz, directivity patterns are shown in Figure 3-11 and Figure 3-12.

Figure 3-11 illustrates the radiation patterns of these antennas (polar plot), both in the E-plane and in H-plane. The antenna on the thick substrate has the lowest front radiation while its back radiation is the largest. Both the antenna on the thin substrate and the step-like structure exhibits similar radiation performance with a slight difference in the favor of the thin substrate antenna. The best radiation performance is achieved by the S-EBG antenna structure. Because of the successful suppression of surface waves, its front radiation is the highest, which is about 2.85 dBi higher than the thick substrate antenna. Since the surface wave diffraction at the edges of the ground plane is suppressed due to the presence of the band-gap, the EBG antenna has a very low back lobe, which is more than 4 dB lower than other cases.

It is also interesting to notice that beam width of the S-EBG structure is much narrower (see Figure 3-12) than the other three cases in both E- and H-planes.

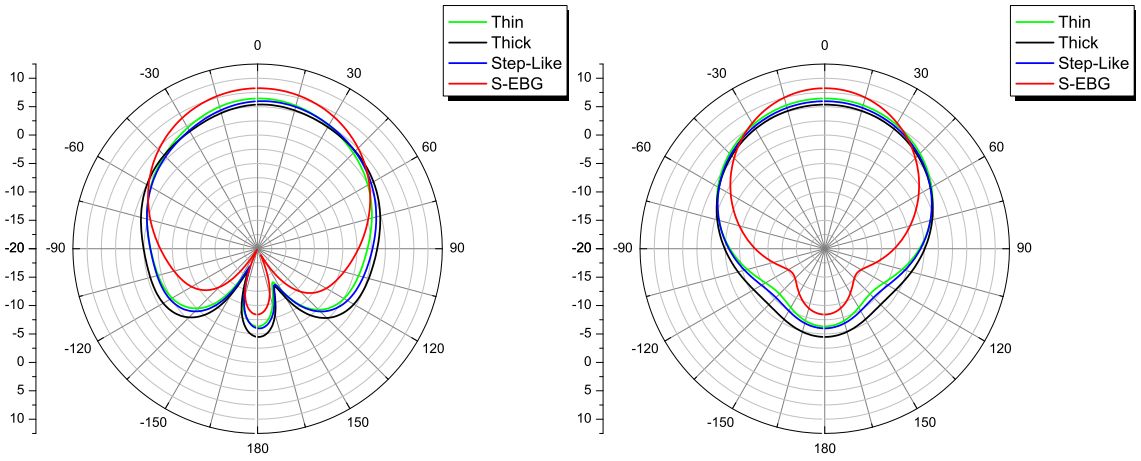

(a) (b)

Figure 3-11: Simulated radiation patterns, (a) H-plane, (b) E-plane (Polar plot).

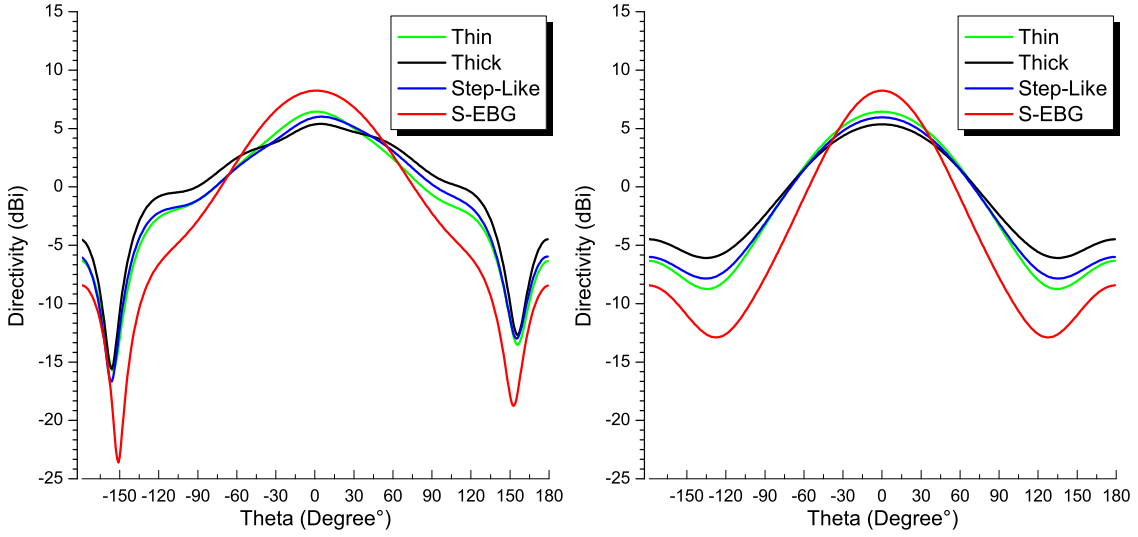

Figure 3-12: Simulated radiation patterns, (a) H-plane, (b) E-plane (Cartesian plot).

Because the EBG structure stops the surface wave propagation, so the beam becomes much narrower. From above comparisons, it is clear that the EBG structure improves the radiation performances of the patch antenna.

3.4 Fabrication & Measurements Results

In this section, the simulation results are validated by first fabricating all involving parts of the proposed design with its final optimized geometry and dimensions, on the Rogers RT/ duroid 6010LM dielectric slab with thickness of 2.54 mm (1.27 mm for each layer). They were assembled using adhesive paste, to form the final proposed prototype (see Figure 3-13(a)). It is fed by a 50 Ohm SMA connector soldered directly to the patch.

Next, the reflection coefficients characteristics of the fabricated prototype are analyzed and measured using the Agilent 8722ES Vector Network Analyzer (VNA), and the results are illustrated in Figure 3-14, where the measured impedance bandwidth with S11 <-10 dB criterion is 438 MHz ranging from 5.644 to 6.082 GHz, corresponding to a fractional impedance bandwidth of 7.47% with respect to the center frequency of interest. It is also compared to the simulated results, where the impedance bandwidth was 7.20% (417 MHz). Therefore, both simulation and

(a)

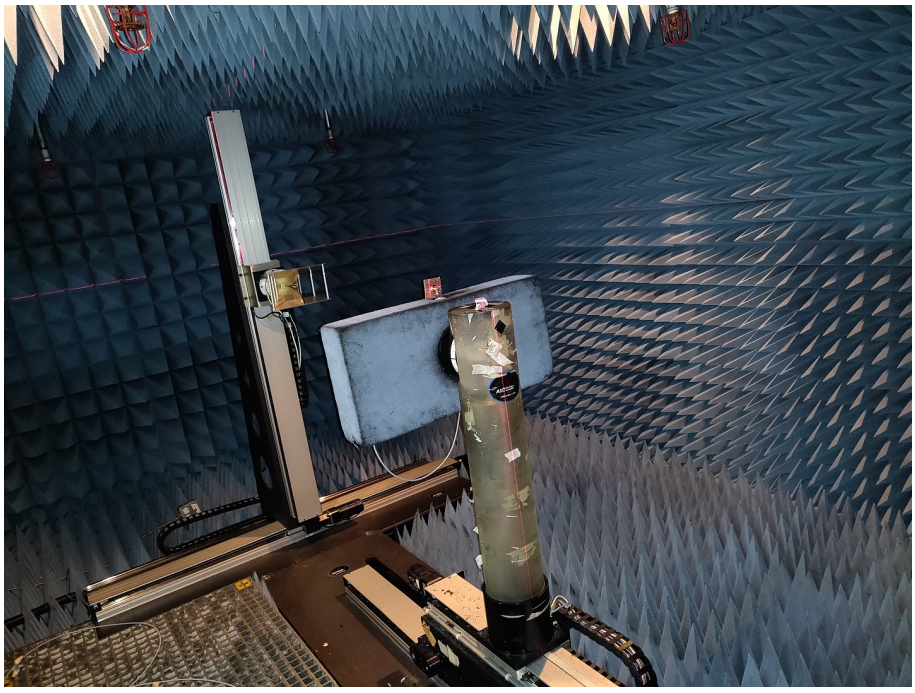

(b)

Figure 3-13: The final (a) fabricated antenna and its assembly parts, and (b) far-field measurement setup.

measurement results are in good agreement, despite the slight discrepancies between them, which are probably due to assembly and fabrication errors.

In addition, the radiation patterns for the proposed prototype were measured in an anechoic chamber, and the setup is depicted in Figure 3-13 (b). The normalized simulated and measured radiation patterns of the proposed antenna are illustrated in Figure 3-15 at the center frequency of 5.8 GHz, in both H- and E-planes.

The obtained radiation patterns (simulated and measured) of the antenna, are directional in the broadside of both the E- and H-planes, with lower sidelobe levels. Both simulation and measurements results are in good agreement, with a slight

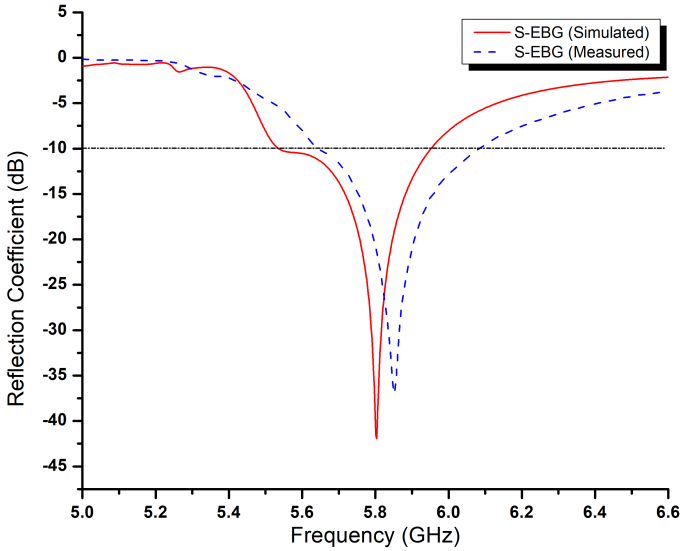

Figure 3-14: Simulated and measured reflection coefficients versus frequency.

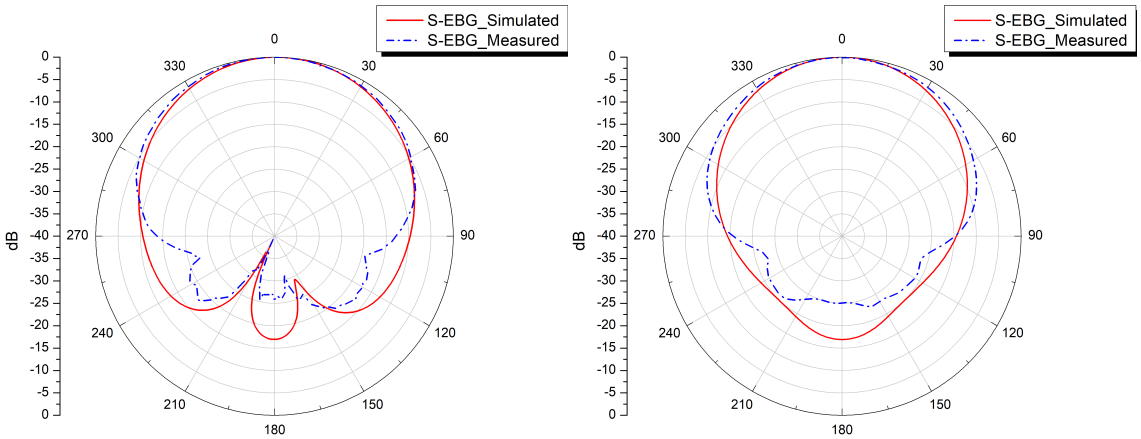

Figure 3-15: Normalized simulated and measured radiation patterns, (a) E-plane, (b) H-plane at 5.8 GHz

difference due to fabrication errors.

For easier comparison between the antennas, the most relevant parameters are summarized in Table 3.1, the performances of the proposed antenna and other related works were illustrated in Table 3.2, where It can be observed that, the proposed antenna outperforms the other designs in terms of return loss and peak gain with an adequate bandwidth while maintaining its compact size on thick and high dielectric permittivity substrate.

Table 3.1: Simulated antenna's performance of all antenna designs

Ant.	Thin	Thick	Step-Like	S-EBG
Return loss (dB)	-22	-21	-34	-42
Bandwidth (%)	1.14	3.22	3.64	7.20
Front Radia.(dBi)	6.44	5.39	6.01	8.24
Back Radia. (dB)	-12.8	-9.9	-12	-16.7
Peak gain (dB)	5.66	5.13	5.71	8

Table 3.2: Proposed antenna versus other related works

Ant.	[58]	[59]	[60]	[61]	This work
Freq. (GHz)	5.674	5.8	6	5.8	5.8
S_{11} (dB)	-22	-14.8	-20	-32	-42
BW (%)	3.59	4.13	2.51	6.89	7.20
Gain (dB)	6.7	1.6	5.9	6.4	8
Size (mm)					
w	17.68	24	15.72	13.6	6.7
l	13.85	16	11.74	10	4
h	0.762	1.6	1.58	2.54	2.54

3.5 Summary

In this chapter, a mushroom-like EBG-Based structure was investigated and simulated alongside three other designs on a high dielectric permittivity substrate to take advantage of using such dielectric medium, in terms of compactness of the patch, and to enhance the overall performance.

The EBG unit cell parameters were calculated and optimized using the combination of a stochastic global optimization algorithm (GA) and the commercial simulator CST Microwave studio, to insure the coverage of the resonance frequency of 5.8 GHz.

A parametric study was conducted on the EBG cell by varying the position of the via, to lower the frequency of the band-gap, hence reducing the unit's size to prevent an increase in overall size of the antenna, the bandgap was determined using the dispersion diagram method and verified with the direct transmission technique.

The obtained simulation and measurement results show a good overall performance in terms of return loss, bandwidth, directivity and peak gain, comparing it

to the thick substrate case with an improvement of 50 % in return loss, 55 % in impedance bandwidth, 34 % and 35 % for directivity (front radiation) and peak gain respectively, due to the successful suppression of the surface waves by implementing (EBG) structure, which makes the proposed design an extremely attractive and ideal choice for RFID and wireless communication (WLAN, WiMAX, etc...) applications.

Chapter 4

Analysis and Design of An UWB Antenna Using A Compact Topology Optimized Single FSS-Layer as A Reflector

4.1 Introduction

Microstrip patch antennas play a vital role in today's wireless communication systems, as mentioned in the previous chapter. They are widely used because of their special traits, such as low in profile and cost, light weighted, compact, and easy to fabricate, and have the integration ability with solid-state devices [62]. In spite of these remarkable advantages, microstrip patch antennas suffer from narrow bandwidth and low gain.

With the increasing demand for high data rates, broadband and multi-band antennas are attracting subjects in both academic and industrial sectors. Since the Federal Communications Commission FCC released the 3.1 to 10.6 GHz unlicensed band for communication [63], and the fast development of broadband antenna designs, wideband antennas with better gain performances have become the talking point of many researchers, and have extensively been used in various wireless com-

munication systems, for their simplicity, broader bandwidth, low profile, and low cost effective performances, easy fabrication, which made them to be an attractive candidates for many applications [64, 65] [66]. However, such configurations have a major disadvantage in terms of low-gain performance, and exhibit gain fluctuations over their wide range of frequencies.

To tackle this problem, Electromagnetic Band Gap EBG structures and Artificial Magnetic Conductors AMC, have been used to improve the gain characteristics of such structures. These later are mostly used as reflectors, placed very near to the radiating element, reflecting the incident signal, which in turn leads to a cumulative superposition of radiation from the antennas [67, 68]. Consequently, a gain enhancement could be achieved.

In [69], the authors have used an Artificial Magnetic Conductor AMC as a reflector, as well as in the case of [70], where an electromagnetic band gap EBG has also been applied as a reflector. Both suppressed the surface waves at the operating frequency, which leads to an increase in gain. The proposed unit cells are not only large in size, but also provide only a narrow bandwidth and a nonlinear phase reflection coefficient. Authors of [71] have used the Uniplanar Compact Photonic Band gap UC-PBG as a lens for gain enhancement, while [72, 73] used a frequency selective surface FSS based on aperture and superstrate to enhance both directivity and gain. In [74] and [75], authors have used multilayer FSSs to generate a multi-stop-band structure with a wide band property to enhance the gain but at the same time it increases both design profile and complexity.

A convoluted circular FSS unit cell, alongside an interwoven with a convoluted element from a simple spiral dipole array, have been proposed by authors of [76] and [77] to achieve the desired miniaturization aspect of an FSS array. Therefore, the main objective of this study is to design a broadband, compact-size, and low-profile FSS structure in order to achieve ultra-wide band properties and high gain.

In this chapter, a compact ultra-wideband FSS structure is proposed to operate at the UWB spectrum, and acts as a reflector to an ultra-wideband monopole antenna to improve its gain. The binary genetic algorithm is exploited using the automated topology synthesizing system, based on the interface established between

MATLAB and CST Microwave Studio through VBA language, to achieve the objective of a miniaturized and yet ultra-wideband FSS unit cell.

4.2 Design procedure and structure analysis

In this section, all antenna design variations, use the Rogers RO4350B substrate material having thickness (h_s) of 1.524 mm, and permittivity ϵ_r= 3.66, alongside the FSS unit cell design, and simulated using full wave CST Microwave Studio.

4.2.1 Antenna Design variations

Our proposed ultra-wideband antenna is achieved after a series of modifications and variations in the design, mainly to expand its bandwidth. First, the initial design of a conventional microstrip fed patch antenna (MPA) is achieved by using the equations of the transmission line model as a guideline. According to [19], the following equations ((1)-(5)) are used to design this antenna by calculating the geometrical parameters, namely the patch width W_p and the patch length L_p, assuming that the resonant frequency f_r, the relative permittivity ϵ_r and the substrate's height h_s are known, and these equations are outlined as follows: First, we calculate the patch width W_p using equation (1):

$$W_p = \frac{c}{2f_r}\sqrt{\frac{2}{\varepsilon_r + 1}} \tag{4.1}$$

where c is speed of light in free space. Then with this parameter, the substrate's effective permittivity (ϵ_{eff}) is calculated using (2):

$$\varepsilon_{eff} = \frac{\varepsilon_r + 1}{2} + \frac{\varepsilon_r - 1}{2}\left(\frac{1}{\sqrt{1 + 12h_s/W_p}}\right) \tag{4.2}$$

Using this later (ϵ_{eff}), we calculate the patch length extension ΔL_p (3):

$$\Delta L_p = 0.412\ h_s \frac{(\varepsilon_{eff} + 0.3)}{(\varepsilon_{eff} - 0.258)} \frac{\left(\frac{W_p}{h_s} + 0.262\right)}{\left(\frac{W_p}{h_s} + 0.813\right)} \tag{4.3}$$

Finally, L_p is calculated using the following equations (4) and (5)

$$L_{eff} = \frac{c}{2f_r\sqrt{\varepsilon_{eff}}} \tag{4.4}$$

$$L_{p=L_{eff}-2\Delta L_p} \tag{4.5}$$

First, we begin by designing a simple microstrip-fed patch antenna (C-MPA) as a first step towards our final proposed design; operating at 5.8 GHz using the previously stated equations. The Rogers RO4350B dielectric slab is chosen as a base substrate with a dielectric constant ϵ_r= 3.66, and a height of h_s = 1.524mm. Knowing these parameters, both the width and length of the patch are calculated as W_p =18.29 mm and L_p=14.24 mm. By tuning these parameters using CST Microwave studio, the final optimized values are obtained and summarized in Table 4.1.

From the obtained return loss S_{11} of this antenna, the resonance frequency is 5.8 GHz, and the -10 dB impedance bandwidth is 175 MHz (0.175GHz) ranging from 5.71 to 5.88 GHz, and a fractional bandwidth (FBW) of 3.01%. Next, our objective is to broaden the antenna bandwidth without increasing its size profile. To do so, we redesign the previous MPA by using a curved partial ground (PG -MPA) with length lg, while keeping the other geometrical parameters fixed. Using a partial ground and sweeping the parameter lg, the bandwidth is broadened to 3.5 GHz, which leads to an improvement by a factor of 20, in comparison to the initial design, covering the band from 3.1-6.6 GHz, and an FBW of 60% at the center frequency of 5.8 GHz.

Even with this enhancement, this design does not cover the whole ultra-wide band frequencies of interest (3.1-10.6 GHz), and to further enlarge the bandwidth, our next approach is based on using a pixelated based pattern on the patch antenna, just like slots, to create multiple resonances, for increasing the bandwidth. Genetic algorithm (GA) based optimizations are carried out, to which yields to great potential in finding no-conventional solutions to EM-based problems. In [78], the authors have used GA to miniaturize the patch antenna by a rate of 82%. Where as in the case of [79], the authors use the same technique to achieve a wide band microstrip patch antenna.

Table 4.1: Conventional MPA geometrical parameters

Parameter	Value (mm)	Parameter	Value (mm)
Substrate width (Ws)	30	Patch length (Lp)	14.38
Substrate length (Ls)	30	Feed Length (Lf)	8
Substrate height (hs)	1.524	Feed Width (Wf)	3.1
Patch width (Wp)	17.85	Copper Thickness(mt)	0.018

A Genetic algorithm (GA) is used here, in parallel with MATLAB through a well-established VBA based connection, hence an automated synthesizing system to create these patterns. The patch area is the targeted element on this procedure, it is divided into n x m cells matrix composed of both conducting and non-conducting cells, and is defined using binary encoding, meaning if a cell is conducting, then the assigned binary bit is 1, and if a cell is non-conducting one, it is assigned 0.

In our scenario, the GA operates on a 50-bit encoded binary string (10 by 5 pixelated binary array), and this string of binary bits represents a chromosome, and this later will undergo many operations and steps to reach the optimal solution or an individual in a search space of 250. The 10 x 5 pixelated array is mirrored along the y axis to form a symmetrical 10 x 10 array, representing the whole patch area, so by using the mirroring technique, the calculation and search is cut down by half, and the 10 x 5 array is the only trial solution (see Figure 4-1).

First, a population of a randomly generated solutions is created, and then passed on to the next GA based operations, such as selection, crossover, and mutation. The

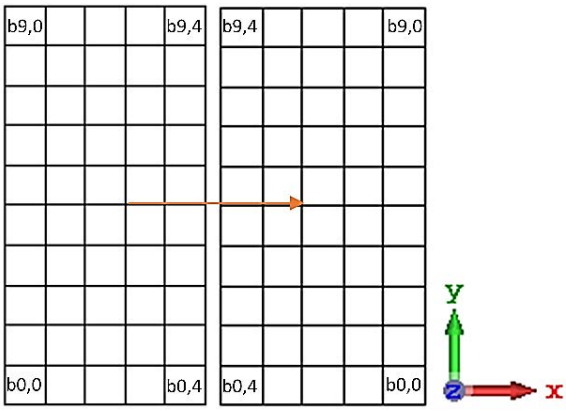

Figure 4-1: A 10 x 5 array mirrored along the y axis to create a 10 x 10 symmetrical array (Patch).

next generations of these solutions are selected according to their performances of the previously solutions (antenna instances), using a fitness or a cost function. The optimization process of our design is summarized and illustrated in Figure 4-2.

After the geometry is generated, the performance is evaluated by the Time-Domain solver embedded in CST Microwave Studio, and the S-parameter is then returned to MATLAB through VBA link, to compute the fitness function according to each generated and simulated antenna. For this optimization process, a return loss-based fitness function is used. It is defined as the sum of all values that exceed -10 dB, to achieve the maximum bandwidth between 3.1–10.6 GHz (UWB spectrum). The fitness function is then defined as follows:

$$Fitness = -\sum_{f_1}^{f_2} L\left(f_i\right) \tag{4.6}$$

where

$$L\left(f_i\right) = \begin{cases} S_{11}\left(f_i\right) dB & S_{11}\left(f_i\right) dB \geq -10dB \\ -10dB & S_{11}\left(f_i\right) dB < -10dB \end{cases} \tag{4.7}$$

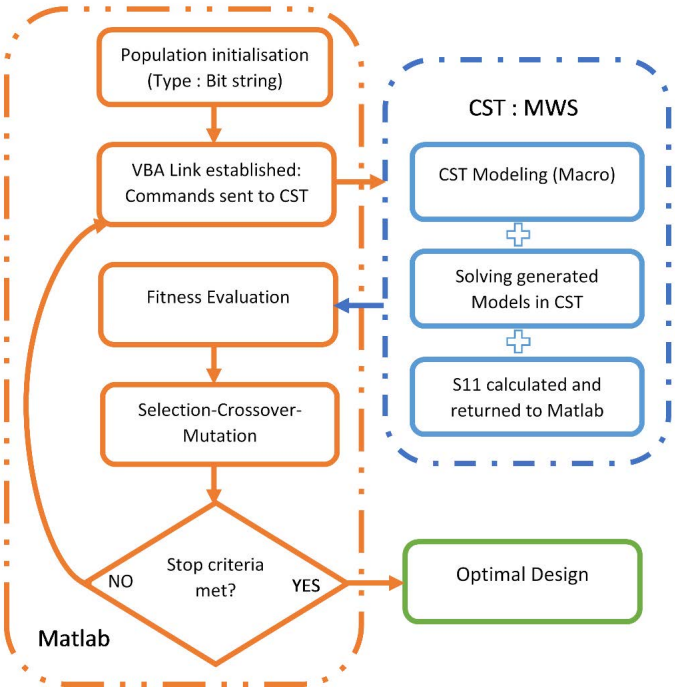

Figure 4-2: The Proposed flowchart of the GA optimization process for UWB antenna.

The population size is set to 200 and evolved over 20 generations. A single run of CST Microwave Studio on one trial solution antenna takes approximately 1.5 min on an Intel i7 2.2 GHz PC. For the given population size and generations, 4000 such runs are necessary. This adds up to 4 days runtime on a single machine, but fortunately the stopping criteria is met at the 10th generation, and the final design's binary representation is illustrated in Figure 4-3.

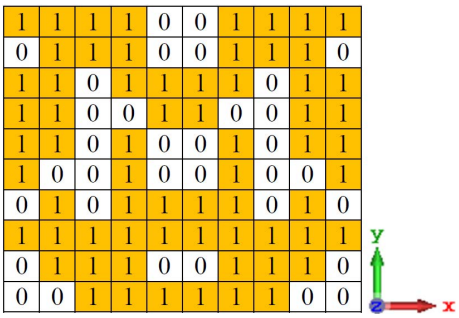

Figure 4-3: The optimal design's binary representation.

However, this design suffers from an infinitesimal connection problem, between two sub-patches, when these constellations $\left(\begin{smallmatrix}1&0\\0&1\end{smallmatrix}\right)$ or $\left(\begin{smallmatrix}0&1\\1&0\end{smallmatrix}\right)$ are present, which leads to a malfunctioning patch antenna, due to fabrication tolerances [79]. To overcome this inconvenience, the adjacent sub-patches are then overlapped to ensure the electrical contact, while keeping in mind the effect of this overlapping area on the overall structure, so it must be chosen so it doesn't influence on its electromagnetic properties, hence a minimum value for the overlapping area is a must, and this value is limited of course by the machine precision, during the fabrication process. The overlapping offset is set to be $O_l = 0.2$ mm. The final GA optimized and ready for fabrication design, is illustrated in Figure 4-5 (c).

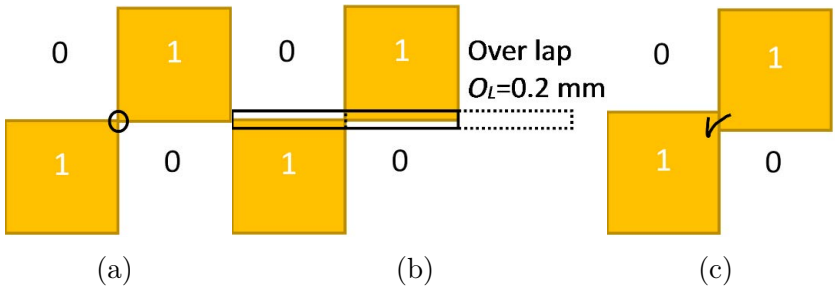

Figure 4-4: (a) Combination with infinitesimal connection. (b) Proposed overlapping scheme. (c) A good connection with overlapping area.

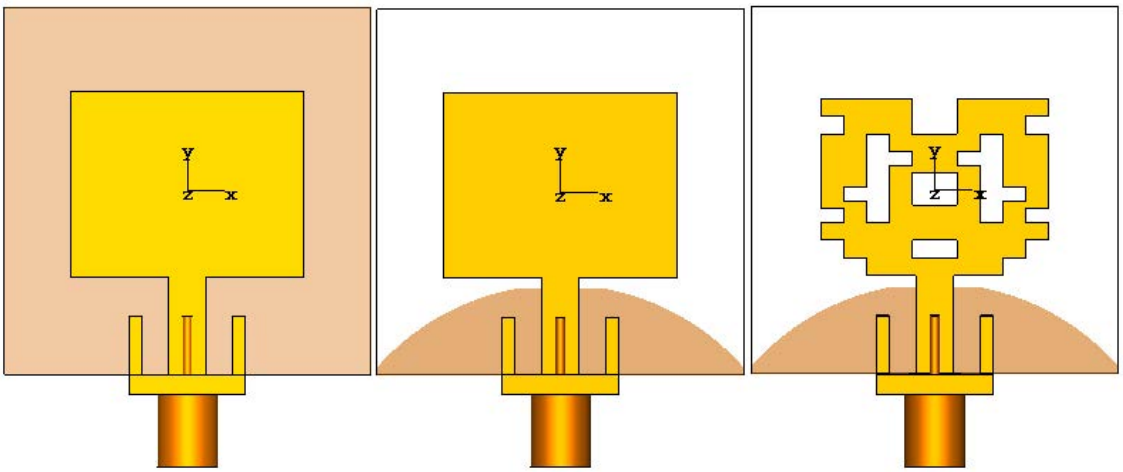

(a) (b) (c)

Figure 4-5: Schematic of the (a) C-MPA design, (b) PG -MPA , and (c) the final GA-MPA design.

Figure 4-6. illustrates the obtained return loss S_{11} of the final optimized design, with -10 dB impedance bandwidth of 10.4 GHz ranging from 3.1 to 13.5 GHz, and a fractional bandwidth (FBW) of 179.31% at the resonance frequency of 5.8 GHz. So, the proposed design achieved the required bandwidth (3.1-10.6 GHz) while keeping its compact size and low profile.

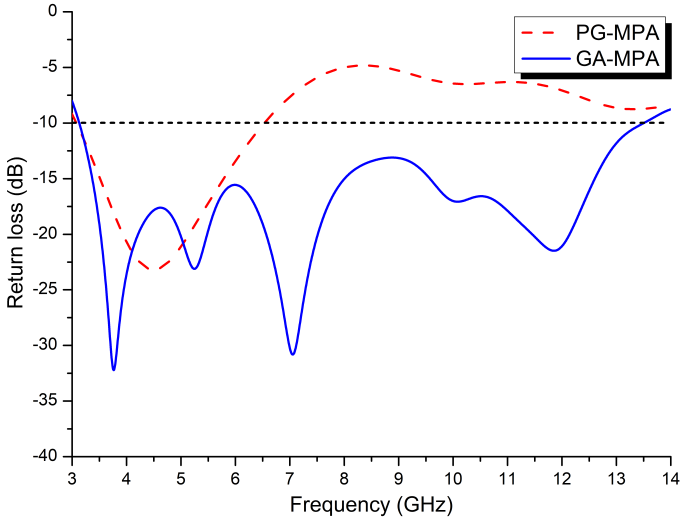

Figure 4-6: Simulated return loss of the final GA-Based MPA versus the Partial-Ground MPA .

4.2.2 FSS unit cell designing process

The Proposed FSS unit cell, is also designed on the RO4350b substrate, with a thickness (h_{FSS}) of 1.524 mm, and permittivity of $\epsilon_r = 3.66$, and is achieved by the following designing steps and variations.

The first step, a simple square-loop patch is printed on the top of the substrate, with L_{FSS} and W_{FSS} as length and width, respectively, taking into account the spacing S=2*g between two FSS unit cells (see Figure 4-7(a)).

Figure 4-7(b) depicts the simulation and analysis setup in CST microwave studio of the FSS unit cell, where boundary conditions are applied as follow: along the ± x-axis, the perfect magnetic condition (PMC) is applied, whereas in the case of the ±y-axis, the perfect electric boundary condition (PEC) is used, with two wave ports along the z-axis with open boundary condition, so only the normal incidence is considered here.

The length of the square loop is taken as L_{FSS}=10.8 mm, and its width as W_{FSS}= 0.9 mm, and S is varied from 0.2 to 1.2 mm, to see the effect of this latter on the unit cell transmission coefficient response. From Figure 4-8, it is clearly noticed that when the spacing S is increased, the FSS cell response is shifted towards the higher frequency band, due to the lower capacitance between two FSS unit cells, and the overall size of the unit cell, is also increased (from 11 mm to 12 mm). So, the smaller

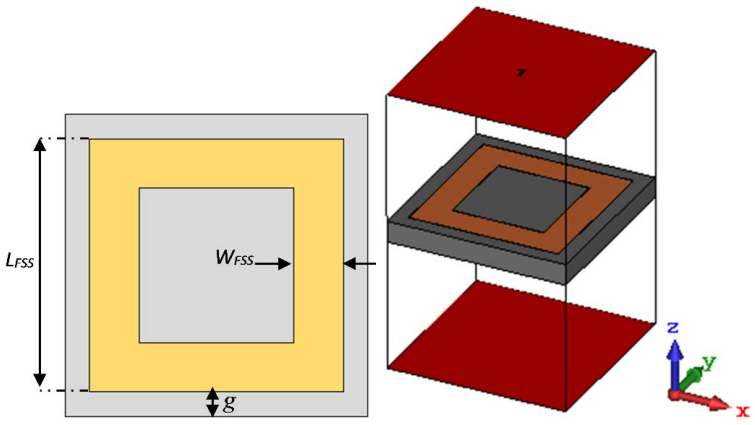

(a) (b)

Figure 4-7: (a) Geometry of the initial FSS unit cell, (b) Analysis setup of the unit cell (CST).

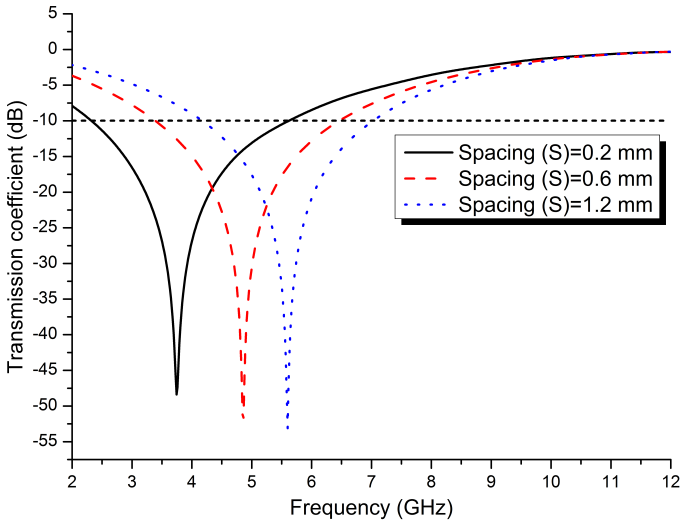

Figure 4-8: Variation of the transmission coefficient of the initial FSS unit cell for different spacing S.

the spacing S is, the better, because it leads to a higher capacitance value, meaning the lower band is covered [80], and the overall size of the FSS unit cell is kept as compact as possible.

Increasing the length L_{FSS} would shift the frequencies towards the lower end, but at the expense of the unit cell size. This unit cell is far from achieving the UWB requirements, as the largest -10 dB bandwidth attained by this simple design is 3.3 GHz, for S= 0.2 mm.

To overcome this, the same bandwidth enhancement technique is used in the proposed UWB antenna, is also used here, to cover the full UWB spectrum while keeping a degree of compactness.

The previously established link between CST and MATLAB, is also used here with some modifications in terms of the targeted structure and the fitness function.

The FSS unit cell is divided into square pixel cells, each can be a conducting or non-conducting cell, and is represented by the binary bits 1 and 0, respectively.

When the number of pixel cells is increased, the number of total possible structures is also increased, making it an impractical way to solve such a problem, in which a global optimization solution is needed, with a confined search space for the optimal candidate, according to a predefined fitness criterion, making the genetic algorithm an effective way in doing so. Each binary word generated by the genetic

algorithm, corresponds to a possible candidate model throughout the optimization process, analysed and evaluated using a predefined fitness function, which makes defining this latter a critical part in formulating the optimization problem.

In our designing scenario, the fitness function is defined as the sum of all values that exceed -10 dB of the unit cell transmission coefficient (S_{21}), to achieve a broad band-stop performance between 3.1–10.6 GHz (UWB spectrum), and is defined as:

$$Fit = -\sum_{i=1}^{N} Sn\left(f_i\right) \tag{4.8}$$

where

$$Sn = 20log_{10}\left|S_{21}\left(f_i\right)\right| \tag{4.9}$$

and

$$Sn\left(f_i\right) = \begin{cases} S_n\left(f_i\right) dB & S_n\left(f_i\right) dB \geq -10dB \\ -10dB & S_n\left(f_i\right) dB < -10dB \end{cases} \tag{4.10}$$

The transmission coefficient S_{21} of the FSS unit cell, is taken at equal frequencies fi, with the total number of N =1001 frequency points, between the designated stop-band ($f_{min} \leq f_i \leq f_{max}$), corresponding to the UWB spectrum.

The flowchart of the implemented GA based optimization process for a broad band-stop FSS unit cell, is shown in Figure 4-9.

As a starting point, let us consider the conventional FSS unit cell illustrated in Figure 4-7. as a reference for our optimization process to speed up the search for the optimal design, instead of using a randomly generated binary string as an initial population, which leads to more computational time.

Our goal is to determine a new FSS unit cell topology, to obtain a broad band-stop covering the UWB spectrum. The size of each FSS unit cell is the same as the conventional one (10.8 mm × 10.8 mm), with the same substrate properties.

The FSS unit cell is discretized into 12 × 12 pixels as start, which provides a resolution of 0.9 × 0.9 mm, and is increased accordingly, to see the effect of the number of pixels on the unit cell performance, while taking into account the fabrication constrains, and to maintain the geometrical flexibility.

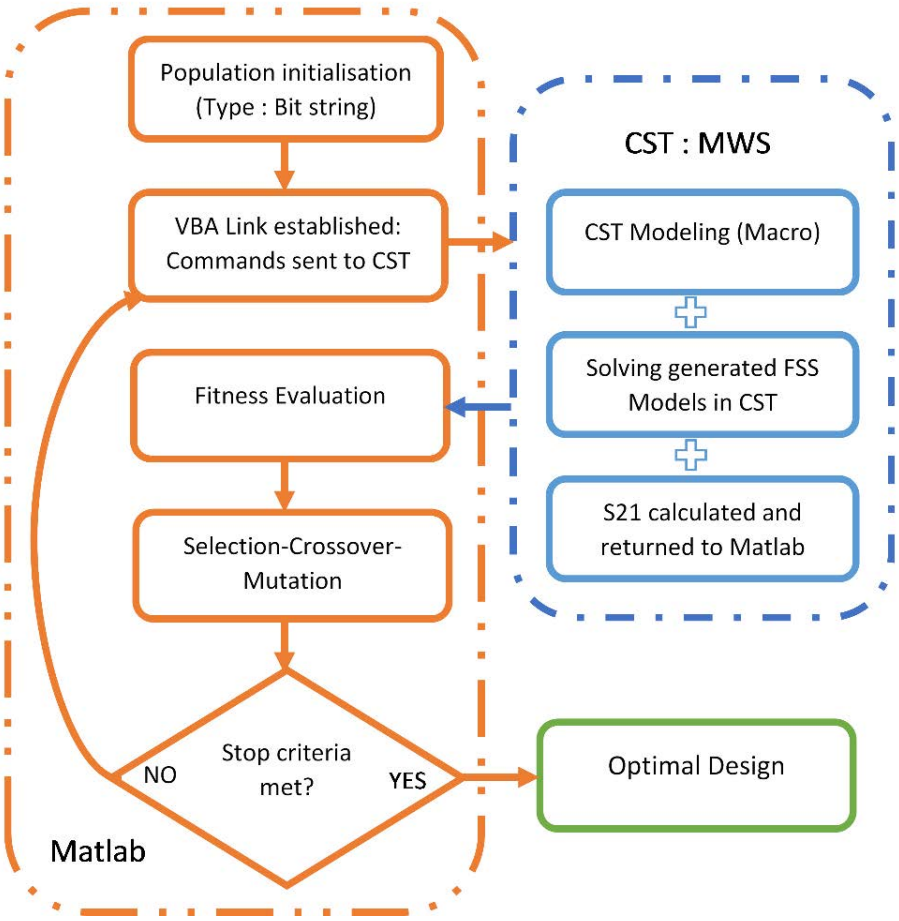

Figure 4-9: The Proposed flowchart of the GA optimization process for the FSS unit cell.

A 12 x 12 discretization space on such unit cell needs to be represented by 144 binary encoded pixels, and this led to a large search space for the optimal solution, an impractical and time-consuming process, that is; however, a four-folded symmetry is imposed on our initial design, as shown in Figure 4-10 providing polarization independence in our design [76]. As a result, the solution search space (the number of bits required to represent the FSS unit cell) is reduced drastically to 21.

For instance, the binary word of the conventional design in Figure 4-10 (a) is represented by:

B_{Conv} = 1 1 1 1 1 1 0 0 0 0 0 0 0 0 0 0 0 0 0 0 0.

The proposed optimization process tries to manipulate the S-curve (transmission coefficient S_{21}) of the possible design candidates, in order to cover the whole

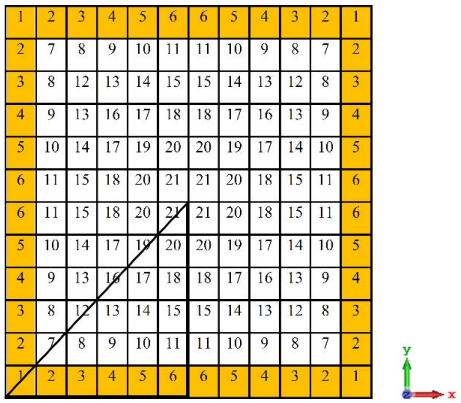

Figure 4-10: The proposed four-folded symmetry pixelated FSS unit cell (12 x12).

UWB spectrum, by using the uniform mutation with a rate of 0.001, single point crossover, and the tournament selection as the genetic algorithm's parameters. The population size is set to be 200 different binary strings randomly selected, with each one representing a specific pixelated FSS unit cell, and 20 is the number of iterations (generations).

Once all the 200 initial pixelated FSS structures are evaluated, they are ranked and the top performing ones are selected for the crossover and mutation process, creating a new population of 200 FSS unit cells going through the same process of evaluation, and this process is repeated until a cost value of -7.5 is obtained (which corresponds to the number of frequency points where the transmission coefficient equals or less than -10 dB , covering the UWB spectrum (3.1-10.6 GHz) or until the maximum number of iterations is reached. The best achieved design (FSS-A) is obtained at the 12th iteration, when the stop criteria is met, as shown in Figure 4-11 (a), the resulted transmission coefficient (S_{21}) ranges from 3 to 12.8 GHz, covering the whole UWB spectrum and some (see Figure 4-12 (a)). The binary string of the final optimized FSS unit cell is:

B_{FSS-A}= 1 1 1 1 1 1 0 0 1 0 0 0 1 1 1 1 0 0 0 0 1.

Keeping the same topology synthesizing setup, and increasing the number of pixels to 14x14, to see the effect on the convergence speed, and the FSS unit cell's performance, two new FSS designs emerged (FSS-B and FSS-C). Both of them converged to the global optimum after the 8th and the 11th iteration, respectively.

FSS-B design, shows an outstanding performance and faster convergence, its

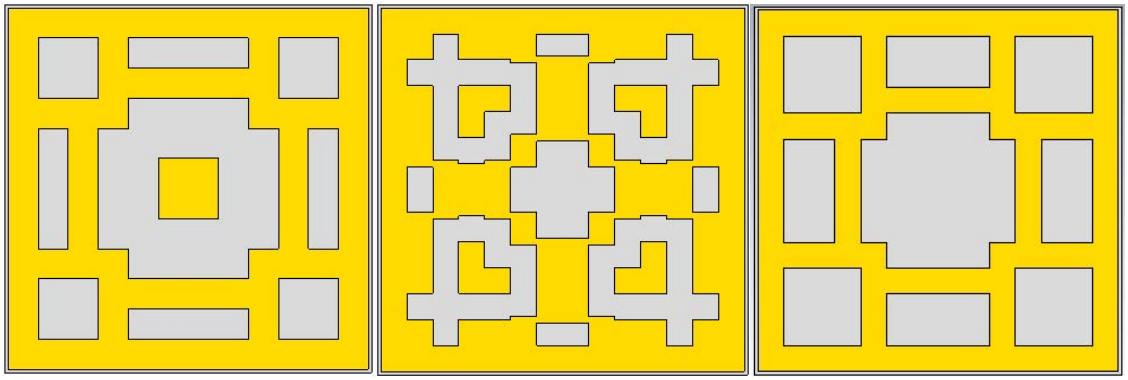

(a) (b) (c)

Figure 4-11: The GA based optimized FSS designs, with (a) 12 x 12 pixels, (b) and (c) 14 x 14 pixelated FSS unit cell.

transmission coefficient exhibited a magnitude below -10 dB, ranging from 2.9 to 14.5 GHz, and so it is more than enough stop-band coverage for the UWB spectrum, whereas for the case of the third design (FSS-C), its transmission coefficient (stop-band), is in the range of 3 to 14.6 GHz, with the lowest S_{21} value of -73.8 dB in comparison to the first design and the second one, where their lowest values are -54 and -58.1 dB, at different center stop frequencies (see Figure 4-12(a)). All proposed designs are achieved with only a 0.1λ x 0.1λ FSS unit cell size, where λ is the wavelength at the lower end frequency. The second and third design's binary words are:

B_{FSS-B}= 1 1 1 1 1 1 1 1 0 1 1 1 0 0 0 0 0 1 1 1 0 1 0 0 1 1 0 0.

B_{FSS-C}= 1 1 1 1 1 1 1 1 0 0 0 1 0 0 0 0 1 0 0 0 1 1 1 1 1 0 0 0 0 0.

Despite its performance, FSS-B suffer from the infinitesimal connections between the diagonal pixelated cells, which leads to inaccurate results from measurements, due to fabrication tolerances. And to get pass this, the same overlapping technique, that is used in our proposed UWB antenna is applied here. The final three FSS designs are depicted in Figure 4-11. The antenna gain can be significantly improved, using these FSS designs as reflector layers, when its reflection coefficient phase is decreasing linearly, with the increment in frequency all over the UWB spectrum (see Figure 4-12(b)). So, when this condition is satisfied, the FSS reflecting layer exhibits a constructive interference with back radiated waves of the UWB antenna.

Design validation was carried out in HFSS (FSS-B), with the same simulation

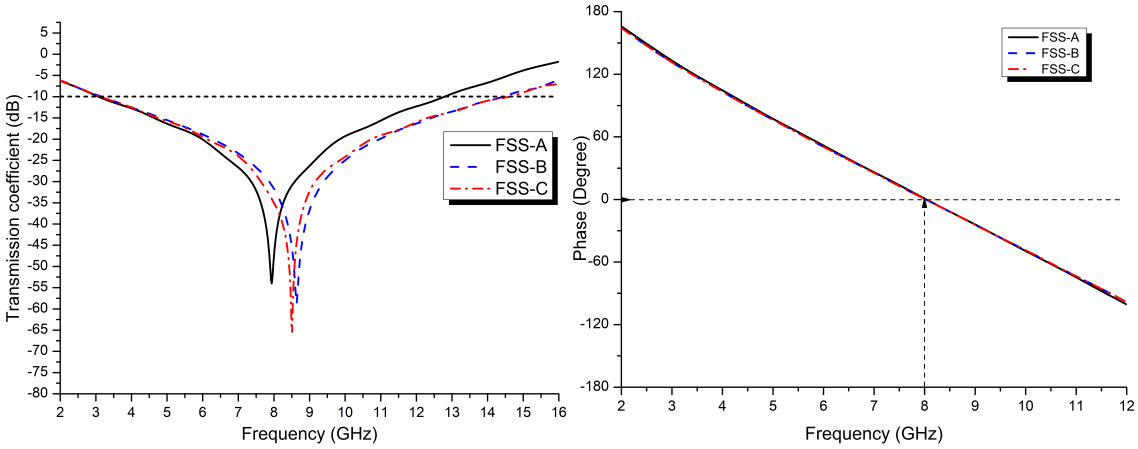

(a) (b)

Figure 4-12: (a) Simulated transmission coefficient (S_{21}) and (b) reflection phase, for all FSS proposed designs.

process in CST, and the results in Figure 4-13, yields a good agreement between them, with a slight shift, due to the different implemented analyzing methods used in both CST and HFSS.

4.3 FSS-backed UWB Antenna

The optimized FSS designs in the previous section are applied as a reflector layer, to improve the performance of the proposed UWB antenna, and it is spaced by a

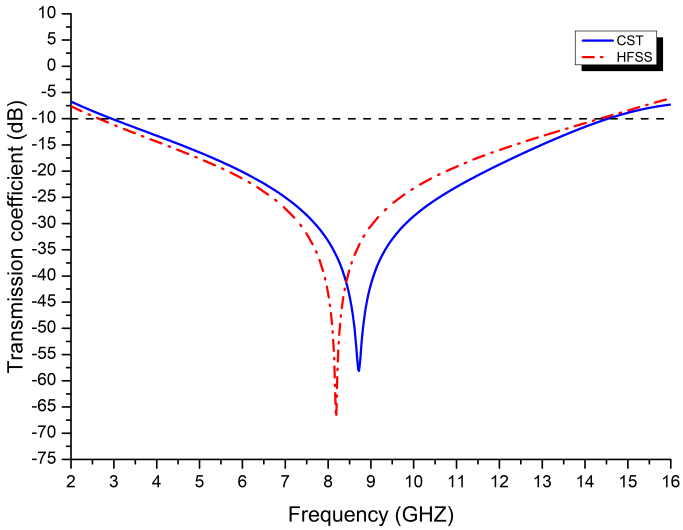

Figure 4-13: Simulated transmission coefficient (S_{21}) of the proposed FSS unit cell (FSS-B) in both CST and HFSS.

distance H_z, and this latter is varied carefully, to find the optimal distance in order to achieve the best performance of FSS-Backed UWB antenna.

The FSS reflecting layer is composed of a 7x7 FSS array, and the proposed FSS-Backed UWB antenna is illustrated in Figure 4-14. When using a single FSS layer reflector concept, with our UWB antenna placed above it at a distance Hz, the reflected wave from the FSS layer is added to the direct radiation from the antenna itself, leading to a constructive interference, when these two waves are in phase, at the reference plane T, and the total phase ϕ_T is described as follow [81]:

$$\phi_T = \phi_S + \phi_R \tag{4.11}$$

where

$$\phi_S = 2\frac{2\pi f}{c}H_z \tag{4.12}$$

ϕ_R is the FSS's reflection phase, and ϕ_S is the path delay phase between the antenna and the FSS reflector. As the phase of path delay is dependent and increased with frequency, the ideal FSS reflection phase response should be decreasing with frequency at the same rate, which is noticed in our proposed FSS designs (see Figure 4-12(b)). The total phase difference ϕ_T should be then equal to zero or an integral multiple of 2 π, in order to fulfill the objective of phase coherence and maximum gain enhancement at all frequencies of interest.

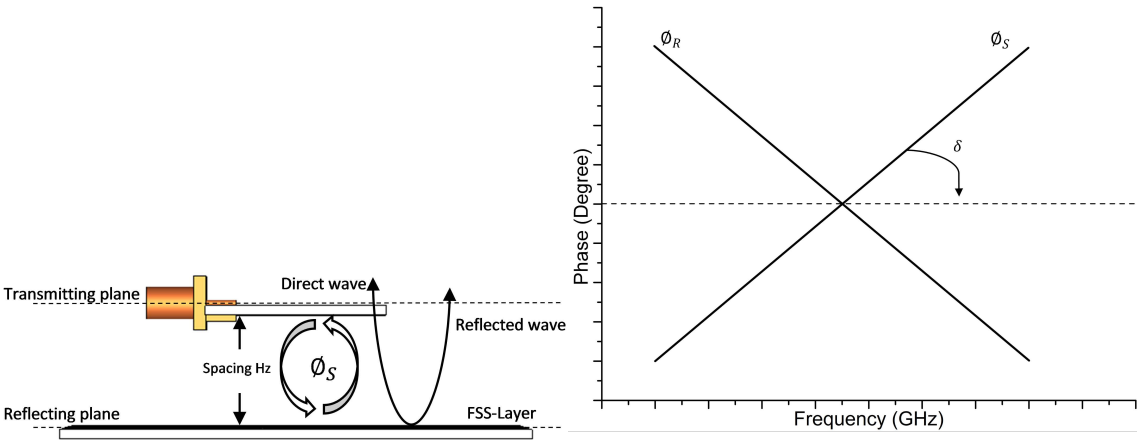

(a) (b)

Figure 4-14: Geometry of (a) Proposed FSS-Backed UWB Antenna, and (b) Ideal frequency response of the single-layer FSS reflection phase ϕ_R and phase delay ϕ_S.

The simulated return loss for the FSS-backed antenna, is shown in Figure 4-15(a). These values are obtained by studying the antenna at different distances H_z. Figure 4-15(b) illustrates this variation effect on the bandwidth and peak gain of the proposed design.

From Figure 4-15, it is clearly noticed that by changing the spacing H_z, both the bandwidth and peak gain are affected accordingly. Increasing the spacing H_z improved the bandwidth significantly, reaching its maximum (3 to 13.8 GHz) at H_z = 18.74 mm, and decreased slightly and stayed almost stable when increasing the spacing H_z.

Moreover, the peak gain exhibited a different trait when increasing the spacing H_z, meaning peak gain is at its highest values when the spacing H_z is small, and reaching its maximum at H_z =18.74 (9.13 dBi), and decreasing at higher values of H_z. Thus, between the maximum bandwidth and higher peak gain, H_z = 18.74 mm, is the optimal distance between both the proposed UWB antenna and its FSS reflector. This is all due to the fact that, the direct and the reflected waves are matched with a phase of zero or an integral multiple of 2π (n x 2π), which leads to the enhancement of the antenna gain.

Using the proposed FSS's reflection phase ϕ_R (See Figure 4-12(b)), and by calculating the path delay phase (ϕ_S) at H_z =18.74 using Equation (12), we can find the total phase shift at that distance, to further validate our numerical simulation

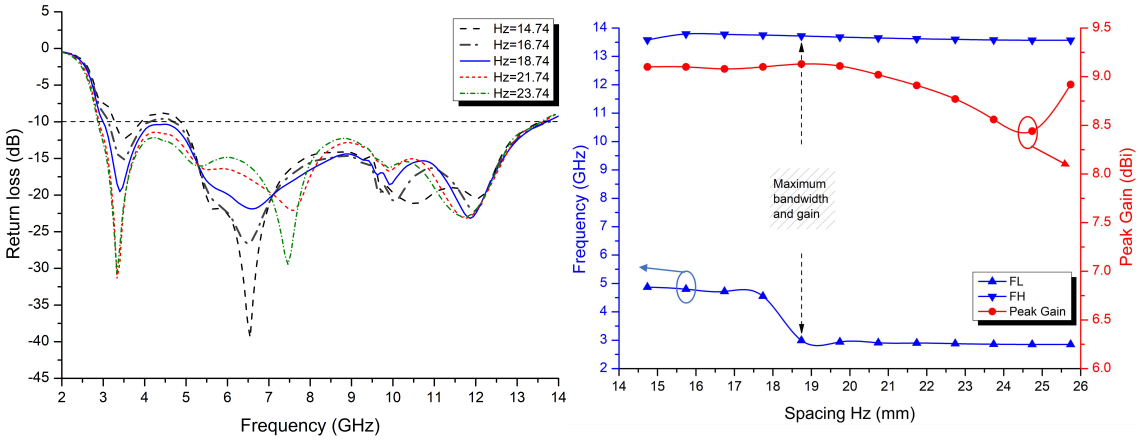

(a) (b)

Figure 4-15: Simulated (a) reflection coefficients of the proposed FSS-Antenna, (b) the bandwidth and gain variations at different spacings Hz.

results. Since the path delay phase (ϕ_S) relied mainly in both a certain frequency f_r and spacing H_z, the proposed FSS structure exhibits a Zero-Phase reflection at 8 GHz, and its half wavelength consequently is 18.74 mm, the ϕ_S equals to 2π (see Figure 4-16.). By using Equation (11), the total phase shift is equal to 2π at 8 GHz andH_z =18.74 mm.

From Figure 4-16., it is clearly noticed that our proposed FSS design displayed n x 2π (n=1) phase shift between the direct and the reflected waves at H_z = 18.74 mm and f_e=8 GHz, and this leads to a compatibility and phase coherence throughout the whole UWB spectrum. Thus, both the antenna bandwidth and gain are enhanced accordantly.

Figure 4-17. depicts the simulated return loss and peak gain for both antenna with and without the proposed FSS reflector, where it is clearly noticed that the average gain drastically improved (from 4 to 7.84 dBi) for all UWB spectrum (3.1-10.6 GHz), with a peak gain of 9.13 dBi by using our proposed FSS structure. Both FSS-B and FSS-C alongside our proposed UWB antenna, are fabricated and validated in the next section.

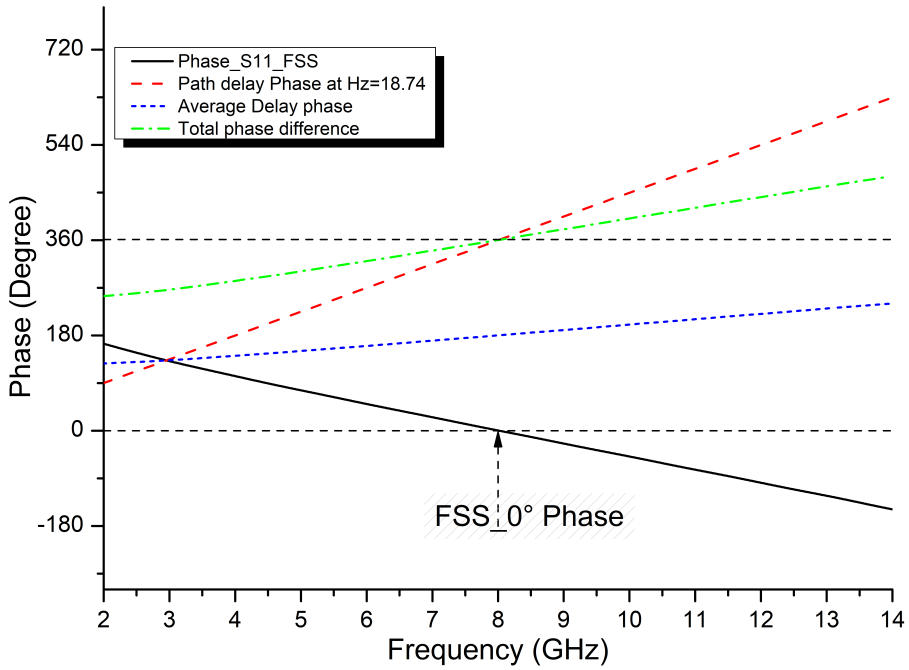

Figure 4-16: Phase variations analysis.

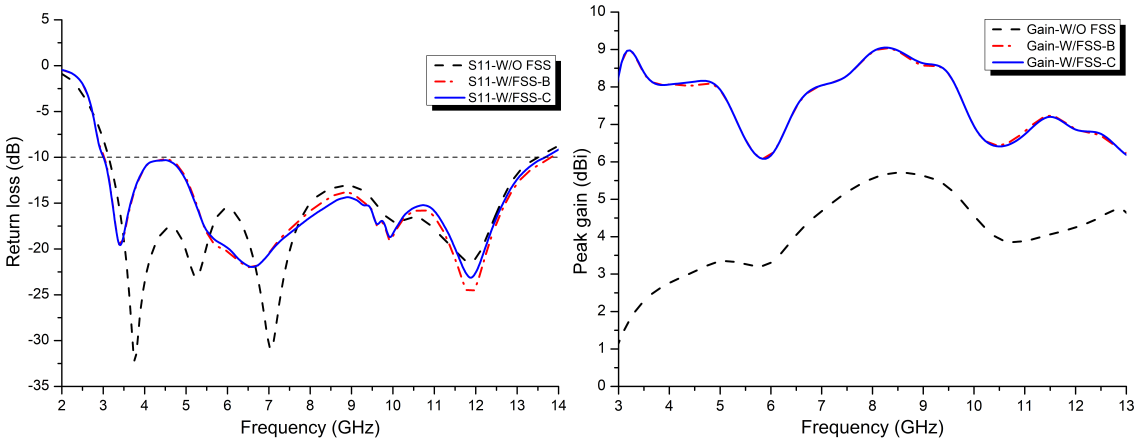

(a) (b)

Figure 4-17: Simulated (a) reflections coefficients (S_{11}), and (b) gain for both antennas with and without FSS reflector, at H_z =18.74 mm.

4.4 Prototypes Fabrication and Measurement Results

The prototypes including both the proposed UWB antenna and the FSS reflecting layers were fabricated using the same substrate used in simulation to validate our findings. Figure 4-18. depicts the final fabricated prototypes, with and without the FSS layer, and this latter is based on the two synthesized FSS unit cells FSS-B and FSS-C, due to their remarkable performances. The UWB antenna is suspended over these FSS layers using foam spacers during measurements at the optimal spacing Hz of 18.74 mm. The reflection coefficients characteristics of all fabricated antennas are analysed and measured using Agilent 8722ES VNA, and the results are illustrated in Figure 4-19(a). From simulation results for both with and without FSS layer, it is clearly noticed that they are in good agreements with the measured ones. the antenna without FSS exhibits a bandwidth in the range of 3.4 to 13.8 GHz, whereas in the case of the FSS-backed ones, the antenna with FSS-B covered the bandwidth of 3.3 to 13.9 GHz, while the one with FSS-C the bandwidth is from 3.1 to 13.9 GHz, meaning all antennas are in great agreements with simulation results with a slight shift in the lower end frequency, due to the phase matching and fabrication errors. Moreover, the peak gain and radiation patterns for all proposed prototypes were measured in an anechoic chamber.

(a) (b)

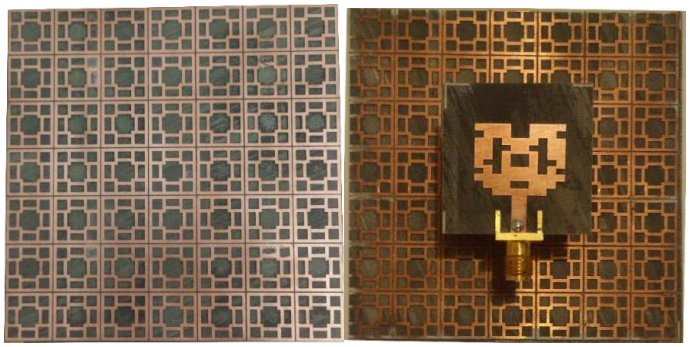

(c) (d)

Figure 4-18: Final fabricated prototypes, (a) UWB antenna front and back view, (b) FSS-B layer, (c) FSS-C layer, and (d) the final proposed antenna.

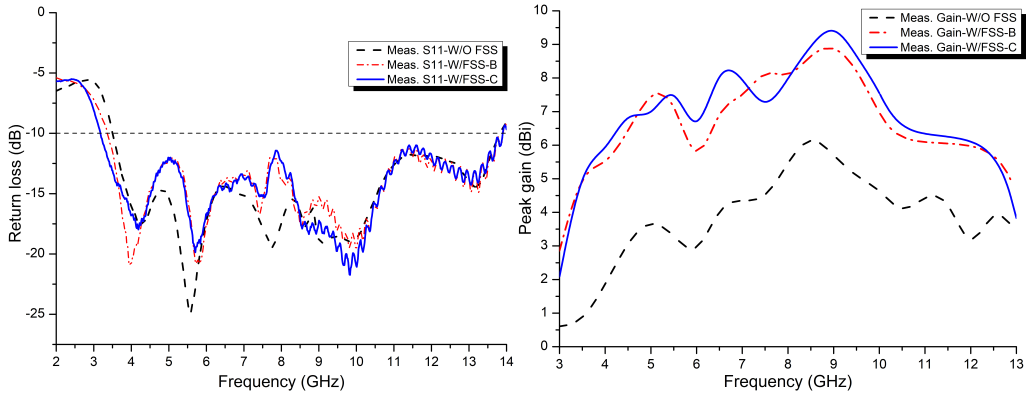

(a) (b)

Figure 4-19: Measured (a) reflections coefficients (S_{11}), and (b) gain for both antennas with and without FSS reflectors, at H_z =18.74 mm.

First, the gain calculation of the antenna under test (AUT) is performed using the following [82]:

$$G_{AUT} = G_{horn} - P_{horn} + P_{AUT} \tag{4.13}$$

where G_{horn} is the gain of the reference antenna, in this case a standard horn antenna. P_{horn} and P_{AUT} are the received power at the spectrum analysis of the standard horn (receiver mode), and the antenna under test, respectively.

The measured peak gains for both the antenna with and without FSS layer, are depicted in Figure 4-19(b). It is clearly noted that by using an FSS-based reflector the peak gain over the UWB spectrum is improved. The antenna without FSS, exhibits a maximum peak gain of 6.3 dBi and an average of 3.7 dBi all over the UWB spectrum, whereas for the case of the two other FSS based antennas, the maximum peak gain is 9.03 dBi and 9.7 dBi for FSS-B and FSS-C designs, alongside the average peak gain of 6.87 dBi and 7.11 dBi, thought out the UWB spectrum, respectively. Thus, an improvement of 3.4 and 3.41 dBi for maximum and average peak gain, in comparison with the antenna without FSS. It is observed that both simulation and measurements results are in good agreement.

For further analysis, the normalized simulated and measured radiation patterns of both antennas, with and without FSS layer (FSS-C in this case), are illustrated in Figure 4-20., at three different frequencies, 4.5, 7 and 10.5 GHz, in both H- and E-planes. The obtained radiation patterns (simulated and measured) of the antenna without FSS, are bidirectional in the E-plane, where as in the case of the H-plane the patterns are quasi-omnidirectional, with different orientations. The antenna with FSS reflecting layer exhibited more directional nature in both planes, with much lower sidelobe levels, and a narrower beamwidth. This is further noticed when the number of FSS unit cells is increased. Both simulation and measurements results are in good agreement, with a slight difference due to fabrication errors, phase mismatch between the antenna and the FSS layer, etc. with these features, the FSS-backed design could be a potential candidate, allowing a high gain, larger bandwidth and low profile. Finally, the proposed FSS designs are compared (using Fr-4 substrate) to others in the literature, taking into account the unit cell size (λ at the lower end frequency), the stop band and the number of FSS planes and layers, and the comparison is summarized in Table 4.2. From this comparison, it can be concluded that the proposed design outperforms the other ones in terms compactness and stopband bandwidth.

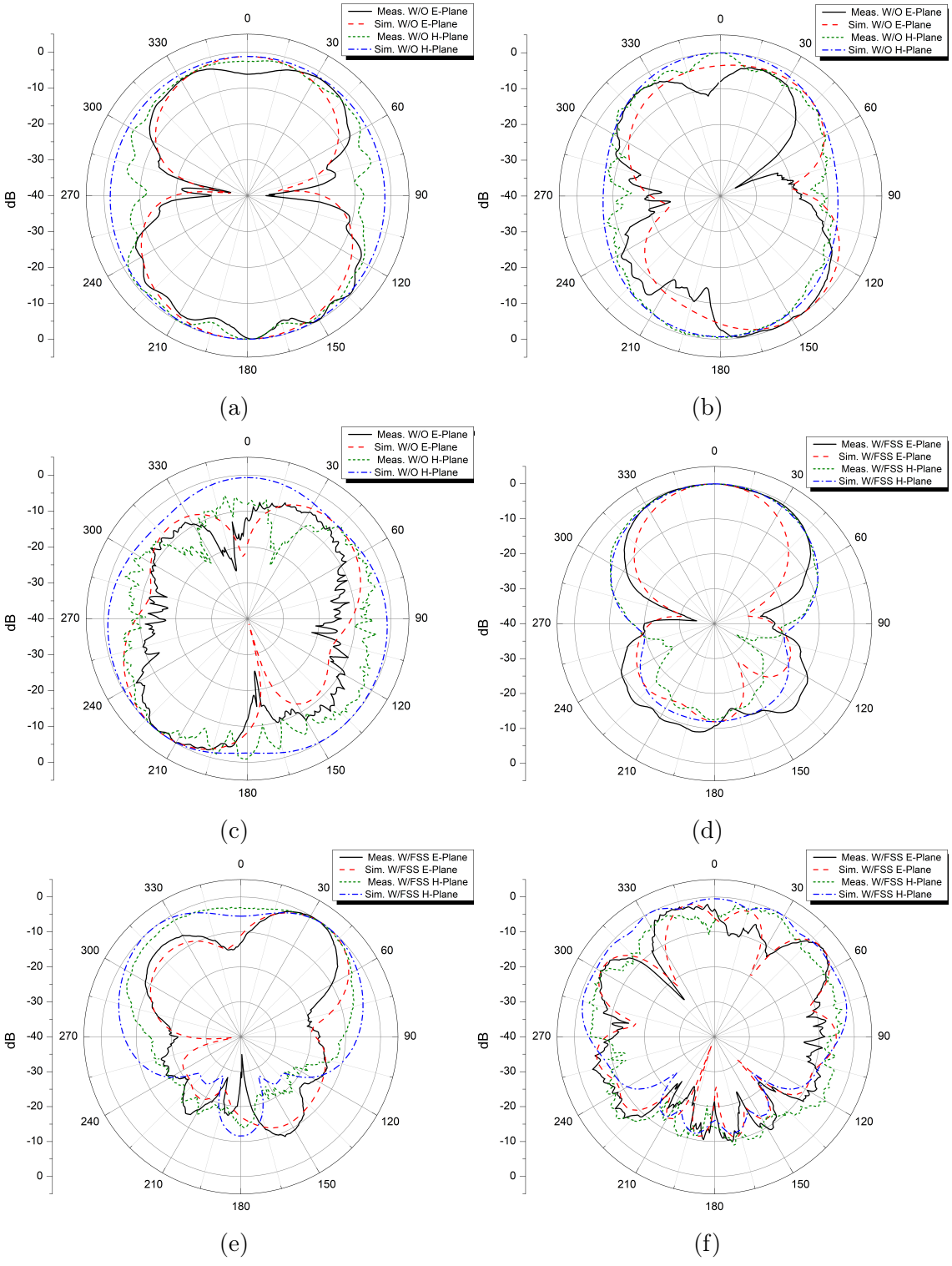

Figure 4-20: Normalized simulated and measured radiation patterns for antenna without FSS (a, b, and c) and FSS-based one (d, e, and f) at 4.5, 7, and 10.5 GHz.

Table 4.2: Proposed FSS designs compared to other related works

Ref. No	Stop-Band (GHz)	Unit cell size	No. of FSS planes
[80]	2.6–11.1	0.095λ x 0.095λ	One
[81]	4-7	0.12λ x 0.12λ	One
[83]	2.8-12.2	0.098λ x 0.098λ	One
[84]	4-12	0.22λ x 0.22λ	Two
[85]	3-11.64	0.12λ x 0.12λ	Two
[86]	3-15	0.108λ x 0.108λ	Two
This work (Fr-4 Substrate)			
FSS-A	2.6–12	0.095λ x 0.095λ	One
FSS-B	2.5–13.7	0.091λ x 0.091λ	One
FSS-C	2.6–13.5	0.095λ x 0.095λ	One

4.5 Summary

In this chapter, a topology optimized UWB antenna using a genetic algorithm embedded in MATLAB, with an interface with CST Microwave studio, has been designed, simulated and validated by measurements, alongside a compact FSS layer, covering the whole UWB spectrum. Both the UWB antenna and the FSS layer have been designed and fabricated on a Rogers RO4350B substrate. The size of the proposed FSS unit cell is only 0.1 λ x 0.1 λ, with a broad bandwidth of 2.9 to 14.5 GHz. The fabricated UWB antenna without FSS layer, exhibits a bandwidth of 3.4 to 13.8 GHz, a maximum peak gain of 6.3 dBi, where as in the case of the proposed FSS-backed antenna, the bandwidth was from 3.1 to 13.9 GHz, and the maximum peak gain achieved is 9.7 dBi, leading to a 3.4 dBi improvement in terms of peak gain. Aside from gain enhancement, using FSS reflecting layer shapes the radiation pattern to be a more directive one, with a narrower beamwidth, and lower sidelobe levels. The simulation and measurement results are in good agreement, with a slight difference due to fabrication errors and mismatching between the FSS layer and the UWB antenna. The proposed FSS-backed antenna can be a great candidate for high gain UWB applications.

Chapter 5

High gain and Wideband Fabry-Perot Resonator Antenna based on a compact single PRS layer

5.1 Introduction

With the increasing demand for high-data rates and low latency wireless communication systems, wideband and highly directive antennas are becoming attractive subjects in both the academic and industrial sectors, especially in the upper microwave region and the untapped millimeter wave spectrum [87]. High gain antennas have been designed using traditional technologies such as reflectors, waveguide horn antennas [88, 89], and microstrip fed patch arrays [90]; however, these aforementioned techniques have some major disadvantages in terms of design complexity, high fabrication cost, and feeding-network induced losses.

One approach to tackle these disadvantages is by using a Fabry-Perot Resonator Antenna (FPRA), which consist of a Partially Reflective Surface (PRS) based superstrate placed at a distance (usually half a wavelength) from the ground plane, creating an air-gaped cavity, and excited by a feeding source antenna (single or array) backed by the ground-plane, making this type of technique a simple, and cost effective approach for achieving a significant enhancement in terms of antenna radiation characteristics [91, 92, 93, 94].

However, this kind of antenna suffer even more from the inherent narrow bandwidth due to the fact that the antenna's characteristics, such as its frequency, radiation patterns, gain and bandwidth are mainly determined by the PRS layer properties, and this latter invokes the typical narrow band cavity [95].

To overcome this issue, many studies have been conducted to improve the operation bandwidth while keeping higher gain performance of the FPRA. In [96, 97], a multi-layer superstrates based on periodically printed FSS arrays have been used for bandwidth enhancement on a single and dual-band application, whereas in [98] a dielectric based one has been used to achieve a broadband EBG resonator. A side of improving the bandwidth, using multi-layer superstrates increases the profile of the antenna making it a bulky structure.

Another effective technique yet a complicated one, which involves making a dielectric slab with gradient permittivity as in [99, 100].

A more convenient method using double-sided printed metallic layers on a dielectric medium, has attracted the interest of many researchers [101, 102, 103], since this superstrate produces a positive reflection phase gradient over a particular range of frequencies to broaden the 3-dB gain bandwidth of the FPRA, while keeping a degree of compactness and low profile, since the height of the resonance cavity is only a half wavelength. This design not only provides a high gain but also low fabrication cost.

In this chapter, a compact PRS based layer is proposed as a superstrate to an aperture-coupled wideband source antenna, to form a Fabry-Perot Resonator and to improve its gain bandwidth. The proposed FPRA unit cell is generated using an automated topology synthesizing system, established using a link between the genetic algorithm embedded in MATLAB and the commercial simulator CST Microwave Studio through a VBA based connection. A Binary Particle Swarm Optimization (BPSO) algorithm [12] can also be used instead of the genetic algorithm to achieve the same objective of a compact with positive reflection phase gradient PRS unit cell.

The proposed PRS designing process is applied on two different radio frequency spectrums namely the Ku-band and the future of the wireless communication sys-

tems 5G band.

5.2 Wide Band FPRA Antenna

Fabry-Perot resonator antenna (FPRA) is considered a highly directive one [104]. It consists of a simple radiating source backed by a ground-plane, and a PRS (see Figure 5-1).

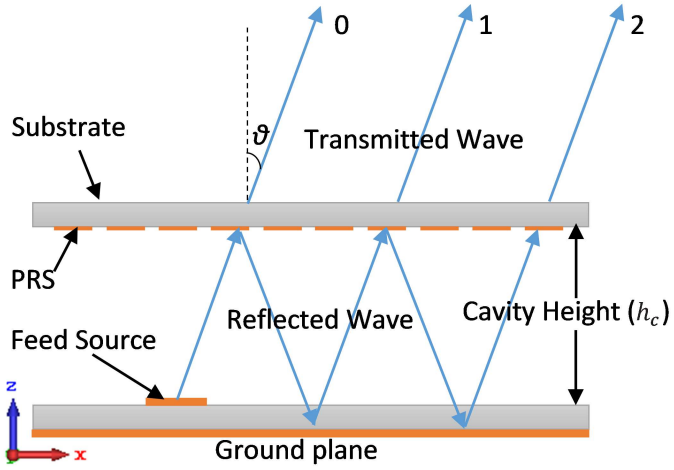

Figure 5-1: Schematic diagram of a Fabry-Perot resonator.

Gain and directivity improvements are achieved, when the spacing h_c between the ground and the PRS, satisfies the cavity resonance condition according to the ray-tracing analysis in [105], and equals to the following:

$$h_c = \frac{c}{4\pi f_r}\left(\varphi_{PRS} + \varphi_{GND} - 2N\pi\right) \tag{5.1}$$

where φ_{PRS} and φ_{GND} are both the reflection phases of the PRS and the ground plane, respectively. N is the resonance mode order, and is equal to 0,1, 2,... etc. For a low profile Fabry-Perrot based resonator antenna, N is set to be 0. f_r and c are the resonance frequency and the speed of light in the vacuum, respectively.

Assuming that the source antenna directivity is D_{ref} at a particular frequency f_r, the directivity of the FPRA antenna would be the summation of this latter and

the PRS directivity D_{PRS}, which is expressed as:

$$D_{PRS} = 10log\left(\frac{1+\Gamma}{1-\Gamma}\right), \tag{5.2}$$

where Γ is the reflection magnitude of the PRS superstrate layer, and the total theoretical FPRA directivity is formulated as follows [87]:

$$D_{FPRA} = D_{ref} + D_{PRS} \tag{5.3}$$

From Equations (2) and (3), it is clearly noticed that the directivity of FPRA is positively correlated with the PRS reflection amplitude, thus, the larger this latter is, the better the overall directivity of the FPRA. Due to the fact that the cavity spacing h_c and the partially reflective surface phase φ_{PRS}, are frequency-sensitive, conventional FPRAs only possess a small radiation bandwidth. Assuming that the dielectric slab is lossless, the aperture surface of the FPRA for a required directivity can be approximated using the following formula [106]:

$$A = \frac{10^{\frac{D_{FPRA}}{10}}\lambda^2}{\pi^2} \tag{5.4}$$

where λ is the operating wavelength of the FPRA. By taking a PEC ground plane (φ_{GND}=π), the PRS reflection phase is expressed by rearranging (1) as the following:

$$\varphi_{PRS} = \frac{4\pi h_c}{c} f_r + (2N-1)\,\pi \tag{5.5}$$

From (5) it can be noted that if the reflection phase of the PRS increases with the resonance frequency f_r (a positive slope versus frequency), the FPRAs would operate in a wider frequency band with an enhanced gain bandwidth. Therefore, a PRS with positive reflection phase gradient is needed, for designing a wideband and high gain Fabry Perrot based Resonator Antenna.

5.3 Ku-band Antenna design and analysis

5.3.1 Proposed PRS Structure

In the previous section, a PRS with positive phase gradient is discussed to be the main key point for designing a wideband FPRA. Therefore, first of all, we should carefully design one that meets the aforementioned requirement.

First, a simple circular ring is etched on one side of a Rogers RT/duroid 5880 dielectric slab ($\varepsilon_{r1} = 2.2$, tanδ=0.0009), with a thickness h_PRS of 1.575 mm, creating the initial PRS unit cell having the following design parameters: w_PRS=6 mm, ro=2.9 mm, ri=1.4 mm and g=0.2 mm. Fig. 2(a) shows the geometry of the initial PRS unit cell.

The PRS unit cell is designed and simulated using CST Microwave studio, and the reflection phase characteristics analyzing setup is depicted in Figure 5-2 (b), where boundary conditions are applied as follow: along the ± x-axis, the Perfect Magnetic Condition (PMC) is applied, whereas in the case of the ±y-axis, the Perfect Electric Condition (PEC) is used, with two wave ports set at distance of $\lambda/2$ from the unit cell under investigation along the z-axis, with open boundary condition, so only the normal incidence is considered here.

The simulated magnitude and phase of the reflection coefficient response of the initial PRS unit cell is shown in Figure 5-3 Where it's clearly noticed that the PRS unit cell is highly reflective around the frequency band of interest with a magnitude of Γ=0.9 at 15 GHz. A high reflection magnitude is targeted for a high gain antenna. However, the reflection phase of the unit cell as depicted in Figure 5-3, is decreasing as the frequency increases, which leads to a narrower bandwidth. A new unit cell that provides a positive reflection phase gradient, is then proposed to broaden the antenna bandwidth while keeping a high gain performance.

A partially reflective surface (PRS) unit cells are printed on either one or both sides of the dielectric slab, just like in this case, where it is printed on both sides of the same dielectric substrate used on the previous PRS design, namely the Rogers RT/duroid 5880, with the same thickness of 1.57 mm.

The next approach is based on the same PRS unit cell, and using a pixelated

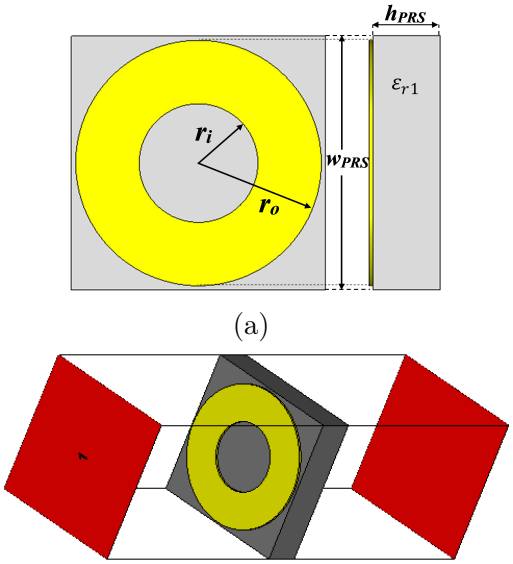

(a)

(b)

Figure 5-2: (a) Geometry of the initial PRS unit cell, (b) Analysis setup of the unit cell (CST).

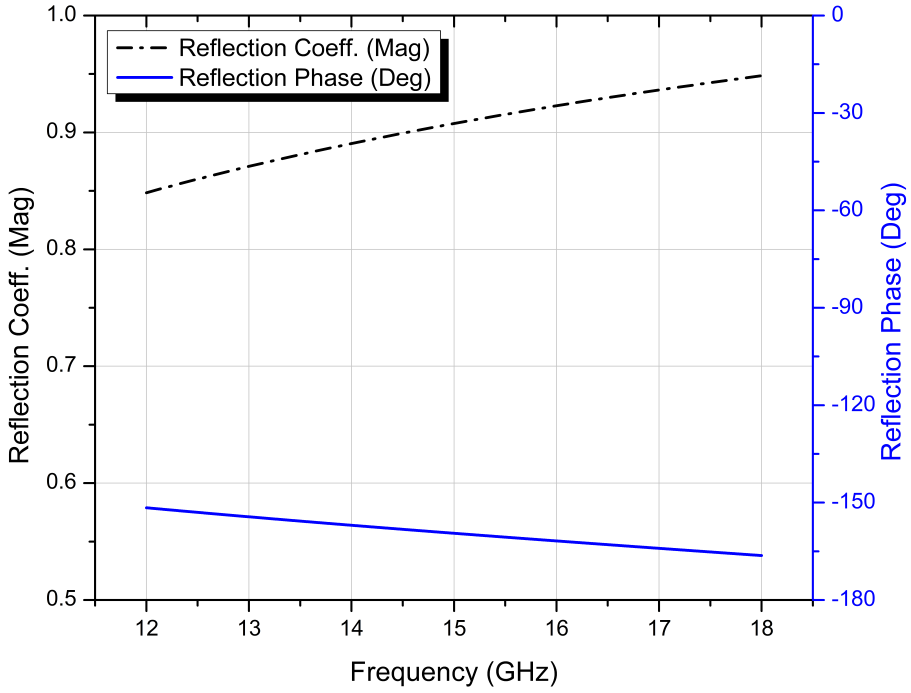

Figure 5-3: Reflection phase and magnitude of the initial PRS unit cell.

based pattern on the other side of the unit cell, to create a positive phase gradient that follows the optimal phase, for increasing the bandwidth.

Genetic algorithm (GA) based optimizations were carried out, yielding to great potential in finding no-conventional solutions to Electromagnetic based problems.

In [1], the genetic algorithm has been used to optimize an EBG structure for gain and bandwidth enhancement, whereas in the case of [9], an AMC based reflector has been optimized using the same technique to achieve an important enhancement in the peak gain and front-to-back ratio, alongside a low side-lobe level (SLL), for 5G applications.

A well-established VBA based connection between CST Microwave studio and MATLAB's embedded GA is used here, to create an automated pattern synthesizing system. The upper side of the PRS structure is the targeted area on this procedure. Each PRS unit cell is pixelated into n x m pixels, and are defined using binary encoding, where having the value of either 1 or 0 indicates the presence or the absence of copper on the pixelated sub-cell (on top of the dielectric slab).

Increasing the number of pixelated cells, increases also the number of total possible structures, making it an impractical way in solving such a problem, so, a confined in search space global optimization solution is needed, for finding the optimal candidate, according to a predefined fitness function, making the genetic algorithm an effective way in doing so.

In the proposed designing scenario, the fitness function is defined as the Root-Mean-Square Error (RMSE) between the reflection coefficient phase response of the generated PRS unit cell under investigation, and the optimum phase, and is defined as:

$$Fit = RMSE(Phase_{PRS}, Phase_{Optimum}) \tag{5.6}$$

where

$$RMSE = \sqrt{\frac{\sum_{n=1}^{N} (Phase_{PRS} - Phase_{Optimum})}{N}} \tag{5.7}$$

The reflection coefficient phase of the PRS unit cell, is taken at equal frequencies f_i, with the total number of N = 1001 frequency points, within the designated overlapping frequency band of interest ($f_{min} \leq fi \leq f_{max}$).

The implemented flowchart of the GA based optimization process for a positive phase gradient PRS unit cell, is shown in Figure 5-4

As a starting point, the PRS unit cell is discretized into 12 × 12 pixels, which provides a resolution of 0.5 × 0.5 mm, that is chosen while taking into account the

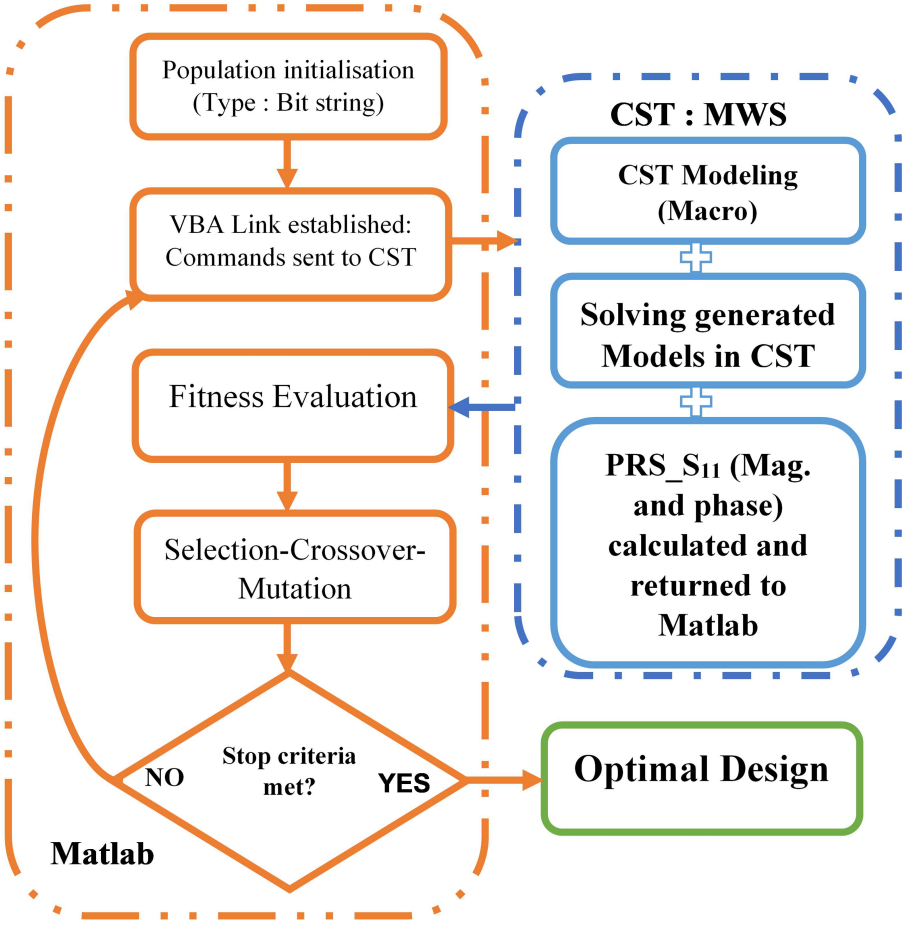

Figure 5-4: The Proposed flowchart of the GA optimization process for the PRS unit cell.

fabrication constrains, and to maintain the geometrical flexibility.

A 12 x 12 discretized unit cell needs to be represented by 144 binary encoded pixels, and this led to a large search space for the optimal solution, which is an impractical and time-consuming process. To overcome this, a four-folded symmetry is imposed, as shown in Figure 5-5. As a result, the search space for the optimal solution (the number of bits required to represent the PRS unit cell) is reduced drastically to 21. The proposed optimization process tries to manipulate the reflection coefficient phase of the possible PRS design candidates, to produce a PRS unit cell with a phase that closely resembles the positive gradient optimum phase, within the frequency band of interest, by using the proposed genetic algorithm, with a uniform mutation at rate of 0.001, a single point crossover, and the tournament selection as its parameters.

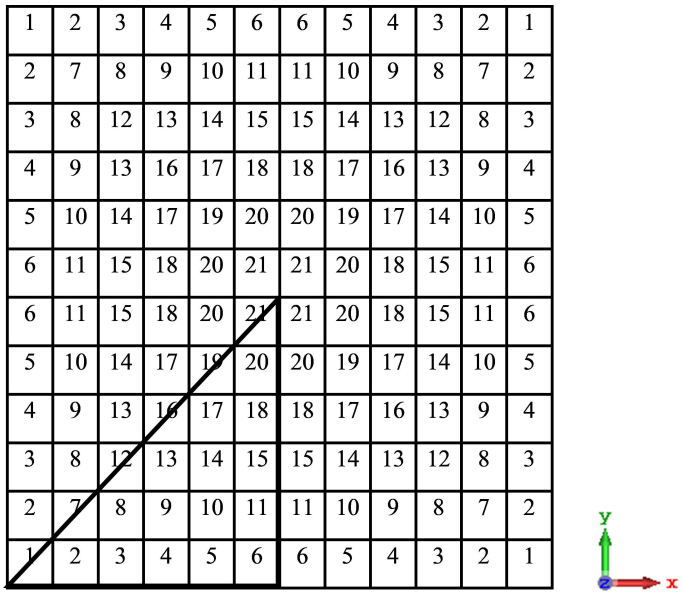

Figure 5-5: The proposed four-folded symmetry pixelated PRS unit cell (12 x12).

The population size is set to be 200 different binary strings randomly selected, with each one representing a specific pixelated PRS unit cell, and the number of iterations (generations) is set to be 20.

Once all the 200-initial pixelated PRS structures are evaluated, they are ranked and the top performing ones are selected for the crossover and mutation processes, creating a new population of 200 PRS candidates going through the same evaluation process. This later is repeated until the desired fitness value is achieved (Fit tends towards zero) or until the maximum number of iterations is reached.

The best achieved PRS design is obtained at the 10th iteration, when the stop criterion is met, as shown in Figure 5-6 (a), where it is clearly shown that the final design doesn't suffer from the infinitesimal connection problem, between two sub-cells, when these constellations $\binom{10}{01}$ or $\binom{01}{10}$ are present, which could lead to a malfunctioning PRS structure, due to fabrication tolerances. Also, since the design imposes the four-folded symmetry, the PRS unit cell exhibits polarization insensitivity, which makes it also applicable to circular polarized antennas.

The binary string of the final optimized PRS unit cell is:

BPRS = 0 1 0 1 0 0 1 1 1 0 1 0 0 0 1 1 1 1 1 0 0.

The resulted reflection coefficient phase of the optimized PRS has a positive gradient and is almost perfectly resembles that of the optimum PRS over a wide

bandwidth spectrum range, with a relatively high reflection magnitude (See Figure 5-6 (b)), which makes the proposed PRS design a potential superstrate candidate for a wideband and high gain FPRA

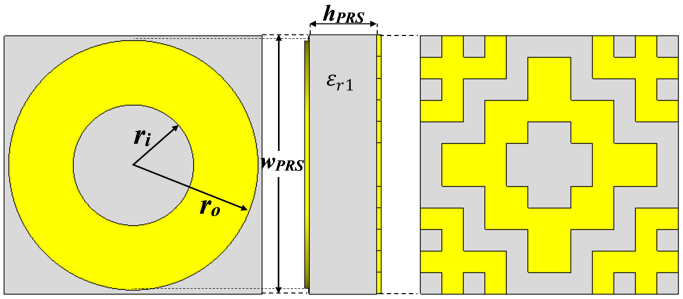

(a)

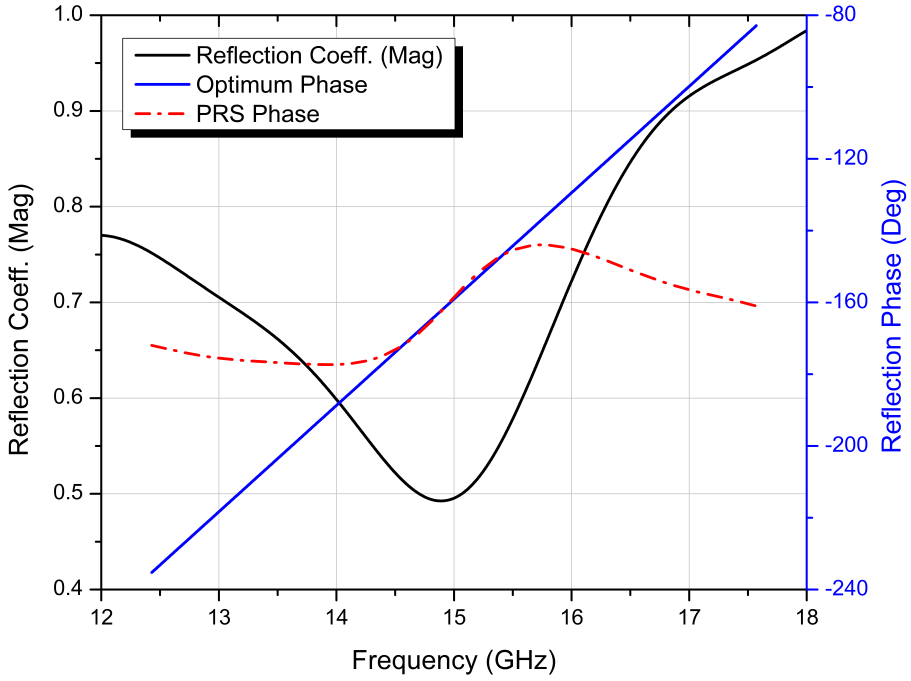

(b)

Figure 5-6: (a) The GA based final optimized PRS design, and (b) reflection coefficient's magnitude and phase of the proposed PRS unit cell.

5.3.2 Feeding Antenna

The feeding source antenna for an FPRA is as important and vital to its performances as the PRS structure, thus a well-designed feeding antenna is a crucial part in designing a high gain and wideband FPRA antenna. Several types of exciting sources have been reported in the literature, such as a suspended metal-strip over a

ground plane [95], a probe-fed patch antenna [107], and a waveguide aperture-based feeding antenna [108].

An air-gaped slot-coupled patch antenna is a good candidate for a high gain and wideband FPRA antenna, due to its low profile, ease of feeding and fabrication, a stable broadside radiation and wide bandwidth capability.

The proposed feed antenna design is depicted in Figure 5-7. it consists of a parasitic patch, coupled to a feeding line through a slotted ground plane (bottom layer), and spaced by an airgap h_{air} = 2 mm, for surface waves suppression, since this latter can contribute to performance degradation of the FPRA cavity [109]. An impedance matching network is added to the feedline to improve the bandwidth. The Rogers RT/ duroid 5880 material having a thickness (h_s) of 0.787 mm, permittivity ε_{r2}= 2.2, and a loss tangent of 0.0009, is used as a substrate for both the parasitic patch and the bottom layer (ground plane and the feed line). The antenna design parameters are summarized in Table 5.1.

Both the simulated reflection coefficient (S_{11}) and the peak gain of the feed antenna are illustrated in Figure 5-8 a & b, respectively, where it is clearly noticed

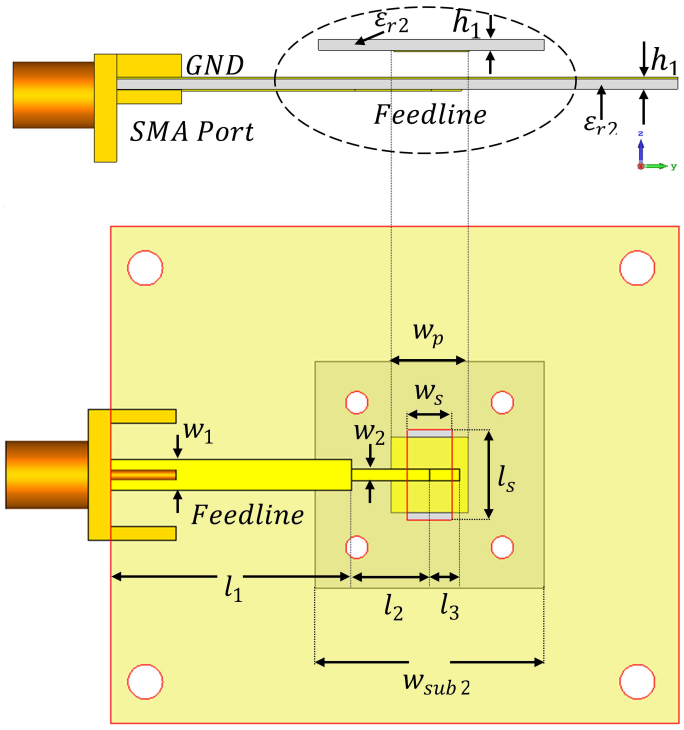

Figure 5-7: The schematic diagram of the slot-coupled patch antenna.

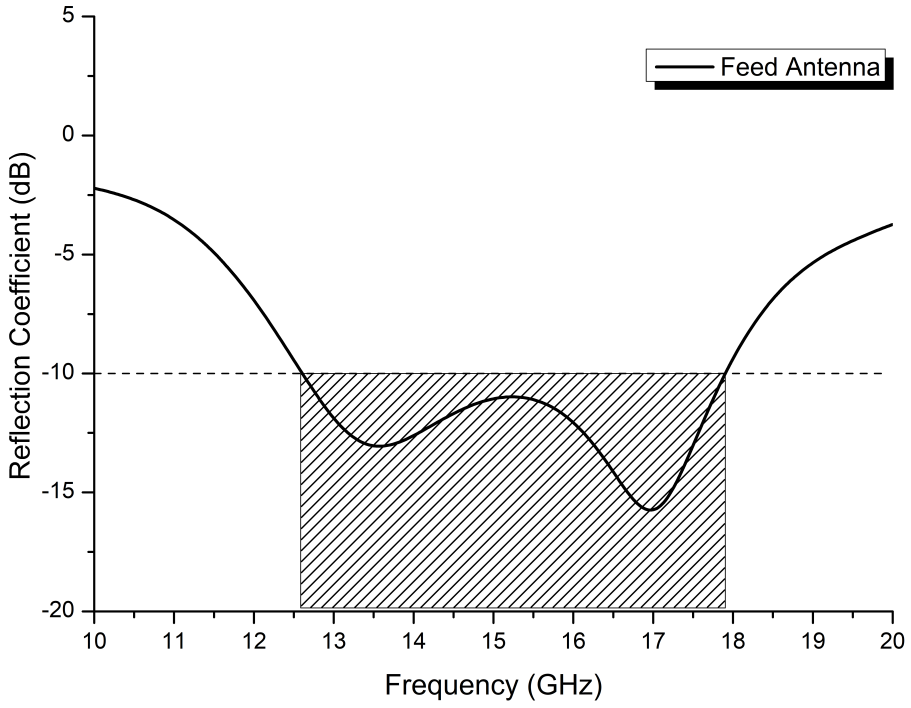

(a)

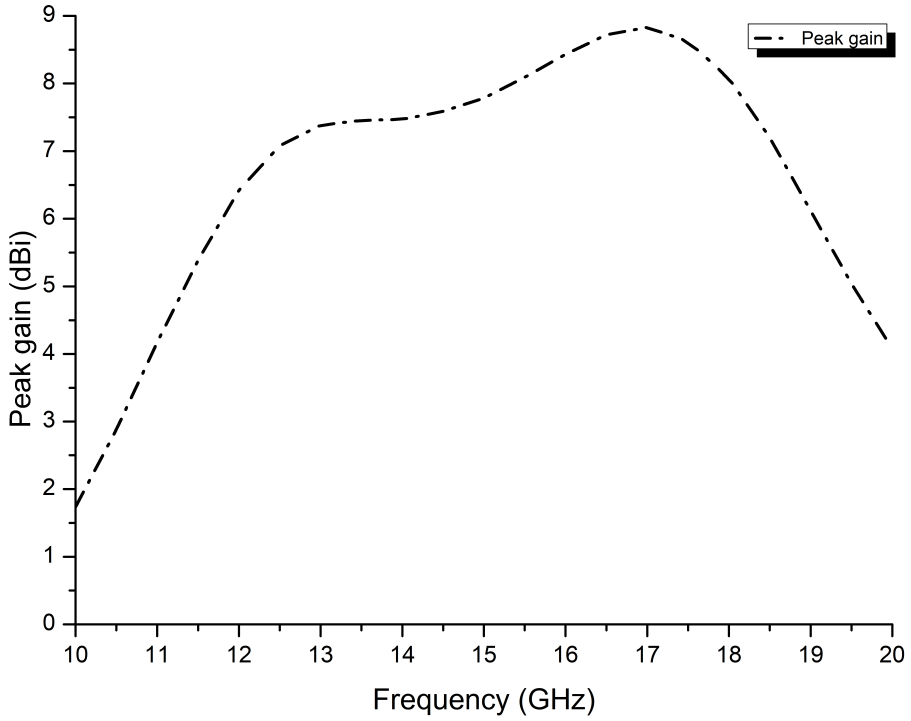

(b)

Figure 5-8: The simulated results of the slot-coupled patch antenna (a) reflection coefficient, (b) peak gain.

that the impedance bandwidth almost covers the whole Ku-band spectrum, ranging from 12.6 GHz to 18 GHz. Within this band, the peak gain increased from 7 to 8.8

Table 5.1: The slot-coupled patch antenna design parameters.

Parameter	Value (mm)	Parameter	Value (mm)
h_1	0.79	l_3	2.2
w_1	2.3	w_s	3.2
w_2	0.9	l_s	6.5
l_1	17.4	w_p	5.5
l_2	5.6	w_{sub2}	16.5

dBi, making it a good candidate for being a feeding source for the proposed FPRA antenna to be designed in the next section.

5.3.3 Proposed Ku-band FPRA Antenna

The optimized PRS structure (Figure 5-6) is applied as a superstrate layer to the proposed slot-coupled feed antenna in the previous section (Figure 5-7), creating the proposed wideband and high gain Fabry-Perot resonator antenna as shown in Figure 5-9. The PRS superstrate is suspended over the shared ground plane at a distance h_c using M2 nylon screws (2 mm in diameter) at the four corners, and they are also taken into account during the simulation process, alongside a 50 Ohm SMA connector modeled also in CST Microwave studio. A preliminary determination of h_c can be achieved using both the simulated results of the proposed PRS unit cell reflection coefficient phase (φ_{PRS}) in Figure 5-6 (b) and (1), where f_r is the FPRA's center frequency and φ_{PRS} is taken also at that same center frequency too. The reflection coefficient phase of the PRS at the center frequency of 15GHz is about -158.6° (see Figure 5-6 (b)), and by using (1), the spacing hc is about 10.5mm. Further optimization is need to be performed to find the optimal distance to achieve the best performance of the Fabry-Perot Resonator Antenna.

The aperture size of the proposed FPRA antenna is estimated by using (4), where the wavelength λ is taken at the lower end frequency (12.6 GHz) of the antenna, which is 23.8 mm, and the corresponding estimated FPRA directivity (DFPRA) is around 13.73 dBi using both (2) and (3), therefore, the aperture size is about 36.83 mm x 36.83 mm.

Thus, a PRS structure of an aperture size of 36 mm × 36 mm is used as the

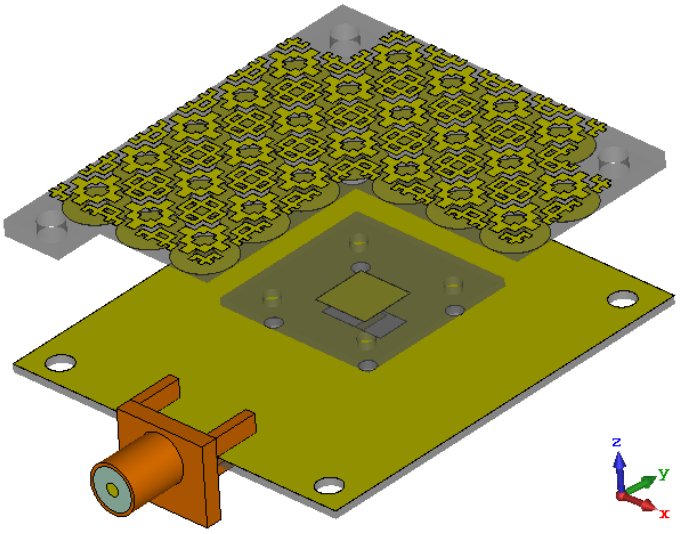

Figure 5-9: The proposed wideband FPRA design.

superstrate for the proposed Fabry Perot resonator antenna, which consists of an array of 6×6 PRS unit cells since this latter's effective size is 6 mm. Using the previously estimated parameters, namely the aperture size (36mm x 36mm), and the cavity air gap h_c = 10.5 mm, the resulted reflection coefficient S_{11} of the proposed FPRA is illustrated in Figure 5-10, where the impedance bandwidth ($|S_{11}|$<-10dB) is about 3.24 GHz divided into a dual band, ranging from 14.18 to 16.52 GHz, and from 17.1 to 18 GHz. The peak gain is 14.4 dBi at 14.5 GHz.

The air gaped cavity of the Fabry Perot resonator antenna is an important factor in designing a wideband antenna with high gain; therefore, the influence of changing such a parameter on the overall performance of the proposed antenna is investigated.

All other parameters are fixed, while the cavity height is changed in a step of 0.5 mm from 10.5 to 13 mm, to see the effect of the cavity height variation on the S_{11} impedance bandwidth, the peak gain, and the 3-dB gain bandwidth of the FPRA. The results are depicted in Figure 5-10 & Figure 5-11 and summarized in Table 5.2. From there, it is clearly noticed that, when the cavity thickness increases, both the impedance and 3-dB gain bandwidths are gradually expanded, while the peak gain is reduced, accordingly, as expected from an FPRA.

For a high gain FPRA with a wider operating bandwidth, and based on the results illustrated in both Figure 5-10 & Figure 5-11, and Table 5.2, it can be

Table 5.2: Summarized results of the proposed design at different cavity spacings

Cavity spacing h_c (mm)	$\|S11\| < -10dB$ BW (GHz)	3-dB gain bandwidth(GHz)
10.5	14.18-16.52 (15.24%) 17.1-18 (5.12%)	13.3-17.8 (28.93%)
11	13.29-15.2 (13.40 %) 15.71-17.68 (11.79%)	13-17.6 (30.06%)
11.5	12.95-17.56 (30.21%)	12.77-17.38 (30.58%)
12	12.61-17.51 (32.53%)	12.4-17.3 (32.99%)
12.5	12.26-17.52 (35.32%)	11.99-17.26 (36.03%)
13	11.9-17.6 (38.64%)	11.6-17.24 (39.11%)

concluded that the optimal cavity height is 13 mm, where the proposed FPRA exhibited an outstanding impedance bandwidth performance of 38.64 % ranging from 11.9 to 17.6 GHz (Figure 5-10), and a 3-dB gain bandwidth of 39.11 % (11.6 to 17.24 GHz), with a maximum peak gain of 14.21 dBi at 16 GHz as shown in Figure 5-11. Radiation patterns at three different frequencies (12.5, 14 and 16 GHz) in both E-and H- planes are simulated and depicted in Figure 5-14. From this figure, it can be noted that the patterns are directive, with narrow beamwidth of 20.4° and 26.4° in the E- and H-planes respectively at 16 GHz.

5.3.4 Fabrication & Measurements Results

In this section, the prototype validation process is carried out, by first fabricating all parts involved in the proposed design with its final optimized dimensions on the Rogers RT/ duroid 5880 dielectric slab with two different thicknesses for both the feed antenna (0.787 mm), and the proposed PRS based superstrate (1.57 mm). They are assembled using nylon M2 & M3 metric pan head screws with the proper washers and hex nuts, to form the final proposed prototype (see Figure 5-12 (a)). The optimal cavity spacing is fixed to 13 mm for further results validation and analysis. It is fed by a 50 Ohm SMA connector soldered to the feed line with an offset of 5 mm from the edge of the feed antenna.

Next, the reflection coefficients characteristics of the fabricated prototype are analyzed and measured using the Agilent 8722ES VNA, and the results are illus-

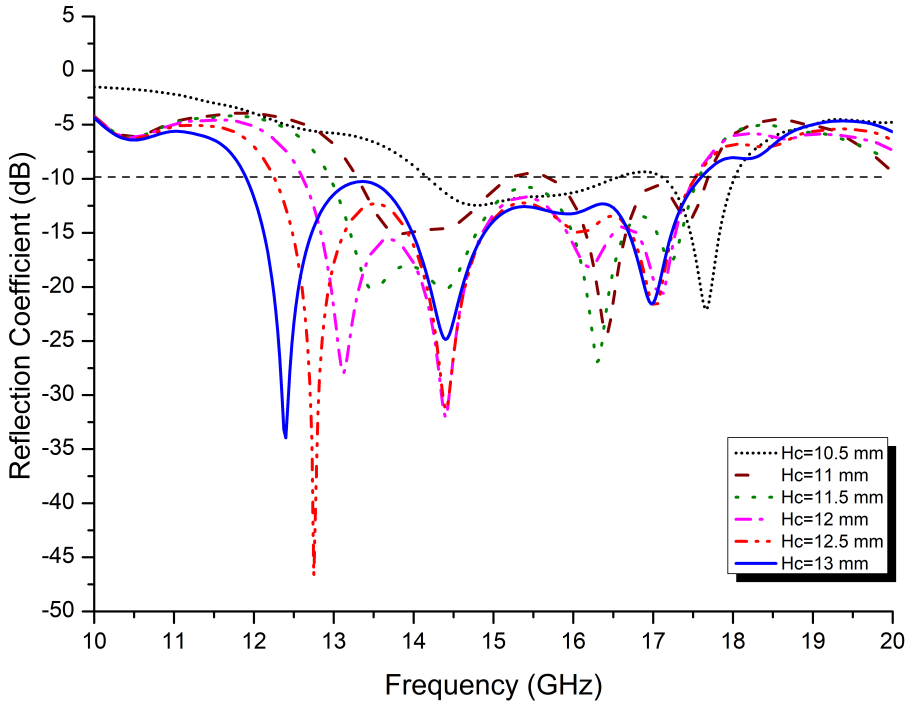

Figure 5-10: The simulated reflection coefficient of the proposed FPRA at different h_c.

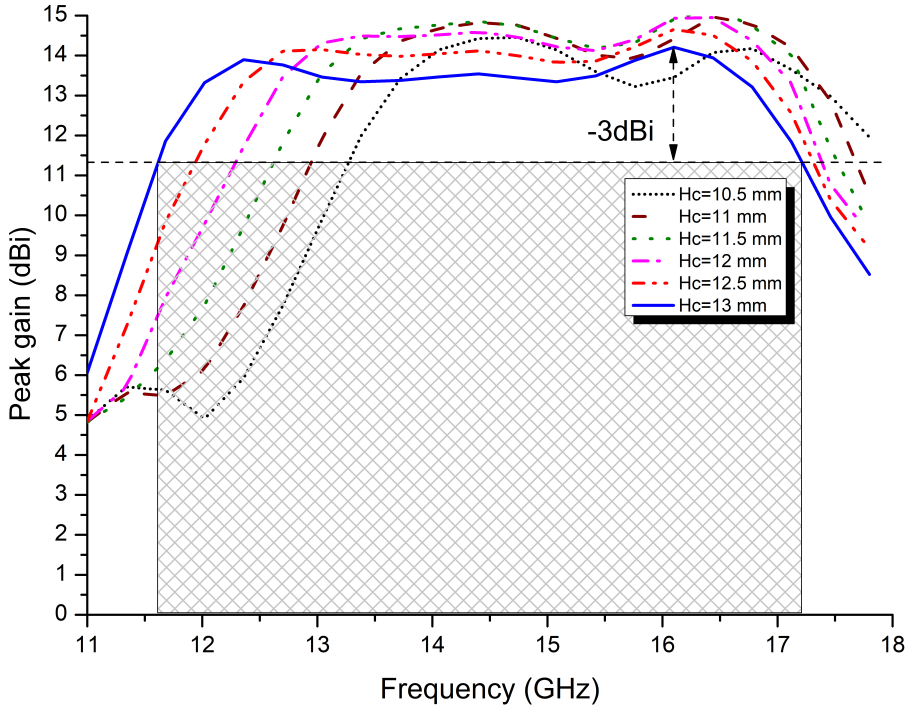

Figure 5-11: The simulated peak gain of the proposed FPRA at different values of h_c.

trated in Figure 5-13 (a), where the measured impedance bandwidth with S11 <-10

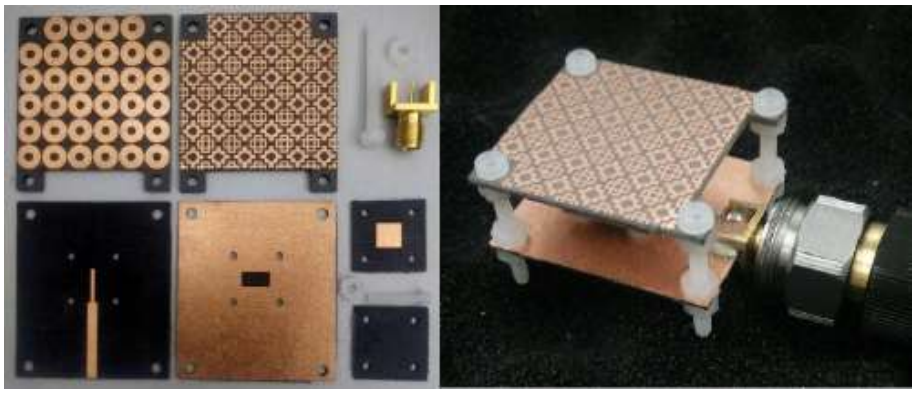

(a)

(b)

Figure 5-12: The final (a) fabricated antenna and its assembly parts, and (b) far-field measurement setup.

dB criterion is 6.03 GHz for a wide band FPRA ranging from 11.32 to 17.35 GHz, corresponding to a fractional impedance bandwidth of 42% with respect to the center frequency of interest. It is also compared to the simulated results, where the impedance bandwidth was 38.64% (5.7 GHz) ranging from 11.9 to 17.6 GHz. Therefore, both simulation and measurement results are in good agreement, despite the slight discrepancies between them, which are probably due to assembly and fabrication errors. Thus, the proposed antenna performed outstandingly in terms of wide impedance bandwidth, covering almost the whole Ku-band spectrum.

In addition, the peak gain and radiation patterns for the proposed prototype were measured in an anechoic chamber, and the setup is depicted in Figure 5-12 (b), and by using the following equation, the gain of the antenna under test (AUT) is calculated [82]:

$$G_{AUT} = G_{horn} - P_{horn} + P_{AUT} \tag{5.8}$$

where G_{horn} is the gain of the standard horn antenna.

P_{horn} and P_{AUT} are the received power of the horn antenna (receiver mode), and the antenna under testing, respectively. The results are depicted in Figure 5-13 (b), conforming that by using a PRS-based superstrate with a positively gradient phase, the peak gain over a wideband of frequency spectrum is improved drastically. From Figure 5-13 (b), the measured maximum peak gain of the proposed FPRA is 14.72 dBi at 16 GHz, with a 3-dB gain bandwidth of 36% (5.1 GHz) ranging from 11.68 to 16.78 GHz, which is in good agreement with the simulation results.

For further analysis, the normalized simulated and measured radiation patterns of the proposed FPRA are illustrated in Figure 5-14. at three different frequencies, 12.5, 14 and 16 GHz, in both H- and E-planes.

The obtained radiation patterns (simulated and measured) of the antenna, are directional in the broadside of both the E- and H-planes, with lower sidelobe levels, and a narrower beamwidth. Both simulation and measurements results are in good agreement, with a slight difference due to fabrication errors. With these features, the proposed design could be a potential candidate, allowing a high and consistent gain over a larger operating bandwidth, and low in profile, for applications in the Ku-band spectrum.

Finally, the proposed FPRA design is compared to others in the literature, taking into account the bandwidth, the maximum peak gain, the overall size of the design, and the number of PRS layers. The comparison is summarized in Table 5.3. From this comparison, it can be concluded that the proposed design outperforms the other ones in terms compactness, high gain and wider operation bandwidth.

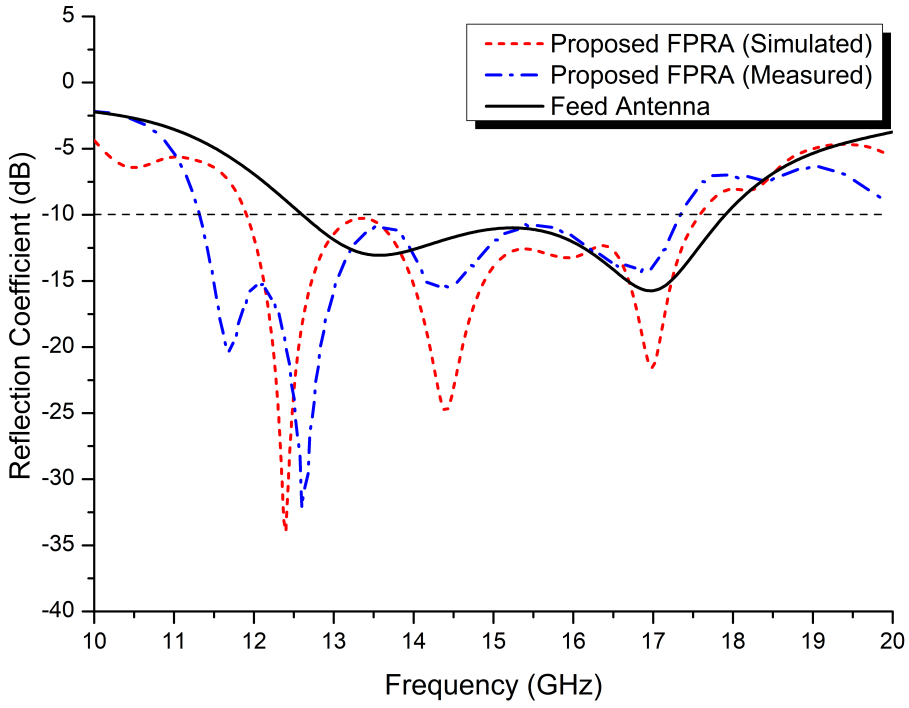

(a)

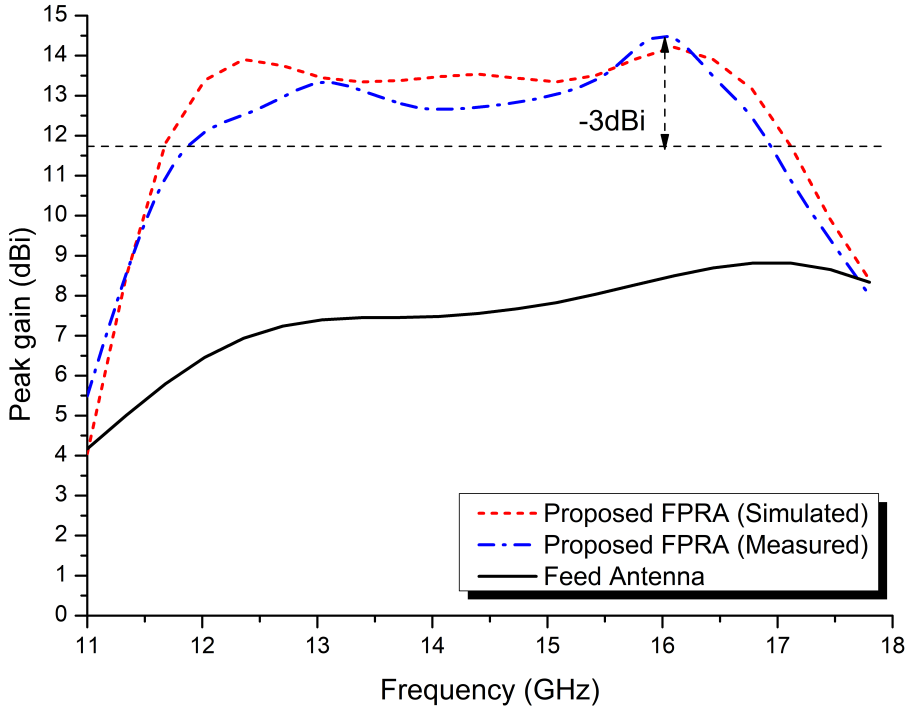

(b)

Figure 5-13: (a) reflection coefficients of the FPRA and (b) gain of the FPRA.

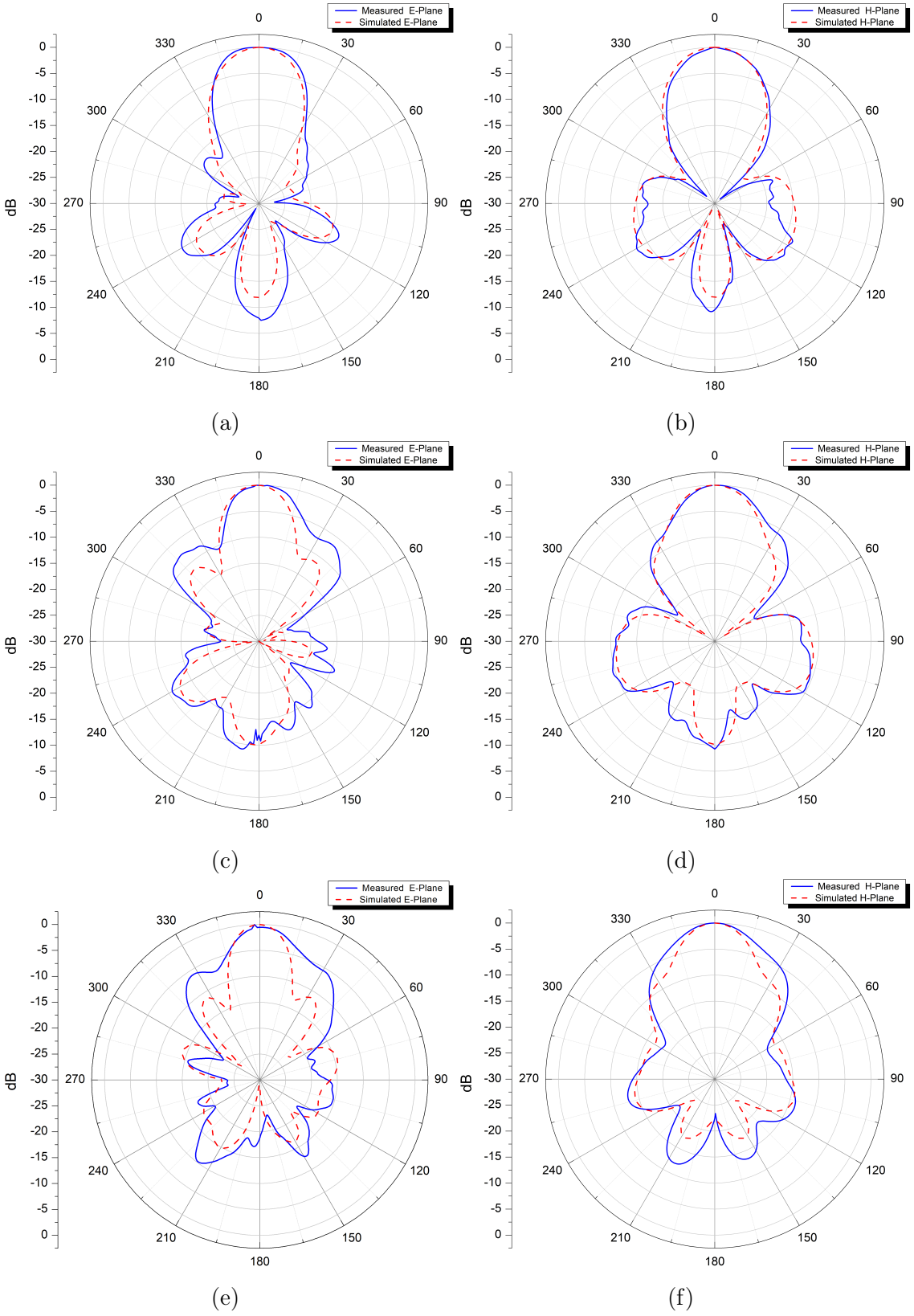

Figure 5-14: Normalized simulated and measured radiation patterns in the E-plane (a, b and c) and in the H-plane (d, e and f) at 12.5, 14, and 16 GHz.

Table 5.3: Proposed FPRA design compared to other related works.

Ref. No	$\|S11\|$ <-10dB BW(%)	3-dB gain bandwidth(%)	Antenna electrical (W x L x H)	Max gain (dBi)	Num. of PRS layers
[87]	25.1	33.5	2.23 λ_0 x 2.23 λ_0 x 0.54 λ_0	13.92	1
[91]	26.26	28	2.40 λ_0 x 2.40 λ_0 x 0.55 λ_0	13.8	1
[110]	10.9	10.9	3.67 λ_0 x 3.67 λ_0 x 0.75 λ_0	15	3
[111]	30	25.8	2.40 λ_0 x 2.40 λ_0 x 1.40 λ_0	15	2
[112]	15.06	15	3.90 λ_0 x 3.90 λ_0 x 1.70 λ_0	20	3
[109]	27	27	2.36 λ_0 x 2.36 λ_0 x 1.23 λ_0	14	2
This work	42	36	1.72 λ_0 x 1.96 λ_0 x 0.62 λ_0	14.72	1

5.4 Mm-wave Antenna design and analysis

The future of Millimeter-wave communication systems, not only meet the increasing demand of high data rates, low-latency, and low power consumption, but also unlock the possibilities of the futuristic technologies such as smart cities, virtual reality, and self-driving cars, etc..[113].

Due to atmospheric and propagation losses, signals transmitted over the Mm-wave spectrum get weaker, and to tackle this inconvenience, high gain antennas with wider operating frequencies are highly recommended for Mm-wave applications. Conventional techniques were employed to achieve high gain performances, such as in the case of array antennas [114], metamaterial based ones [12, 1, 9], and Fabry-Perot resonator antennas [115, 116].

In this section, a wide-band and high gain Fabry-Perot resonator antenna operating from 24.8 GHz to 31.16 GHz, is proposed for Mm-wave applications, by using a positively phase gradient PRS, generated and optimized using genetic algorithm.

5.4.1 Proposed PRS unit cell

A PRS with positive phase gradient is the main key point for designing a wideband Fabry-Perot resonator antenna as mentioned in the previous section, and to do so, a double-sided layer with Frequency Selective Surface printed patterns is proposed and designed on a Rogers RT/duroid 5880 dielectric slab (ϵ_{r1}= 2.2, tan δ=0.0009), with a thickness h_{PRS} of 0.787 mm. The bottom side is a simple ring-shaped FSS with the following design parameters: w_{PRS}=3.8 mm,r_o=1.7 mm, r_i=0.95 mm and

g=0.4 mm, and the upper part is synthesized automatically using an automated system, created by implementing an interface between CST Microwave studio and the embedded genetic algorithm in MATLAB, via a VBA based link. The final optimized PRS unit cell is shown in Figure 5-15.

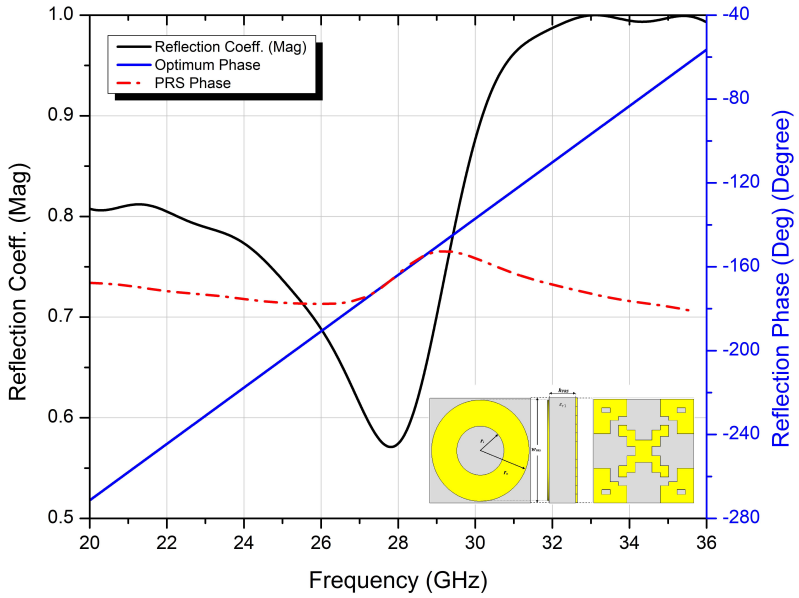

Figure 5-15: The GA based final optimized PRS design, and its reflection coefficient's magnitude and phase.

The resulted reflection coefficient phase of the optimized PRS has a positive gradient and is almost perfectly resembles that of the optimum PRS over a wide bandwidth spectrum range, with a relatively high reflection magnitude (See Figure 5-15), which makes it a potential superstrate candidate for a wideband and high gain FPRA for Mm-wave applications.

5.4.2 Proposed Mm-wave FPRA antenna

The geometry of the proposed FPRA antenna is depicted in Figure 5-16 (b). It consists of an air-gaped (h_{air}=1 mm) slot-coupled elliptical parasitic patch antenna, to a feeding line with an impedance matching network, to improve the bandwidth. Both the parasitic patch and the bottom layer (ground plane and the feed line) are printed on a Rogers RT/ duroid 5880 dielectric slab with a thickness (h_s) of 0.787 mm (see Figure 5-16 (a)).

The optimized parameters of the proposed feed antenna for optimal performance are: W_{sub1}= 26.6 mm, W_{sub2}= 10 mm, h_s = 0.787 mm, R_{WP}= 3.5 mm, R_{LP}= 2.5 mm, S_L= 3.1 mm, S_W= 1.4 mm, l_1=10 mm, l_2=3.3 mm l_3=1.1 mm, w_1=2.4 mm, w_2=0.9 mm.

The FPRA layer is suspended over this feed antenna at an optimal distance h_z

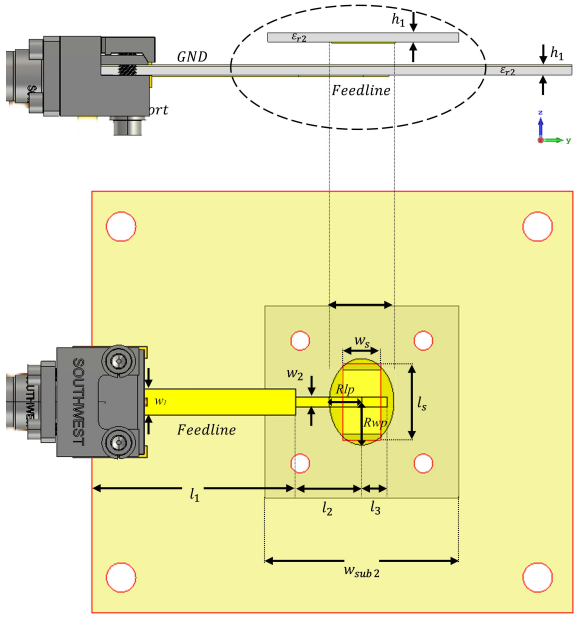

(a)

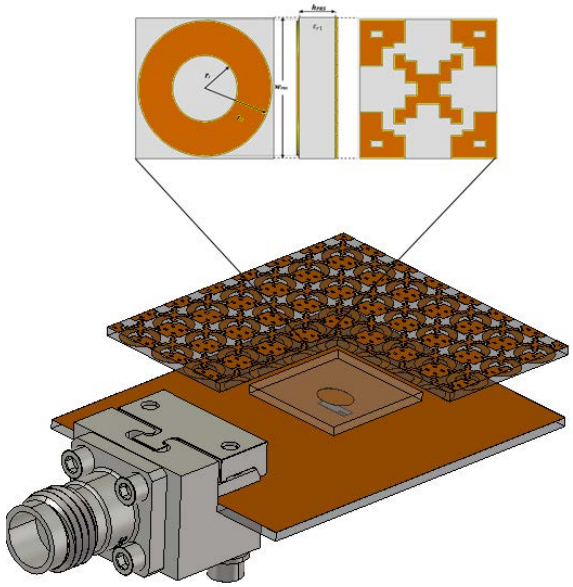

(b)

Figure 5-16: (a) The schematic diagram of the slot-coupled patch antenna. (b) The proposed wideband FPRA design with the PRS layer.

of 5.7 mm (see Figure 5-16 (b)).

The characteristics of the proposed antenna, namely the simulated reflection coefficient (S_{11}), the maximum achieved peak gain, and the 3-dB gain bandwidth, are illustrated in Figure 5-18, where it is clearly noticed that the impedance bandwidth almost covers the entire global 5G Mm-wave spectrum, ranging from 24.8 GHz to 31.16 GHz (22.73%), and the peak gain was 16.2 dBi within this band of interest in comparison to the antenna without PRS layer, with a maximum peak gain of only 8 dBi (see Figure 5-18).

In addition, the proposed antenna achieved a wide 3-dB gain bandwidth of 22.10% (6.26 GHz) in the range of 25.2 to 31.45 GHz, and this is due to the well-designed PRS based superstrate layer, with a positive phase gradient, and by ensuring the multiple reflections between the source antenna and the proposed superstrate, the gain is enhanced accordingly. Meaning, the proposed PRS based superstrate is acting as a lens, focusing the electromagnetic radiations from the source antenna in the broadside direction.

The radiation patterns at the center frequency 28 GHz in both E-and H-planes are simulated and depicted in Figure 5-19. From this figure, it is clearly noticed that the patterns are directive, with narrow beamwidth of 20.9° and 22.4° in the E- and H-planes respectively, with low side and back lobe levels of -14 dB.

5.4.3 Fabrication & Measurements Results

In this section, the prototype validation procedure is carried out, by first fabricating all parts involved in the proposed design with its final optimized dimensions on the Rogers RT/ duroid 5880 dielectric slab with a thickness of 0.787 mm for both the feed antenna, and the proposed PRS based superstrate. They are assembled using nylon M2 & M2.5 metric pan head screws with the proper washers and hex nuts, to form the final proposed prototype (see Figure 5-17 (a)). The optimal cavity spacing is fixed to 5.7 mm for further results validation and analysis. It is fed by a 2.92mm (K) connector screwed and fixed to the feed line with an offset of 6 mm from the edge of the feed antenna.

Next, the reflection coefficients characteristics of the fabricated prototype are

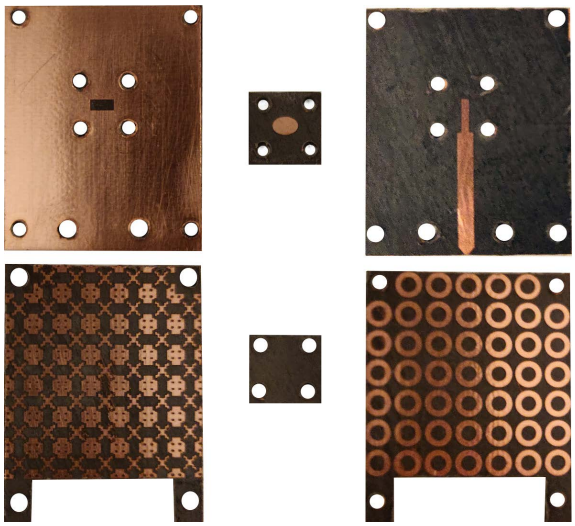

(a)

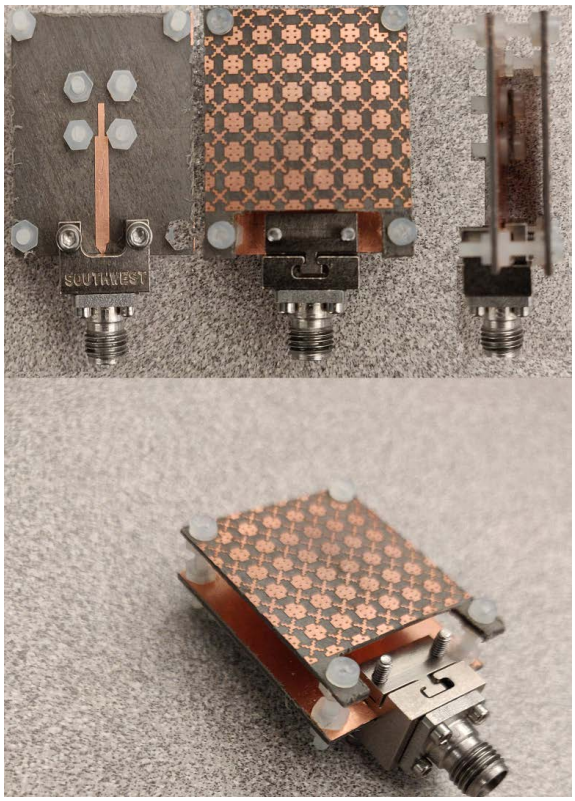

(b)

Figure 5-17: The fabricated antenna: (a) The assembly parts, and (b) the final FPRA prototype.

analyzed and measured using the Agilent 8722ES VNA, and the results are illustrated in Figure 5-18, where the measured impedance bandwidth with S_{11} <-10 dB criterion is 8.26 GHz for a wide band FPRA ranging from 25.17 to 33.43 GHz, corresponding to a fractional impedance bandwidth of 28.19% with respect to the

center frequency of interest. It is also compared to the simulated results, where the impedance bandwidth was 22.10% (6.26 GHz) ranging from 25.2 to 31.45 GHz. Therefore, both simulation and measurement results are in good agreement, despite the slight discrepancies between them, which are probably due to assembly and fabrication errors specially in the mm-wave region. Thus, the proposed antenna performed outstandingly in terms of wide impedance bandwidth.

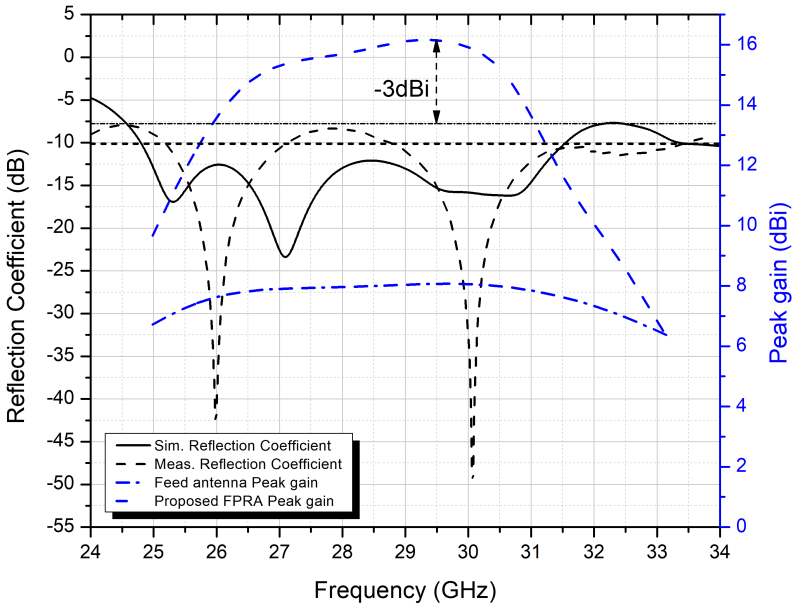

Figure 5-18: Reflection coefficients of the FPRA and it's gain compared to the feed antenna.

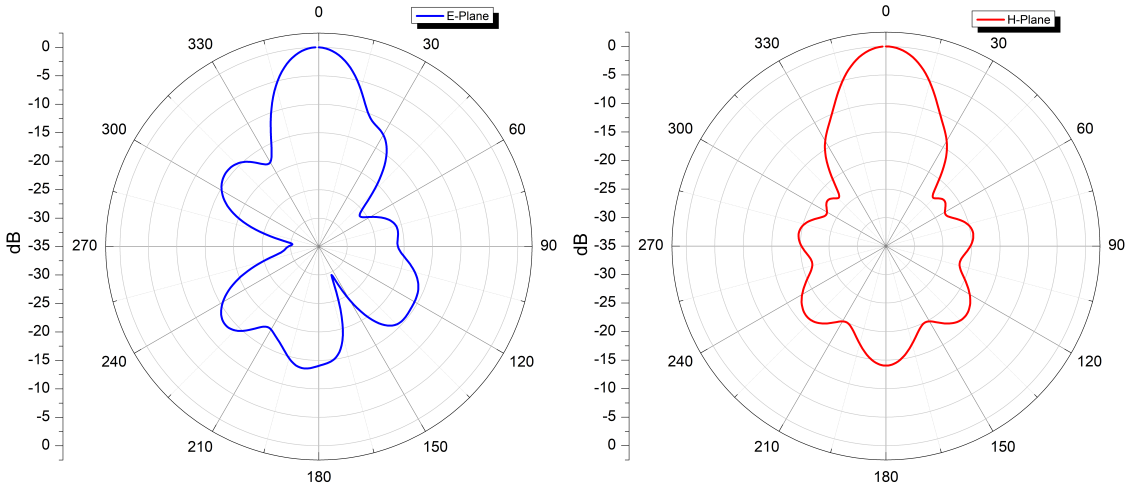

(a) (b)

Figure 5-19: Normalized simulated radiation patterns in the E-plane (a), and in the H-plane (b) at 28 GHz.

In this section, a topology synthesized partially reflective surface has been designed and simulated. This proposed PRS layer has provided a positive reflection coefficient phase, which leads to a wider impedance, 3-dB gain bandwidth and high gain at the Mm-wave band. The final design exhibited a wider operating bandwidth with simpler and small footprint design, creating a FPRA antenna with capabilities suitable for future Mm-wave applications such as 5G.

5.5 Summary

In this chapter, a topology optimized PRS using the genetic algorithm embedded in MATLAB, with a VBA based interface established with CST Microwave studio, has been designed and simulated. This proposed PRS design has provided a positive reflection coefficient phase, which leads to a wider impedance, 3-dB gain bandwidth and high gain at both the Ku- and Mm-wave bands.

The proposed prototypes have been fabricated and measured, and the simulation results were validated by measurements, and they have shown good agreements between them, with a slight difference due to fabrication errors, especially in the Mm-wave region.

Aside from the aforementioned improvements, using the proposed PRS layer shaped, the radiation pattern becomes more directive, with a narrower beamwidth, and lower sidelobe levels.

The proposed PRS-based Fabry-Perot resonator antennas can be considerate as good candidates for high gain with wideband of operation in both the Ku-band and the Mm-wave spectrum.

Chapter 6

Conclusions

6.1 Conclusion

The goal of this thesis was to discover an efficient and precise method for designing periodic structures such as EBGs, PBGs, AMCs, FSSs and Partially reflective surfaces, acting as modified dielectric mediums, reflectors, superstrates and lenses to enhance the electrical properties of the widely used technology of microstrip patch antennas, due to their advantages in terms of cost, ease of fabrication and their light weight, making them an attractive choice when designing an efficient communication system. Many design techniques have been developed in the last decade since periodic surfaces became widely used in antenna and microwave engineering.

The use of full-wave numerical models is the most accurate and universal method of designing periodic structures. The design process becomes more consistent and the overall computational time can be significantly reduced when optimization algorithms are used for both rough initial design and final tuning.

Periodic surfaces acting as an artificial magnetic conductor, electromagnetic and photonic band gap structures were successfully implemented using global evolutionary algorithms. Their application in the design of structures with suppressed surface waves propagation has been investigated throughout the progression of the thesis, while using the full-wave numerical simulator CST Microwave Studio and Ansoft High Frequency Structure Simulator HFSS.

Then, a technique based on the genetic optimization algorithm GA embedded in

the famous simulator MATLAB, in corporation with CST Mirowave studio simulator through a well established VBA based link, has been used to build and evaluate an EBG based microstrip patch antenna for WiMAX application.

A study of different thicknesses and high permittivity substrates were simulated and discussed, and a final step-like substrate is then used to build the initial antenna for further analysis. Using CST microwave studio with the GA proved to be useful for optimizing an EBG based substrate for the proposed microstrip antenna with the desired features. In fact, the Step-like EBG (S-EBG based antenna has been found to be appropriate for wideband operating around 5.8 GHz with a return loss enhancement of 100% compared with the initial antenna. In comparison, it has also enhanced the fractional bandwidth for the patch antenna, based on the EBG structure, by 531.818% relative to the original antenna (thin substrate). Their bandwidth is substantially increased. Furthermore, by implementing the mushroom-like EBG the side lobes levels decreased. The improved antenna features are attributed to the fact that by using the mushroom-like EBG the surface waves are suppressed. The final prototype was fabricated and validated through measurements, and compared to related works in the field, presenting its potential as a high gain antenna for WiMAX, WLAN, etc...

After that, a variety of microstrip patch antennas are designed, simulated and analyzed to achieve an UWB coverage with higher gain and easy to fabricate prototypes. First, a conventional microstrip fed patch antenna is designed and the maximum achieved impedance bandwidth was 0.175GHz ranging from 5.71 to 5.88 GHz, corresponding to a fractional bandwidth (FBW) of only 3.01 %. Next, a curved partial ground (PG-MPA) was then used to broaden the antenna bandwidth without increasing its size profile, and maximum achieved bandwidth was 3.5 GHz, an improvement by a factor of 20, compared to the initial design, ranging from 3.1 to 6.6 GHz, and an FBW of 60 %. Even with this technique, the proposed design is far away from achieving an UWB operating bandwidth.

In order to increase its impedance bandwidth, while keeping its compactness, an automated synthesizing and computer aided system is proposed, to create unique check-board-like patterns on the effective area of the radiating patch, and this led

to an increase in the impedance bandwidth of 10.4 GHz, ranging from 3.1 to 13.5 GHz, corresponding to an FBW of 179.31 %. So, the proposed design achieved the required bandwidth (3.1-10.6 GHz) while keeping its compactness and low profile.

Furthermore, an ultra-wideband FSS reflecting layer was also generated using the same technique, and evaluated according to a specific fitness function to achieve the UWB capability, with minimum foot print. Different designs and prototypes were fabricated and validated through measurements, and further analysis, and the results showed the potential of the proposed design, by comparing it to related works in the literature, proving its capabilities as a high gain and UWB antenna.

Finally, a novel FPRA antenna was developed and analyzed for the Ku-band and Mm-wave frequency regions, fed by an aperture-coupled antenna and supported by a PRS superstrate layer with a positive phase gradient that follows almost perfectly the optimum phase in the frequency band of interest, where the wide band of operation was then achieved.

The proposed antennas provide an outstanding performance in terms of impedance and 3-dB gain bandwidths, peak gain, and the side lobe levels (SLL, with narrower beamwidths suitable for high gain and more directive communication systems.

These findings demonstrated the feasibility and the efficiency of the proposed FPRA designs, with small foot prints, making them great candidates for high gain with On-chip integration possibility antennas for the future of wireless communication systems.

6.2 Suggestions

Some interesting suggestions and extensions of this thesis for the future can be outlined as follows as research progresses:

- Implementing current antenna designs and findings for the next generation of wireless communications systems 5G, by tackling all its aspects like: Beamforming, Massive MIMO, etc...
- Designing antenna array based on EBG/PBG, and other meta-materials/meta-surfaces.

- Design of new EBG structures based on 3D printing, incorporation with the proposed GA synthesizing system, that further enhances antenna features and performances, while keeping a degree of compactness and low fabrication cost.

Bibliography

[1] N. Melouki, A. Hocini, and T. A. Denidni, "Performance enhancement of a compact patch antenna using an optimized ebg structure," *Chinese Journal of Physics*, vol. 69, pp. 219–229, 2021.

[2] V. G. Veselago, "The electrodynamics of substances with simultaneously negative values of img align= absmiddle alt= ϵ eps/img and μ," *Physics-Uspekhi*, vol. 10, no. 4, pp. 509–514, 1968.

[3] P. J. Ferrer González, "Multifunctional metamaterial designs for antenna applications," 2015.

[4] R. A. Shelby, D. R. Smith, and S. Schultz, "Experimental verification of a negative index of refraction," *Science*, vol. 292, no. 5514, pp. 77–79, 2001.

[5] J. B. Pendry and D. R. Smith, "Reversing light with negative refraction," *Physics today*, vol. 57, pp. 37–43, 2004.

[6] J. B. Pendry, D. Schurig, and D. R. Smith, "Controlling electromagnetic fields," *Science*, vol. 312, no. 5781, pp. 1780–1782, 2006.

[7] D. Schurig, J. J. Mock, B. Justice, S. A. Cummer, J. B. Pendry, A. F. Starr, and D. R. Smith, "Metamaterial electromagnetic cloak at microwave frequencies," *Science*, vol. 314, no. 5801, pp. 977–980, 2006.

[8] D. Sievenpiper, L. Zhang, R. F. Broas, N. G. Alexopolous, and E. Yablonovitch, "High-impedance electromagnetic surfaces with a forbidden frequency band," *IEEE Transactions on Microwave Theory and Techniques*, vol. 47, no. 11, pp. 2059–2074, 1999.

[9] A. Hocini, N. Melouki, and T. Denidni, "Modeling and simulation of an antenna with optimized amc reflecting layer for gain and front-to-back ratio enhancement for 5g applications," in *Journal of Physics: Conference Series*, vol. 1492, no. 1. IOP Publishing, 2020, p. 012006.

[10] B. A. Munk, *Frequency selective surfaces: theory and design.* John Wiley & Sons, 2005.

[11] J. D. Joannopoulos, R. Meade, and J. Winn, "Photonic crystals princeton university press," *Princeton New Jersey*, 1995.

[12] M. N. E. Temmar, A. Hocini, D. Khedrouche, and M. Zamani, "Analysis and design of a terahertz microstrip antenna based on a synthesized photonic bandgap substrate using bpso," *Journal of Computational Electronics*, vol. 18, no. 1, pp. 231–240, 2019.

[13] Y. Rahmat-Samii and H. Mosallaei, "Electromagnetic band-gap structures: classification, characterization, and applications," 2001.

[14] J. Lo, "Étude de la reconfigurabilité d'une structure à bande interdite électromagnétique (bie) métallique par plasmas de décharge," Ph.D. dissertation, Université de Toulouse, Université Toulouse III-Paul Sabatier, 2012.

[15] D. Sievenpiper, "High-impedance electromagnetic surfaces [ph. d. dissertation]," *Electrical Engineering Department University of California, Los Angeles, Los Angeles, Calif, USA*, vol. 33, 1999.

[16] F. Yang and Y. Rahmat-Samii, *Electromagnetic band gap structures in antenna engineering.* Cambridge university press Cambridge, UK, 2009.

[17] M. Rahman and M. Stuchly, "Transmission line–periodic circuit representation of planar microwave photonic bandgap structures," *Microwave and optical technology letters*, vol. 30, no. 1, pp. 15–19, 2001.

[18] Y. Kim, F. Yang, and A. Z. Elsherbeni, "Compact artificial magnetic conductor designs using planar square spiral geometries," *Progress In Electromagnetics Research*, vol. 77, pp. 43–54, 2007.

[19] C. A. Balanis, *Antenna theory: analysis and design.* John wiley & sons, 2015.

[20] H. F. Shaban, H. A. Elmikaty, and A. A. Shaalan, "Study the effects of electromagnetic band-gap (ebg) substrate on two patch microstrip antenna," *Progress In Electromagnetics Research*, vol. 10, pp. 55–74, 2008.

[21] R. Gonzalo, G. Nagore, and P. d. Maagt, "Simulated and measured performance of a patch antenna on a 2-dimensional photonic crystals substrate," *Progress in Electromagnetics Research*, vol. 41, pp. 257–269, 2003.

[22] L. Liang, C. Liang, L. Chen, and X. Chen, "A novel broadband ebg using cascaded mushroom-like structure," *Microwave and Optical Technology Letters*, vol. 50, no. 8, pp. 2167–2170, 2008.

[23] J. P. Pereira, J. P. da Silva, and H. D. de Andrade, "A new design and analysis of a hexagonal pbg microstrip antenna," *Microwave and Optical Technology Letters*, vol. 57, no. 9, pp. 2147–2151, 2015.

[24] J. A. Buck, *Fundamentals of optical fibers.* John Wiley & Sons, 2004, vol. 50.

[25] S. Mumtaz and J. Rodriguez, "Introduction to d2d communication," in *Smart Device to Smart Device Communication.* Springer, 2014, pp. 1–22.

[26] J. Khan, D. A. Sehrai, and S. Ahmad, "Design and performance comparison of metamaterial based antenna for 4g/5g mobile devices," *International Journal of Electronics and Communication Engineering*, vol. 12, no. 6, pp. 382–387, 2018.

[27] H. Zhou, "Phased array for millimeter-wave mobile handset," in *2014 IEEE Antennas and Propagation Society International Symposium (APSURSI)*. IEEE, 2014, pp. 933–934.

[28] M. L. de Macedo Dantas, J. dos Santos Silva, H. C. C. Fernandes *et al.*, "Antenna for fifth generation (5g) using a ebg structure," in *New contributions in information systems and technologies*. Springer, 2015, pp. 33–38.

[29] A. L. T. de Oliveira, S. de Brito Espinola, J. R. F. de Melo, J. L. da Silva, H. C. C. Fernandes *et al.*, "Dual band patch antenna for 5g applications with ebg structure in the ground plane and substrate," in *World Conference on Information Systems and Technologies*. Springer, 2017, pp. 1044–1049.

[30] F. Yang and Y. Rahmat-Samii, "A low profile single dipole antenna radiating circularly polarized waves," *IEEE Transactions on Antennas and Propagation*, vol. 53, no. 9, pp. 3083–3086, 2005.

[31] Y. Zhang, J. Von Hagen, M. Younis, C. Fischer, and W. Wiesbeck, "Planar artificial magnetic conductors and patch antennas," *IEEE Transactions on Antennas and Propagation*, vol. 51, no. 10, pp. 2704–2712, 2003.

[32] R. L. Haupt, "An introduction to genetic algorithms for electromagnetics," *IEEE Antennas and Propagation Magazine*, vol. 37, no. 2, pp. 7–15, 1995.

[33] F. Capolino, *Theory and phenomena of metamaterials*. CRC press, 2017.

[34] Y. Ranga, L. Matekovits, K. P. Esselle, and A. R. Weily, "Design and analysis of frequency-selective surfaces for ultrawideband applications," in *2011 IEEE EUROCON-International Conference on Computer as a Tool*. IEEE, 2011, pp. 1–4.

[35] Y. Ranga, K. Esselle, L. Matekovits, and S. Hay, "Increasing the gain of a semicircular slot uwb antenna using an fss reflector," in *2012 IEEE-APS Topical Conference on Antennas and Propagation in Wireless Communications (APWC)*. IEEE, 2012, pp. 478–481.

[36] K. Da Xu, H. Xu, Y. Liu, J. Li, and Q. H. Liu, "Microstrip patch antennas with multiple parasitic patches and shorting vias for bandwidth enhancement," *IEEE Access*, vol. 6, pp. 11 624–11 633, 2018.

[37] A. A. Deshmukh, "Broadband slot cut shorted sectoral microstrip antennas," *IET Microwaves, Antennas & Propagation*, vol. 11, no. 9, pp. 1280–1287, 2017.

[38] S. Singhal, "Octagonal sierpinski band-notched super-wideband antenna with defected ground structure and symmetrical feeding," *Journal of Computational Electronics*, vol. 17, no. 3, pp. 1071–1081, 2018.

[39] T. Ali, K. D. Prasad, and R. C. Biradar, "A miniaturized slotted multiband antenna for wireless applications," *Journal of Computational Electronics*, vol. 17, no. 3, pp. 1056–1070, 2018.

[40] T. Lo, Y. Hwang, E. Lam, B. Lee *et al.*, "Miniature aperture-coupled microstrip antenna of very high permittivity," *Electronics Letters*, vol. 33, no. 1, pp. 9–10, 1997.

[41] A. Rivera-Albino and C. A. Balanis, "Gain enhancement in microstrip patch antennas using hybrid substrates," *IEEE Antennas and Wireless Propagation Letters*, vol. 12, pp. 476–479, 2013.

[42] P. Samineni, T. Khan, and A. De, "Modeling of electromagnetic band gap structures: A review," *International Journal of RF and Microwave Computer-Aided Engineering*, vol. 27, no. 2, p. e21055, 2017.

[43] S. Peddakrishna, T. Khan, and A. De, "Electromagnetic band-gap structured printed antennas: A feature-oriented survey," *International Journal of RF and Microwave Computer-Aided Engineering*, vol. 27, no. 7, p. e21110, 2017.

[44] H. Boutayeb, T. Djerafi, and K. Wu, "Gain enhancement of a circularly polarized microstrip patch antenna surrounded by a circular mushroom-like substrate," in *The 40th European Microwave Conference*. IEEE, 2010, pp. 1734–1737.

[45] N. Rao and D. K. Vishwakarma, "Gain enhancement of microstrip patch antenna using sierpinski fractal-shaped ebg," *International Journal of Microwave and Wireless Technologies*, vol. 8, no. 6, p. 915, 2016.

[46] B. Zoubiri, A. Mayouf, F. Mayouf, S. Abdelkebir, and T. Devers, "Enhancement of front-to-back ratio and gain of rectangular microstrip antenna using novel elliptical ebg structure," *Microsystem Technologies*, vol. 24, no. 8, pp. 3241–3244, 2018.

[47] R. Sifat, M. R. I. Faruque, E. Ahmed, M. T. Islam, and M. U. Khandaker, "Electric field controlled cohesive symmetric hook-c shape inspired metamaterial for s-band application," *Chinese Journal of Physics*, vol. 68, pp. 28–38, 2020.

[48] A. M. Tamim, M. R. I. Faruque, E. Ahamed, and M. T. Islam, "Electromagnetic absorption of srr based double-inverse e-shaped metamaterial for dcs, eesc, 5g, and wimax applications," *Chinese Journal of Physics*, vol. 66, pp. 349–361, 2020.

[49] S. Peddakrishna, T. Khan, and B. K. Kanaujia, "Resonant characteristics of aperture type fss and its application in directivity improvement of microstrip antenna," *AEU-International Journal of Electronics and Communications*, vol. 79, pp. 199–206, 2017.

[50] S. Peddakrishna and T. Khan, "Performance improvement of slotted elliptical patch antenna using fss superstrate," *International Journal of RF and Microwave Computer-Aided Engineering*, vol. 28, no. 9, p. e21421, 2018.

[51] F. Yang, C.-S. Kee, and Y. Rahmat-Samii, "Step-like structure and ebg structure to improve the performance of patch antennas on high dielectric substrate," in *IEEE Antennas and Propagation Society International Symposium. 2001 Digest. Held in conjunction with: USNC/URSI National Radio Science Meeting (Cat. No. 01CH37229)*, vol. 2. IEEE, 2001, pp. 482–485.

[52] L. Liang, C. Liang, L. Chen, and X. Chen, "A novel broadband ebg using cascaded mushroom-like structure," *Microwave and Optical Technology Letters*, vol. 50, no. 8, pp. 2167–2170, 2008.

[53] S. Enoch, G. Tayeb, and D. Maystre, "Dispersion diagrams of bloch modes applied to the design of directive sources," *Progress In Electromagnetics Research*, vol. 41, pp. 61–81, 2003.

[54] A. Aminian, F. Yang, and Y. Rahmat-Samii, "In-phase reflection and em wave suppression characteristics of electromagnetic band gap ground planes," in *IEEE Antennas and Propagation Society International Symposium. Digest. Held in conjunction with: USNC/CNC/URSI North American Radio Sci. Meeting (Cat. No. 03CH37450)*, vol. 4. IEEE, 2003, pp. 430–433.

[55] L. Li, Q. Chen, Q. Yuan, C. Liang, and K. Sawaya, "Surface-wave suppression band gap and plane-wave reflection phase band of mushroomlike photonic band gap structures," *Journal of Applied Physics*, vol. 103, no. 2, p. 023513, 2008.

[56] E. Rajo-Iglesias, L. Inclán-Sánchez, J.-L. Vázquez-Roy, and E. García-Muñoz, "Size reduction of mushroom-type ebg surfaces by using edge-located vias," *IEEE Microwave and Wireless Components Letters*, vol. 17, no. 9, pp. 670–672, 2007.

[57] H. Boutayeb and T. A. Denidni, "Gain enhancement of a microstrip patch antenna using a cylindrical electromagnetic crystal substrate," *IEEE transactions on antennas and propagation*, vol. 55, no. 11, pp. 3140–3145, 2007.

[58] M. E. de Cos, Y. Álvarez, and F. Las-Heras, "Enhancing patch antenna bandwidth by means of uniplanar ebg-amc," *Microwave and Optical Technology Letters*, vol. 53, no. 6, pp. 1372–1377, 2011.

[59] T. Ali, K. D. Prasad, and R. C. Biradar, "A miniaturized slotted multiband antenna for wireless applications," *Journal of Computational Electronics*, vol. 17, no. 3, pp. 1056–1070, 2018.

[60] J. P. Pereira, J. P. da Silva, and H. D. de Andrade, "A new design and analysis of a hexagonal pbg microstrip antenna," *Microwave and Optical Technology Letters*, vol. 57, no. 9, pp. 2147–2151, 2015.

[61] J. L. da Silva, H. D. de Andrade, A. S. Maia, H. C. Fernandes, I. B. da Silva, A. S. Sombra, and J. P. Pereira, "Performance of microstrip patch antenna due ebg/pbg arrangements insertion," *Microwave and Optical Technology Letters*, vol. 58, no. 12, pp. 2933–2937, 2016.

[62] Y. Lo, D. Solomon, and W. Richards, "Theory and experiment on microstrip antennas," *IEEE transactions on Antennas and Propagation*, vol. 27, no. 2, pp. 137–145, 1979.

[63] F. C. Commission *et al.*, "First order and report: Revision of part 15 of the commision's rules regarding uwb transmission systems," 2002.

[64] G. Tiberi, S. Bertini, W. Q. Malik, A. Monorchio, D. J. Edwards, and G. Manara, "Analysis of realistic ultrawideband indoor communication channels by using an efficient ray-tracing based method," *IEEE Transactions on Antennas and Propagation*, vol. 57, no. 3, pp. 777–785, 2009.

[65] Q. Wu, R. Jin, J. Geng, and D. Su, "On the performance of printed dipole antenna with novel composite corrugated-reflectors for low-profile ultrawideband applications," *IEEE transactions on antennas and propagation*, vol. 58, no. 12, pp. 3839–3846, 2010.

[66] S. Weigand, G. H. Huff, K. H. Pan, and J. T. Bernhard, "Analysis and design of broad-band single-layer rectangular u-slot microstrip patch antennas," *IEEE transactions on antennas and propagation*, vol. 51, no. 3, pp. 457–468, 2003.

[67] D. S. Weile, "Electromagnetic metamaterials: Physics and engineering explorations (engheta, n. and ziolkowski, rw; 2006)[book review]," *IEEE Antennas and Propagation Magazine*, vol. 49, no. 4, pp. 137–139, 2007.

[68] R. R. Krishna and R. Kumar, "Slotted ground microstrip antenna with fss reflector for high-gain horizontal polarisation," *Electronics Letters*, vol. 51, no. 8, pp. 599–600, 2015.

[69] K. N. Paracha, S. K. Abdul Rahim, P. Soh, H. T. Chatha, M. H. Misran, and A. H. Lokman, "A dual band stub-loaded amc design for the gain enhancement of a planar monopole antenna," *Microwave and Optical Technology Letters*, vol. 60, no. 9, pp. 2108–2112, 2018.

[70] Y. Liu, Y. Hao, and S. Gong, "Low-profile high-gain slot antenna with fabry-pérot cavity and mushroom-like electromagnetic band gap structures," *Electronics Letters*, vol. 51, no. 4, pp. 305–306, 2015.

[71] T. A. Elwi, H. M. Al-Rizzo, D. G. Rucker, and F. Song, "Numerical simulation of a uc–pbg lens for gain enhancement of microstrip antennas," *International Journal of RF and Microwave Computer-Aided Engineering: Co-sponsored by the Center for Advanced Manufacturing and Packaging of Microwave, Optical, and Digital Electronics (CAMPmode) at the University of Colorado at Boulder*, vol. 19, no. 6, pp. 676–684, 2009.

[72] S. Peddakrishna, T. Khan, and B. K. Kanaujia, "Resonant characteristics of aperture type fss and its application in directivity improvement of microstrip antenna," *AEU-International Journal of Electronics and Communications*, vol. 79, pp. 199–206, 2017.

[73] S. Peddakrishna and T. Khan, "Performance improvement of slotted elliptical patch antenna using fss superstrate," *International Journal of RF and Microwave Computer-Aided Engineering*, vol. 28, no. 9, p. e21421, 2018.

[74] N. Kushwaha, R. Kumar, and T. Oli, "Design of a high-gain ultra-wideband slot antenna using frequency selective surface," *Microwave and Optical Technology Letters*, vol. 56, no. 6, pp. 1498–1502, 2014.

[75] Y. Ranga, L. Matekovits, A. R. Weily, and K. P. Esselle, "A constant gain ultra-wideband antenna with a multi-layer frequency selective surface," *Progress In Electromagnetics Research*, vol. 38, pp. 119–125, 2013.

[76] R. Sivasamy and M. Kanagasabai, "A novel miniaturized frequency selective surface," *International Journal of RF and Microwave Computer-Aided Engineering*, vol. 29, no. 6, p. e21691, 2019.

[77] M. Yan, S. Qu, J. Wang, H. Ma, J. Zhang, W. Wang, L. Zheng, and H. Yuan, "A single layer ultra-miniaturized fss operating in vhf," *Photonics and Nanostructures-Fundamentals and Applications*, vol. 17, pp. 1–9, 2015.

[78] M. Lamsalli, A. El Hamichi, M. Boussouis, N. Amar Touhami, and T. Elhamadi, "Genetic algorithm optimization for microstrip patch antenna miniaturization," *Progress In Electromagnetics Research*, vol. 60, pp. 113–120, 2016.

[79] M. John and M. J. Ammann, "Wideband printed monopole design using a genetic algorithm," *IEEE Antennas and Wireless Propagation Letters*, vol. 6, pp. 447–449, 2007.

[80] R. A. Abdulhasan, R. Alias, K. N. Ramli, F. C. Seman, and R. A. Abd-Alhameed, "High gain cpw-fed uwb planar monopole antenna-based compact uniplanar frequency selective surface for microwave imaging," *International Journal of RF and Microwave Computer-Aided Engineering*, vol. 29, no. 8, p. e21757, 2019.

[81] D. Belmessaoud, K. Rouabah, I. Messaoudene, and T. A. Denidni, "Broadband planar slot antenna using a simple single-layer fss stopband," *IET Microwaves, Antennas & Propagation*, vol. 14, no. 3, pp. 203–210, 2020.

[82] H. Zhu, X. Li, Z. Qi, and J. Xiao, "A 320 ghz octagonal shorted annular ring on-chip antenna array," *IEEE Access*, vol. 8, pp. 84 282–84 289, 2020.

[83] R. Mondal, P. S. Reddy, D. C. Sarkar, and P. P. Sarkar, "Compact ultra-wideband antenna: improvement of gain and fbr across the entire bandwidth using fss," *IET Microwaves, Antennas & Propagation*, vol. 14, no. 1, pp. 66–74, 2019.

[84] Y. Ranga, L. Matekovits, K. P. Esselle, and A. R. Weily, "Multioctave frequency selective surface reflector for ultrawideband antennas," *IEEE Antennas and Wireless Propagation Letters*, vol. 10, pp. 219–222, 2011.

[85] F. C. Segundo, A. L. P. Campos, A. Gomes Neto, and M. d. O. Alencar, "Double layer frequency selective surface for ultra wide band applications with angular stability and polarization independence," *Journal of Microwaves, Optoelectronics and Electromagnetic Applications*, vol. 18, no. 3, pp. 328–342, 2019.

[86] S. Kundu, A. Chatterjee, S. K. Jana, and S. K. Parui, "Gain enhancement of a printed leaf shaped uwb antenna using dual fss layers and experimental study for ground coupling gpr applications," *Microwave and Optical Technology Letters*, vol. 60, no. 6, pp. 1417–1423, 2018.

[87] F. Meng and S. K. Sharma, "A wideband resonant cavity antenna with compact partially reflective surface," *IEEE Transactions on Antennas and Propagation*, vol. 68, no. 2, pp. 1155–1160, 2019.

[88] M. Mahajan, R. Jyoti, K. Sood, and S. Sharma, "A method of generating simultaneous contoured and pencil beams from single shaped reflector antenna," *IEEE transactions on antennas and propagation*, vol. 61, no. 10, pp. 5297–5301, 2013.

[89] H. Deguchi, M. Tsuji, and H. Shigesawa, "Compact low-cross-polarization horn antennas with serpentine-shaped taper," *IEEE transactions on antennas and propagation*, vol. 52, no. 10, pp. 2510–2516, 2004.

[90] Y. J. Cheng, Y. X. Guo, and Z. G. Liu, "W-band large-scale high-gain planar integrated antenna array," *IEEE Transactions on Antennas and Propagation*, vol. 62, no. 6, pp. 3370–3373, 2014.

[91] N. Wang, Q. Liu, C. Wu, L. Talbi, Q. Zeng, and J. Xu, "Wideband fabry-perot resonator antenna with two complementary fss layers," *IEEE Transactions on Antennas and Propagation*, vol. 62, no. 5, pp. 2463–2471, 2014.

[92] H. H. Tran and T. K. Nguyen, "K-band planar and low-profile fabry-perot cavity antenna with a coupled strip-slitline feed structure," *Applied Computational Electromagnetics Society Journal*, vol. 32, no. 6, pp. 542–547, 2017.

[93] Z.-G. Liu, Z.-X. Cao, and L.-N. Wu, "Compact low-profile circularly polarized fabry–perot resonator antenna fed by linearly polarized microstrip patch," *IEEE Antennas and Wireless Propagation Letters*, vol. 15, pp. 524–527, 2015.

[94] Y.-F. Cheng, W. Shao, X. Ding, and M.-X. Yu, "Design of tilted-beam fabry-perot antenna with aperiodic partially reflective surface," *Applied Computational Electromagnetics Society Journal*, vol. 32, no. 5, 2017.

[95] Y. Ge, K. P. Esselle, and T. S. Bird, "The use of simple thin partially reflective surfaces with positive reflection phase gradients to design wideband, low-profile ebg resonator antennas," *IEEE Transactions on Antennas and Propagation*, vol. 60, no. 2, pp. 743–750, 2011.

[96] M. L. Abdelghani, H. Attia, and T. A. Denidni, "Dual-and wideband fabry–pérot resonator antenna for wlan applications," *IEEE Antennas and Wireless Propagation Letters*, vol. 16, pp. 473–476, 2016.

[97] C. Mateo-Segura, A. P. Feresidis, and G. Goussetis, "Bandwidth enhancement of 2-d leaky-wave antennas with double-layer periodic surfaces," *IEEE Transactions on Antennas and Propagation*, vol. 62, no. 2, pp. 586–593, 2013.

[98] N. Wang, J. Xu, and Q. Zeng, "Broadband ebg resonator antenna using a combination of different dielectric substrates," in *2013 IEEE Antennas and Propagation Society International Symposium (APSURSI)*. IEEE, 2013, pp. 894–895.

[99] R. M. Hashmi and K. P. Esselle, "A class of extremely wideband resonant cavity antennas with large directivity-bandwidth products," *IEEE Transactions on Antennas and Propagation*, vol. 64, no. 2, pp. 830–835, 2015.

[100] R. M. Hashmi, K. P. Esselle, and S. G. Hay, "Directive beaming with lens-like superstates for low profile fabry-perot cavity antennas," in *2014 16th International Symposium on Antenna Technology and Applied Electromagnetics (ANTEM)*. IEEE, 2014, pp. 1–2.

[101] Y.-F. Lu and Y.-C. Lin, "Design and implementation of broadband partially reflective surface antenna," in *2011 IEEE International Symposium on Antennas and Propagation (APSURSI)*. IEEE, 2011, pp. 2250–2253.

[102] K. Kanjanasit and C. Wang, "A broadband resonant cavity antenna using a metamaterial based on double-side identical arrays," in *2017 IEEE Conference on Antenna Measurements & Applications (CAMA)*. IEEE, 2017, pp. 51–54.

[103] R. Lian, Z. Tang, and Y. Yin, "Design of a broadband polarization-reconfigurable fabry–perot resonator antenna," *IEEE Antennas and Wireless Propagation Letters*, vol. 17, no. 1, pp. 122–125, 2017.

[104] A. P. Feresidis, G. Goussetis, S. Wang, and J. C. Vardaxoglou, "Artificial magnetic conductor surfaces and their application to low-profile high-gain planar antennas," *IEEE Transactions on Antennas and Propagation*, vol. 53, no. 1, pp. 209–215, 2005.

[105] G. V. Trentini, "Partially reflecting sheet arrays," *IRE Transactions on antennas and propagation*, vol. 4, no. 4, pp. 666–671, 1956.

[106] L. Leger, C. Serier, R. Chantalat, M. Thevenot, T. Monedière, and B. Jecko, "1d dielectric electromagnetic band gap (ebg) resonator antenna design," in *Annales des télécommunications*, vol. 59, no. 3. Springer, 2004, pp. 242–260.

[107] L. Moustafa and B. Jecko, "Design and realization of a wide-band ebg antenna based on fss and operating in the ku-band," *International Journal of Antennas and Propagation*, vol. 2010, 2010.

[108] A. Feresidis and J. Vardaxoglou, "A broadband high-gain resonant cavity antenna with single feed," in *2006 First European Conference on Antennas and Propagation*. IEEE, 2006, pp. 1–5.

[109] N. Wang, L. Talbi, Q. Zeng, and J. Xu, "Wideband fabry-perot resonator antenna with electrically thin dielectric superstrates," *IEEE Access*, vol. 6, pp. 14 966–14 973, 2018.

[110] K. Konstantinidis, A. P. Feresidis, and P. S. Hall, "Broadband sub-wavelength profile high-gain antennas based on multi-layer metasurfaces," *IEEE Transactions on Antennas and Propagation*, vol. 63, no. 1, pp. 423–427, 2014.

[111] N. Wang, J. Li, G. Wei, L. Talbi, Q. Zeng, and J. Xu, "Wideband fabry–perot resonator antenna with two layers of dielectric superstrates," *IEEE Antennas and Wireless Propagation Letters*, vol. 14, pp. 229–232, 2014.

[112] K. Konstantinidis, A. P. Feresidis, and P. S. Hall, "Multilayer partially reflective surfaces for broadband fabry-perot cavity antennas," *IEEE Transactions on Antennas and Propagation*, vol. 62, no. 7, pp. 3474–3481, 2014.

[113] J. Thompson, X. Ge, H.-C. Wu, R. Irmer, H. Jiang, G. Fettweis, and S. Alamouti, "5g wireless communication systems: Prospects and challenges [guest editorial]," *IEEE Communications Magazine*, vol. 52, no. 2, pp. 62–64, 2014.

[114] N. Yoon and C. Seo, "A 28-ghz wideband 2× 2 u-slot patch array antenna," *Journal of electromagnetic engineering and science*, vol. 17, no. 3, pp. 133–137, 2017.

[115] M. Asaadi, I. Afifi, and A.-R. Sebak, "High gain and wideband high dense dielectric patch antenna using fss superstrate for millimeter-wave applications," *IEEE Access*, vol. 6, pp. 38 243–38 250, 2018.

[116] N. Hussain, M.-J. Jeong, J. Park, and N. Kim, "A broadband circularly polarized fabry-perot resonant antenna using a single-layered prs for 5g mimo applications," *IEEE Access*, vol. 7, pp. 42 897–42 907, 2019.

PhD thesis: *Contribution to the analysis and design of a microstrip antenna based on EBG structures for modern wireless communication systems.*

By: *Noureddine MELOUKI*

Supervisor: *Abdesselam HOCINI*

Co-supervisor : *Tayeb Ahmed DENIDNI*

الملخص

تركز هذه الأطروحة على تحليل وتصميم هوائيات ميكروستريب التي تعمل في نطاق واسع من نطاقات التردد (WiMAX و UWB و Ku-bandو mm-Wave)، وتعتمد على هياكل فجوة النطاق الكهرومغناطيسي (EBG) .تم تصميم الركيزة القائمة على هيكل فجوة النطاق الكهرومغناطيسي التي تشبه الفطر وتحليلها وتحسينها باستخدام تقنية تعتمد على مزيج من خوارزمية تحسين التطوري (الخوارزمية الجينية) مع المحاكي التجاري CST Microwave Studio ، من اجل تطبيقات واي ماكس. بعد ذلك ، تم تصميم وتحليل هوائي النطاق العريض للغاية المحسّن إلى جانب طبقة FSS مدمجة تغطي النطاق العريض .تتم مقارنة نتائج المحاكاة والقياسات التي تم الحصول عليها مع المقالات البحثية المختلفة. أخيرًا ، تم تصميم هوائيات Fabry-Pérot بناءً على هياكل PRS المقترحة ، والتي تم إنشاؤها وتحسينها باستخدام نظام تركيب تلقائي ، بناءً على ارتباط بين MATLAB (الخوارزمية الوراثية) والمحاكي CST Microwave studio ، وتم تحليلها وتصنيعها ، والنتائج التي تم الحصول عليها قورنت بالبحوث الأخرى في الميدان ، حيث يُشار بوضوح إلى أن التصميمات المقترحة يمكن أن تكون مرشحة محتملة لأنظمة ذات الاداء العالي والنطاق العريض في تطبيقات Ku-band و mm-wave ، مثل الجيل الخامس.

الكلمات الدلالية : الجيل الخامس ، هوائي ميكروستريب ، EBG / PBG، AMC، FSS، PRS، الخوارزمية الجينية ، CST، FPRA.

Abstract

This thesis focuses on the analysis and design of microstrip antennas working in a wide range of frequency bands (WiMAX, UWB, Ku-band, mm-Wave), and based on electromagnetic band gap (EBG) structures. A mushroom-like EBG structure-based substrate is designed, analyzed and optimized using a technique based on the combination of an evolutionary heuristic optimization algorithm (genetic algorithm) with the Computer Simulation Technology (CST) Microwave Studio, for WiMAX applications. Next, a topology optimized ultra-wideband antenna alongside a compact FSS layer, covering the UWB spectrum of frequencies, are designed and analyzed. The simulation results and measurements obtained are compared with various works in the open literature. Finally, Fabry-Pérot resonator antennas based on the proposed PRS structures, generated and optimized using an automatic synthesis system, based on a link between MATLAB and CST Microwave studio, were designed, analyzed and fabricated. The obtained results are compared with other research in the open literature, where it is clearly indicated that the proposed designs could be potential candidates for high gain and wideband systems in Ku-band and mm-wave applications, such as the 5G.

Keywords: 5G, Microstrip antenna, EBG/PBG, AMC, FSS, PRS, Genetic algorithm, CST, FPRA.

Résumé

Cette thèse se concentre sur l'analyse et la conception d'antennes microruban travaillant dans une large gamme de bandes de fréquences (WiMAX, UWB, Ku-band, mm-Wave), et basées sur des structures de bande interdite électromagnétique (EBG). Un substrat à base de structure EBG en forme de champignon est conçu, analysé and optimisé en utilisant une technique basée sur la combinaison d'un algorithme d'optimisation heuristique évolutive (algorithme génétique) avec le simulateur commerciale CST Microwave Studio pour l'application de WiMAX. Ensuite, une antenne ultra large bande optimisée en topologie aux côtés d'une couche FSS compacte, couvrant le spectre UWB des fréquences sont conçues et analysées. Les résultats de simulation et mesures obtenus sont comparés à différents articles de recherche dans la littérature. Enfin, des antennes résonatrices Fabry-Pérot basées sur des structures PRS proposées, générées et optimisées en utilisant un system de synthèse automatique, a base d'une lien entre MATLAB (Algorithme génétique) et CST Microwave studio, ont été conçues, analysées et fabriquées, et les résultats obtenus sont comparé avec d'autres recherches dans la littérature ouverte, où est clairement indiqué que les conceptions proposées pourraient être des candidats potentiels pour des systèmes à gain élevé et large bande dans les applications en bande Ku et en ondes mm, telles que la 5G.

Mots clés : 5G, Antenne microruban, EBG/PBG, AMC, FSS, PRS, Algorithme génétique, CST, FPRA.